

LUDWIG-MAXIMILIANS-UNIVERSITY  
MUNICH

MASTER THESIS

---

**Modelling the Spectral Energy Distribution  
of Low Luminosity Active Galactic Nuclei**

---

*Author:*  
Lennart REB

*Supervisor (LMU):*  
Klaus DOLAG

*External Supervisor (IAC):*  
Almudena PRIETO ESCUDERO  
Juan A. FERNÁNDEZ ONTIVEROS

*A thesis submitted in fulfilment of the requirements  
for the degree of Master of Science in physics*

*in the*

Computational Astrophysics Group  
University Observatory Munich

Tuesday 1<sup>st</sup> August, 2017



LUDWIG-MAXIMILIANS-UNIVERSITÄT  
MÜNCHEN

MASTERARBEIT

---

**Modellierung der spektralen  
Energieverteilung aktiver Galaxienkerne  
geringer Leuchtkraft**

---

*Autor:*  
Lennart REB

*Betreuer (LMU):*  
Klaus DOLAG

*Externe Betreuer (IAC):*  
Almudena PRIETO ESCUDERO  
Juan A. FERNÁNDEZ ONTIVEROS

*Eine Masterarbeit eingereicht zur Erlangung des akademischen Grades  
Master of Science in Physik*

*in der*

Computational Astrophysics Group  
Universitätssternwarte München

1. August, 2017



LUDWIG-MAXIMILIANS-UNIVERSITÄT MÜNCHEN

*Abstract*

University Observatory Munich

Master of Science

**Modelling the Spectral Energy Distribution of Low Luminosity Active Galactic Nuclei**

by Lennart REB

Today we believe that every massive galaxy harbours a supermassive black hole. Some of them are quiet, like our central SMBH Sagittarius A\*, while others are active: They accrete and release energy, forming active galactic nuclei (AGNs). Recent studies show that the most numerous class of AGNs in the local universe are low luminosity AGNs (LLAGNs), whose dominant energy output is probably carried by jets: collimated outflows of energetic particles. In contrast to the unified scheme for AGNs, where it is believed that around the black hole forms an accretion disc and further outside a torus, LLAGNs seem to show none of them. How then do the central engines receive energy? Which effects are triggering the launch of jets and provide their power? Despite the lack of knowledge about the full physical picture, a scaling relation of black holes over the entire mass-range is a starting point for developing numerical models; specifically in the case of LLAGNs models of jet-like outflows. Comparing those models with observational data, offers the possibility to study the ongoing physical processes in the vicinity of black holes. However, faint objects like LLAGNs are difficult to observe. The host galaxy typically outshines the nucleus and thus, observational data can be contaminated by stellar light of the host galaxy. In order to minimise this issue, and to truly image the physical nuclear region, observations with sub-arcsec resolution are necessary.

In this thesis a semi-analytical numerical model, focusing on jet emission, is applied to a sample of three nearby LLAGNs, whose observational spectra consist out of highest angular resolution images available over nearly 10 orders of magnitude in frequency. Especially the availability of high angular resolution data in the IR allows to test the model in a critical frequency range. For all sources the emission of a compact jet gives an excellent representation of the continuum emission over the entire spectrum. The well sampled SEDs enable to break the model degeneracy between synchrotron emission or the synchrotron self Comptonisation (SSC) mechanism for the origin of the X-ray spectrum. All three objects are SSC dominated.

Observations impose limits for the standard accretion disc component. For NGC 1052 the inferred model-independent maximum accretion energy budget is too low to account for the lower limit of the rest frame luminosity of the jet. Within this work a possible solution for this problem is proposed: A scaling relation is derived, which relates mass-to-light conversion efficiency to truncation radius. The method allows to estimate a minimum truncation radius and the maximum radiative efficiency for a disc of given accretion rate. In the case of NGC 1052 the application of this method and the thereof estimated minimum truncation radius is within the range of measurements of the Fe  $K\alpha$  line.



## *Acknowledgements*

First and foremost, I would like to express my gratitude to my supervisors Klaus Dolag, Almudena Prieto, and Juan Fernández Ontiveros.

In particular I would like to thank Klaus for encouraging me from the first second to begin this collaborative project.

I would like to thank Almudena for advising me from the very beginning and for supporting me until the last day.

They both found an excellent compromise between directing me and giving me the freedom to really go to the heart of the matter.

I would like to thank Juan who impressed me with his well-ordered knowledge. He helped me to find the logical thread in this work and spent a lot of time trying to teach me scientific writing.

I would like to thank all the other students previously or currently working at the USM. The weekly Astro-PH meeting has always been an enjoyable time to informally discuss interesting topics.

I would like to thank Max Hunter Gordon, who was there when I started and when I finished.

Finally I would express my deepest gratitude to my parents for their love and their dedication. They have always encouraged and supported me on my way.

Part of this work was done in the Instituto de Astrofísica de Canarias and was made possible by the Erasmus+ exchange program.

This research has made use of NASA's Astrophysics Data System and of the NASA/IPAC Extragalactic Database (NED) which is operated by the Jet Propulsion Laboratory, California Institute of Technology, under contract with the National Aeronautics and Space Administration.

This research has made use of "Aladin sky atlas" developed at CDS, Strasbourg Observatory, France.



# Contents

<b>Abstract</b>	<b>v</b>
<b>Acknowledgements</b>	<b>vii</b>
<b>Introduction</b>	<b>1</b>
<b>1 Active Galactic Nuclei</b>	<b>3</b>
1.1 Unified Scheme . . . . .	3
1.1.1 Supermassive Black Hole . . . . .	4
1.1.2 Accretion Disc . . . . .	4
1.1.3 BLR, Torus and NLR . . . . .	5
1.1.4 Jet . . . . .	5
1.2 Taxonomy . . . . .	5
1.3 Low Luminosity AGNs . . . . .	6
1.3.1 Spectral Energy Distribution compared to Seyferts and Quasar . . .	7
1.3.2 Differences to the Standard Picture . . . . .	8
<b>2 Radiative Processes</b>	<b>11</b>
2.1 Radiative Basics . . . . .	11
2.1.1 Intensity, Flux and Luminosity of Isotropic and Lambertian Sources	11
2.1.2 Radiative Transfer: Optically Thick versus Thin . . . . .	13
2.2 Black Body Emission: Planck, Rayleigh-Jeans and Stefan-Boltzmann . . . .	14
2.3 Basics of Electrodynamics . . . . .	15
2.3.1 Lorentz Force, Maxwell Equations and Poynting Vector . . . . .	15
2.3.2 Relativistic Larmor Formula . . . . .	17
2.4 Synchrotron Emission . . . . .	18
2.4.1 Emitted Power of a Single Relativistic Electron . . . . .	18
2.4.2 Typical and Critical Frequencies . . . . .	19
2.4.3 Electrons with a Power Law Energy Distribution . . . . .	21
2.4.4 Thin Emission and Self Absorption . . . . .	22
2.4.5 Superposition of Synchrotron Components in a Jet . . . . .	24
2.4.6 Energetic Argument Towards Equipartition . . . . .	24
2.5 Inverse Compton Effect . . . . .	25
2.5.1 Thomson Cross Section . . . . .	25
2.5.2 Electron Energy Loss . . . . .	26
2.5.3 Compton Spectrum . . . . .	28
2.5.4 Compton and Synchrotron - Similarities . . . . .	29
<b>3 The Model</b>	<b>31</b>
3.1 Description . . . . .	31
3.1.1 Nozzle and Energy . . . . .	33
3.1.2 Compact Jet . . . . .	33
3.1.3 Truncated Accretion Disc . . . . .	34
3.2 The Parameters . . . . .	36

<b>4</b>	<b>The Sample</b>	<b>39</b>
4.1	High Angular Resolution SEDs	39
4.2	NGC4594	41
4.3	NGC 1097	43
4.4	NGC1052	44
<b>5</b>	<b>Methods</b>	<b>49</b>
5.1	Invoking the Model	49
5.2	General Modelling Approach	49
5.3	Analysis	52
5.4	Black Body Considerations	53
5.4.1	Single and Multi Temperature Black Body	53
5.4.2	Efficiency Scaling of the Truncated Accretion Disc	54
5.4.3	Accretion Rate Dependent Limits for Truncation Radius and Efficiency	56
<b>6</b>	<b>Results</b>	<b>57</b>
6.1	NGC 4594	57
6.2	NGC 1097	61
6.3	NGC 1052	63
<b>7</b>	<b>Discussion</b>	<b>67</b>
7.1	NGC 4594	67
7.1.1	Model Consistency	67
7.1.2	Jet and Accretion Disc	68
7.1.3	A Smaller Black Hole?	68
7.2	NGC 1097	69
7.2.1	Model Consistency	69
7.2.2	A Highly Magnetised Outflow	69
7.2.3	Jet and Accretion Disc	70
7.2.4	Modelling the Spectrum I - Inflow or Outflow	71
7.3	NGC 1052	73
7.3.1	Model Consistency	73
7.3.2	Magnetic Launch from a Huge Base?	73
7.3.3	Jet and Accretion Disc	75
7.3.4	Energetic Reasons for Truncation	76
7.3.5	Modelling the Spectrum II - Inflow or Outflow	77
7.4	Synthesis	78
7.4.1	Comparing to the modelling of other LLAGNs - Breaking Degeneracies	78
7.4.2	Elusive Accretion Discs - Truncated and Concealed	80
<b>8</b>	<b>Conclusion</b>	<b>83</b>
<b>Appendix A Appendix</b>		<b>85</b>
A.1	Eddington Limit	85
A.2	Special Relativity	85
A.2.1	Lorentz Transformations	85
A.2.2	Relativistic Doppler Effect and Apparent Velocity	86
A.2.3	Aberration	87
A.2.4	Beaming	87
A.3	Free-Free Emission	88
A.3.1	Derivation with the Weak Encounter Concept	88
A.3.2	Free-Free Absorption	90

A.4 Residual Plots . . . . .	90
<b>Constants and Units</b>	<b>93</b>
<b>Bibliography</b>	<b>94</b>
<b>Erklärung</b>	<b>105</b>



# Introduction

With the first "Observation of Gravitational Waves from a Binary Black Hole Merger" not only Einstein's prediction of gravitational waves one century earlier was confirmed, but also black holes were directly observed for the first time (Einstein 1916, 1918; Abbott et al. 2016). Even though there has been strong belief in black holes for some decades (e.g. Rees 1984), the detection confirmed their existence for their first time.

Black holes of stellar masses are found in binary systems, where either indirect observations by investigation of their visible companion, or direct observations of their interaction are possible. For example Cygnus X1 consists of a star and a black hole orbiting each other. The latter accretes material of the former, accompanied by outflows.

On the other mass end, we believe that every massive galaxy harbours a supermassive black hole (SMBH). Some of them are quiet, like our central SMBH Sagittarius A\*, while others are active: They accrete and release energy, forming active galactic nuclei (AGNs). AGNs channel energy into their host galaxy via outflows and radiation. The deposition of energy in the interstellar medium (ISM) is generally known as feedback. It can trigger shocks, produce turbulence, or heat the ISM - all effects which modulate star formation activity and therefore determine galaxy evolution.

Feedback is an crucial ingredient to correctly predict galaxy evolution in cosmological simulations. Recent studies show that the most numerous class of AGNs in the local universe are low luminosity AGNs (LLAGNs), whose dominant energy output is likely carried by jets: collimated outflows of energetic particles, which could even exceed the feedback of supernovae. Observations show tight relations between AGNs and their host galaxies, which suggest self regulated mechanisms connecting e.g. bulge- and SMBH-growth (Håring and Rix 2004).

In spite of their huge differences in masses, black holes seem to follow a mass scaling relation; the so-called fundamental plane of black holes shows a correlation between black hole mass, radio luminosity and X-ray luminosity (Merloni et al. 2003). Black holes accreting highly sub Eddington seem to follow a certain relation over the entire mass range from tiny stellar black holes up to giant black holes of billions of stellar masses. The processes involved around stellar black holes in the hard state seem to be similar to the processes at seen at their large dim brothers (LLAGNs). This suggests a certain degree of scale-invariance of in- and outflow mechanisms. But which mechanisms are responsible is poorly understood - a closer view reveals many open questions. In contrast to the unified scheme for AGNs, where it is believed that around the black hole forms an accretion disc and further outside a torus, LLAGNs seem to neither show evidence for a typical accretion disc nor a torus (Ho 2008). How then do the central engines receive energy? Which effects are triggering the launch of jets and provide their power provided? What is the origin of the emission in the infra-red (IR)?

Despite the lack of knowledge about the full physical picture, the above mentioned scaling of black holes over the entire mass-range is a starting point for developing numerical models; specifically in the case of LLAGNs models of jet-like outflows. Both, validating or falsifying these models by comparing them with observational data, in turn offers the possibility to study the ongoing physical processes in the vicinity of black holes.

However, faint objects like LLAGNs are difficult to observe. The host galaxy typically outshines the nucleus and thus, observational data can be contaminated by stellar light of

the host galaxy. In order to minimise this issue, observations of highest angular resolution are necessary - ideally over the entire electromagnetic spectrum. Unfortunately today only a handful of few nearby objects in the sky offer the possibility to image them with sub-arcsec resolution over nearly 10 orders of magnitude in frequency. But uncovering the innermost nuclear region in multiple frequency-bands for those objects generates the unprecedented opportunity to directly study their spectral characteristics.

In this thesis a semi-analytical numerical model, focusing on jet emission, is applied to a sample of three nearby LLAGNs, whose observational spectra consist out of highest angular resolution images available over nearly the entire electromagnetic spectrum. Especially the availability of high angular resolution data in the IR allows to test the model in a critical frequency range. The model application to individual LLAGNs offers an complementary approach to gain insight into the radiative nature of the observed emission. The characterisation of individual objects extends the sample of objects already studied using the same technique. In the long term this will allow to study a large statistical sample. This will contribute to a better understanding of the physical mechanisms in the vicinity of black holes. Specifically to the understanding of accretion and jet formation, as well as their scaling over the mass range and their interaction with the environment. This in turn will consolidate and improve the modelling of AGN-feedback in cosmological simulations.

This thesis proceeds as follows: Chapter 1 briefly describes the recent understanding of AGNs, and then focusses on LLAGNs. Chapter 2 defines radiative quantities and introduces the main mechanisms for thermal emission and the non-thermal radiative processes such as synchrotron and inverse Compton radiation. Chapter 3 motivates and introduces the jet-disc model. In Chapter 4 the sample is presented. Each individual object under investigation is briefly characterised and its observational data is described. Chapter 5 focuses on the application of the model to the data, and develops the framework for further analysis. Chapter 6 contains the results of modelling, chapter 7 discusses these results and their implications - individually and the overall trends compared to former investigations. It discusses the important results and puts them in context of the recent theoretical scenario. Chapter 8, the conclusion, emphasises the findings of this work.

# Chapter 1

## Active Galactic Nuclei

The first discovery of a quasi-stellar radio source (Quasar)<sup>1</sup> in 1963 was the starting point for the recognition of a new class of objects: active galactic nuclei (AGNs; Schmidt 1963; Oke 1963). The high brightness, together with the far distance implied an extremely high luminosity ( $\sim 10^{46}$  erg s<sup>-1</sup>), which seemed unlikely to be powered by mass-to-energy conversion by nuclear fusion, especially since furthermore the emission region appeared too small (e.g. Peterson 1997; Rees 1984). The release of gravitational energy of matter falling deep into the gravitational potential of a very compact body can be far more efficient. In the last decades the scientific consensus evolved subsequently and led to the current picture of AGNs: At the centre there is likely a supermassive black hole accreting matter (e.g. Kormendy 2004). Gravitational energy release ultimately supplies all forms of radiation and outflows of the AGN (Shakura and Sunyaev 1973; Rees 1984).

Today it is believed that AGNs -observed in various manifestations, the "zoo of AGN"-obey intrinsically similar characteristics. An attempt to reconcile their variety was done by the development of the unified scheme of AGNs (Antonucci 1993; Urry and Padovani 1995).

The section 1.1 will list the basic components according to the unified scheme and introduce some general definitions. In section 1.2 the distinction criteria and the resulting classification system of the unified scheme will be presented. In section 1.3 we will focus on the subclass of low luminosity AGNs (LLAGNs), which are under investigation in this work. Specifically weakly accreting LLAGNs with jets will be described in greater detail, by comparing their spectra to other types of AGNs and exploring their fundamental differences.

### 1.1 Unified Scheme

According to the unified scheme (Antonucci 1993; Urry and Padovani 1995), illustrated in figure 1.1), AGNs typically have a number of components in common:

- Supermassive black hole in the centre
- Accretion disc around the supermassive black hole
- Broad line region (BLR) in vicinity of the Accretion disc
- Torus confining the inner central region
- Narrow line region (NLR)
- Jet emanating from the central region

---

<sup>1</sup>A star-like appearing object in the optical, to which (extended) radio emission is attributed.

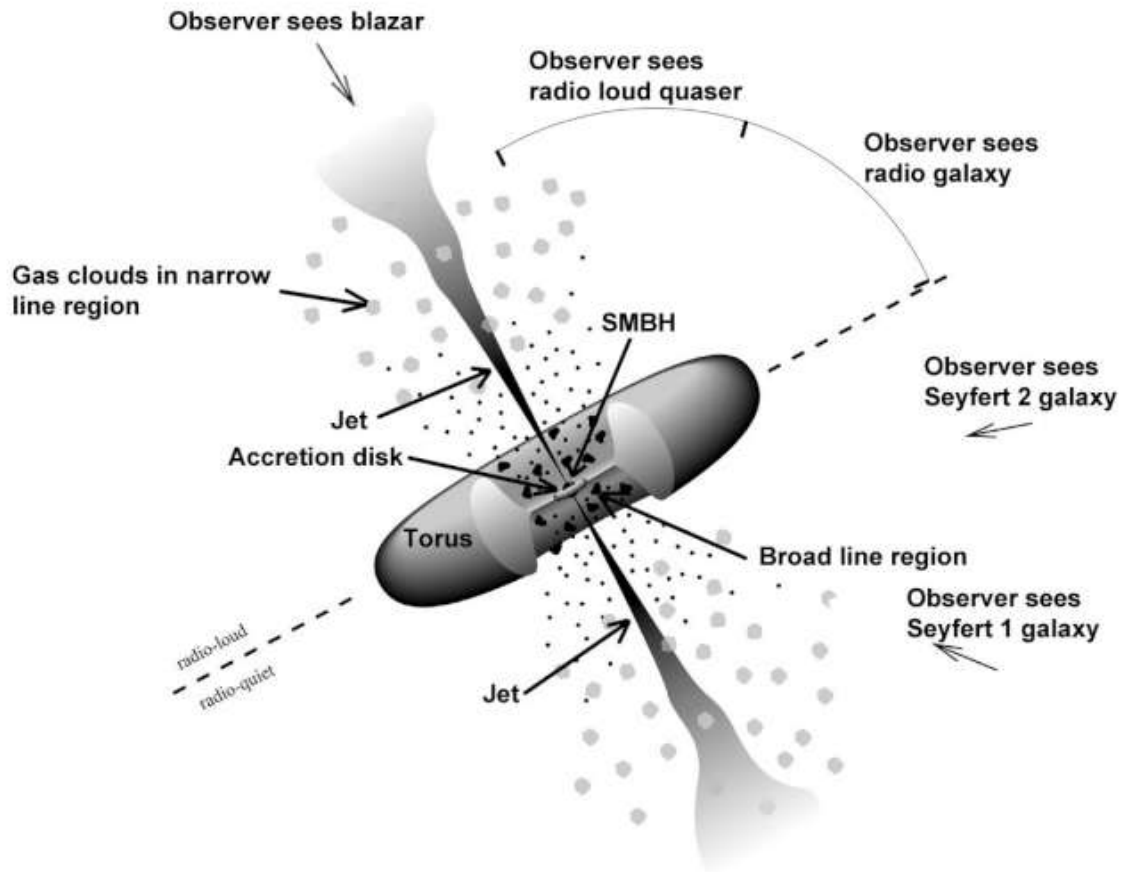


FIGURE 1.1: The unified scheme for AGN. Courtesy NASA (after Urry and Padovani 1995).

### 1.1.1 Supermassive Black Hole

The supermassive black hole, typically with a mass of  $10^6 - 10^9 M_{\odot}$  (e.g. Shankar et al. 2004) is the dominant central attractor. A characteristic physical scale in AGNs is its gravitational radius<sup>2</sup>

$$r_g = \frac{GM}{c^2} \quad (1.1.1.1)$$

where  $M$  denotes the central mass,  $G$  is the gravitational constant, and  $c$  is the speed of light. Within the framework of general relativity, a non rotating black hole has its event horizon at the Schwarzschild radius  $r_s = 2r_g$ .

### 1.1.2 Accretion Disc

Matter collapsing onto the black hole settles into a geometrically thin disc, due to gravity and conservation of angular momentum (e.g. Shakura and Sunyaev 1973).

The canonical geometrically thin and optically thick (Shakura Sunyaev) accretion disc gives rise to a multi-temperature black body spectrum, contributing especially in the ultraviolet (UV) - the so-called blue bump. Briefly, its composite spectrum is the superposition of infinitesimal ring shaped black bodies, becoming hotter at smaller radii. The basic idea is to locally convert a fraction of the released gravitational potential energy into black body radiation. A viscosity prescription results in torques, which transport angular momentum outwards. That enables matter to spiral further in, providing the mass supply for the AGN.

<sup>2</sup>An useful number to remember: the gravitational radius of a solar mass is around 1.5 km.

An important quantity connected to accretion is the Eddington limit

$$L_{\text{edd}} = \frac{4\pi c m_p G}{\sigma_T} M \quad (1.1.2.1)$$

where  $m_p$  is the proton mass and  $\sigma_T$  the Thomson cross section (see [subsection 2.5.1](#)). Under idealised assumptions, this is the maximum luminosity  $L_{\text{edd}}$  a source of mass  $M$  can emit (see [A.1](#)). It is common to express the luminosity of AGNs in terms of the Eddington luminosity.

### 1.1.3 BLR, Torus and NLR

Above and below the accretion disc there are quickly moving gas clouds, due to their proximity to the black hole ( $10^{16}$  cm– $10^{18}$  cm). They, and perhaps the disc itself give rise to widely Doppler-broadened emission lines (typically  $\Delta v_{\text{FWHM}} \sim 5000$  km s $^{-1}$ , e.g. [Peterson 1997](#)), forming the BLR.

Outside the accretion disc and the BLR a dusty, clumpy and/or gaseous torus of typically parsec-scale size ( $\sim 10^{17}$  cm) surrounds the central region, presumably with similar orientation as the disc. The material shields radiation from the inner region and gives rise to thermal emission in the infra red (IR).

In the polar regions (with respect to disc and torus) within a broad opening cone, i.e. where no impenetrable torus shields from the ionising nuclear radiation, there exists a region of slowly moving gas (compared to the BLR) at a distance of several parsecs ( $10^{18}$  cm– $10^{20}$  cm). The detection of forbidden line emission of the NLR indicates low particle densities.<sup>3</sup>

### 1.1.4 Jet

Inflows are frequently accompanied by outflows. High velocity material and/or relativistic effects in the vicinity of the black hole wind up any present magnetic field lines. They are amplified until the overcritical magnetic pressure channels particles to the polar regions, where they are accelerated and expelled. This leads to polar outflows of relativistic particles. The outflows are further collimated by magnetic fields and thus give rise to synchrotron emission. A detailed explanation is not the scope of this work, but a few possible mechanisms are noted in [subsection 1.3.2](#).

The lengths of AGN jets range from few parsecs up to several hundreds kilo-parsecs, exceeding the size of their host galaxy. They are observed in various morphologies.<sup>4</sup> Jets can carry large amounts of kinetic energy which they release into their environment. Thus they modulate the star formation activity and determine the galaxy evolution of their host galaxy. This deposition of energy -generally known as feedback- is a crucial ingredient to correctly predict galaxy formation in cosmological simulations (e.g. [Steinborn et al. 2015](#)).

## 1.2 Taxonomy

The components described above (jet, torus, disc, corona), give rise to a remarkably featureless spectrum. This is a general characteristic of AGNs ([Peterson 1997](#)). Many various observational manifestations (AGN zoo) can be explained by the unified scheme.

<sup>3</sup>For higher densities the excited particles would relax via collisions.

<sup>4</sup> There are jets, whose emission is dominated by so-called hot spots, regions far away of the centre with highest surface brightnesses (FR II), and others, where the central surface brightness is highest (FR I) ([Fanaroff and Riley 1974](#)).

As indicated in [figure 1.1](#), the radio loud and radio quiet dichotomy offers one attribute for classification. Radio loud AGNs appear to have relatively strong radio emission. This is indicative for a compact radio core or jet.<sup>5</sup> The introduced dichotomy by categorizing AGNs into two groups is not based on physical reasons, but an indicative criteria since radio loudness may be related to internal properties (e.g. black hole spin, host galaxy conditions).

Already Carl Seyfert described the occurrence of both broad and narrow emission lines in the centres of nearby galaxies ([Seyfert 1943](#)). The differentiating factor which separates so-called type 1 from type 2 AGNs is the presence or absence of the BLR in direct observations. The unified scheme argues, that when observing AGNs from an fairly edge on angle, neither the accretion disc nor the BLR can be observed directly, because the torus intercepts the line of sight (type 2). However, the (indirect) detection of the BLR is in some cases possible by observing polarised (scattered) light emanating from the NLR, unveiling its existence. The distinction between type 1 and type 2 AGNs is solely an orientation effect. Today the strict type distinction is used in an extended, more detailed fashion for mixed appearance, e.g. type 1.9 (partially broad lines).

A third qualitative but illustrative criterion for classification is their luminosity, where they are labelled by approximately distinguishing between high, intermediate, and low luminosities. For a high luminosity the AGN outshines the stellar light of the host galaxy, resulting in the detection of a quasi stellar object; for an intermediate luminosity the AGN is visible as the bright point-like central region, according to the unified scheme. For a low luminosity the AGN is no prominent optical feature of the galaxy. Typically the nuclear region shows characteristic emission lines of low ionised atoms and is called low ionisation nuclear emission region (LINER, [Heckman 1980](#)), which distinguishes them from the intermediate class.<sup>6</sup>

According to these attributes the following labelling occurs for different manifestations sorted from high to low luminosity: Quasi stellar objects are at the upper luminosity end. They are distinguished into radio loud Quasars and radio quiet Quasars (QSO). These objects have bright continuum emission, a BLR, and belong to type 1. Their type 2 counterparts are not clearly identified but might be IR-luminous AGNs. Radio loud AGNs of intermediate luminosities are called broad line radio galaxies (BLRGs) or narrow line radio galaxies (NLRGs). Their radio quiet counterpart are so-called Seyferts, type 1 or 2. LINERs are distinguished into type 1 or 2, similarly to Seyferts.

Towards lower luminosities, likely linked to lower accretion rates, the radio loudness typically increases ([Sikora et al. 2007](#)). Indeed, radio loudness and therefore the existence of compact radio cores and parsec scale jets seems to be a general property of LLAGNs ([Ho 1999](#); [Nagar et al. 2005](#)).

### 1.3 Low Luminosity AGNs

In spite of their low luminosity ( $L_{\text{bol}} \lesssim 10^{42} \text{ erg s}^{-1}$ ;  $L_{\text{bol}}/L_{\text{edd}} \lesssim 10^{-3}$ , [Ho 2008](#)), they should be treated as key objects within the zoo of AGNs. While AGNs draw attention by their Quasar state only during short intervals of their lifespan, they spend most of their time in rather low activity states ([Greene and Ho 2007](#)). Indeed, the majority of the nearby galaxies with identified AGNs host an LLAGN, corresponding to an  $\sim 1/3$  of all galaxies in the Local Universe ([Ho 2008](#)).

<sup>5</sup>Radio loudness was originally attributed for Quasars when the flux at 5 GHz is at least one order of magnitude larger than the flux at 440 nm,  $F_{5 \text{ GHz}}/F_{440 \text{ nm}} \gtrsim 10$  ([Kellermann et al. 1989](#)).

<sup>6</sup>The distinction between Seyfert galaxies and LINERs is the strength of the line ratio ( $[\text{OIII}]\lambda 5007/\text{H}\beta = 3$  ([Veilleux and Osterbrock 1987](#)). Low luminosity AGNs are frequently associated with LINERs ([Ho 2008](#)). The unified scheme does not include low luminosity AGNs.

Already their missing radio quiet counterpart casts doubts on whether the unified scheme can be simply extended to LLAGNs. They are not scaled-down Seyferts or radio galaxies - their central engines undergo fundamental changes. LLAGNs typically share some observational characteristics: harboured in a LINER; missing spectral footprint of the blue bump and weak or absent iron  $K\alpha$  line<sup>7</sup> - indicating to lack a standard accretion disc in the very vicinity of the black hole; disappearing BLR; vanishing torus; a compact radio core and parsec scale jet (Ho 2008). This jet carries the main energy output of the LLAGN, which might exceed the feedback contribution from supernovae in the host galaxy (Nagar et al. 2005; Ho 2008; Heckman and Best 2014).

### 1.3.1 Spectral Energy Distribution compared to Seyferts and Quasar

In particular, high resolution spectral energy distributions (SEDs)<sup>8</sup> of individual LLAGNs illustrate, that there is neither evidence for a standard accretion disc, nor for a mid-IR bump associated with thermal emission of the torus. Instead, the continuum emission from radio to UV which is expected for non-thermal emission mechanisms, e.g. synchrotron emission of a jet (Markoff 2010; Fernández-Ontiveros et al. 2013). This suggests, that the main radiative output of LLAGNs is dominated by non-thermal processes.

In figure 1.2 the SEDs of (averaged) Seyfert 1 and Seyfert 2, a radio loud quasar (RL QSO 3C273), and three LLAGNs are shown. The LLAGNs -NGC 4594, NGC 1097, and NGC 1052- will be investigated in this work.<sup>9</sup> Both Seyferts show a well pronounced peak in the mid-IR around  $20 \mu\text{m}$ . In that region the LLAGNs share approximately the same normalised flux level. When inspecting the normalised radio fluxes, they are higher for Quasar and LLAGNs than for the Seyferts. More importantly, when starting at radio frequencies and going towards higher frequencies, for the LLAGNs and the Quasar the radio trend continues up to their mid-IR emission, while both Seyferts show a rise towards their peak. The flux of the "louder" Seyfert 1 increases from radio (e.g. 10 GHz) towards the mid-IR by approximately one order more than the LLAGN with the relatively weakest radio flux of the sample, NGC 1097. None of the LLAGNs show a similarly well defined, thermal-like peak (compare figure 3.2). From the peak towards the near-IR both Seyferts show a similar flux decrease down to  $2 \mu\text{m}$ . Only NGC 5128 shows comparable behaviour. Going towards visible (VIS) and comparing both Seyferts, one notices the significantly stronger emission extending up to the UV for the average Seyfert 1. This feature is indicative for an accretion disc. While the same feature is visible for the radio loud Quasar 3C273, there is no evidence for that in the spectra of the LLAGNs. They seem to rather follow a power law from mid-IR to UV. Only NGC4594 shows an excess in the near-IR, but this is not continued in the UV.

Summing that up, both Seyferts show a spectrum indicative for dominant thermal dust emission in the mid-IR. There is no clear signature for dust emission of a torus in the LLAGNs, indicating that this is at least not the dominant emission process which defines the spectrum. There is no footprint for a standard accretion disc. The quite flat and strong spectrum of LLAGNs from radio to mid-IR and the power law shape from IR to UV is rather similar to the spectrum of the Quasar and indicative for jet emission.

<sup>7</sup>The iron  $K\alpha$  fluorescence line is an indicator for optically thick material, irradiated by hard X-rays. If its shape is distorted by Doppler broadening and relativistic effects, it is likely to originate from an inner accretion disc.

<sup>8</sup>Technically speaking, the spectral plots in this work show always the spectral flux density versus frequency, not the spectral energy. However, throughout this work the term SED will be used equivalently.

<sup>9</sup>Their SEDs will be shown individually in chapter 4. Here the attention shall be drawn rather on the overall spectral shape.

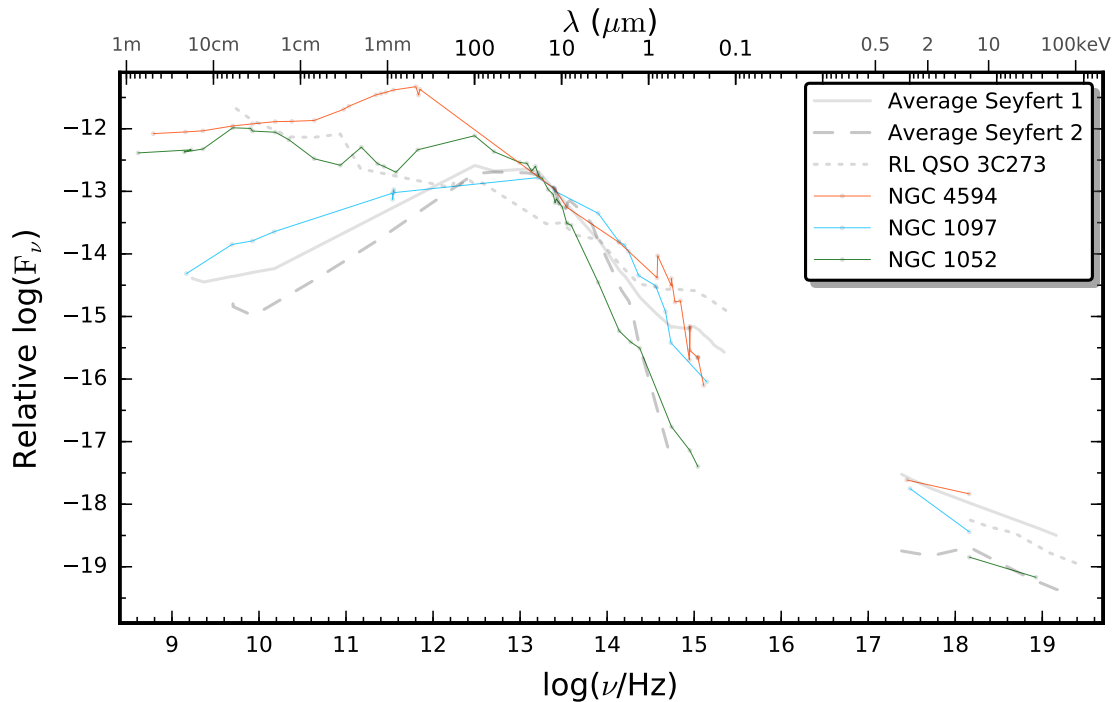


FIGURE 1.2: High angular spectral energy distributions (SEDs) of averaged Seyfert type 1 (grey line) and Seyfert type 2 (grey dashed) nuclei and the radio loud Quasar 3C273 (grey dotted), templates from [Prieto et al. \(2010\)](#); [Elvis et al. \(1994\)](#). Additionally the high angular SEDs of the LLAGNs, NGC 1052, NGC 4594, and NGC 1097 are over-plotted in colour. All spectra are normalised by their average power ( $\langle \nu F_\nu \rangle$ ) to achieve approximate visual agreement. Due to absorption by galactic hydrogen between UV and soft X-rays there is no observational data and no interpolation is included. (The product of frequency and corresponding flux is calculated at each data point and summed up. The value obtained is then divided by the number of data points, resulting in the averaged power.)

### 1.3.2 Differences to the Standard Picture

The missing accretion disc feature in the spectrum, together with the missing iron  $F\alpha$  line, pose general limitations on the presence of an accretion disc. These observations hamper a standard, geometrically thin and optically thick disc, which extends inwards to the innermost stable circular orbit.

Indeed, below a certain accretion rate, the low density of the disc does not longer provide enough gravitational stabilisation. Additionally, the low optical thickness<sup>10</sup> prevents efficient cooling. As a result pressures dominate below a certain distance and "puff up" the disc at a certain (truncation) radius ([Ho 2008](#)). Inside of the truncation radius the accretion disc is converted into a radiatively inefficient accretion flow (RIAF). It is a hot, geometrically thick (quasi-spherical) and optically thin flow, whose main feature is its low mass to light conversion efficiency.

One popular manifestation of this kind of flows is the advection dominated accretion flow (ADAF, see [Narayan and Yi 1995](#)). A significant fraction of hot material is advected<sup>11</sup> into the black hole, before it can radiate away its released potential energy ([Yuan and Narayan 2014](#)). These hot and inefficient flows naturally "solve" the spectrally missing blue bump in weakly accreting black holes.

<sup>10</sup>See [subsection 2.1.2](#) for optically thick-thin.

<sup>11</sup>Transported together with its heat energy.

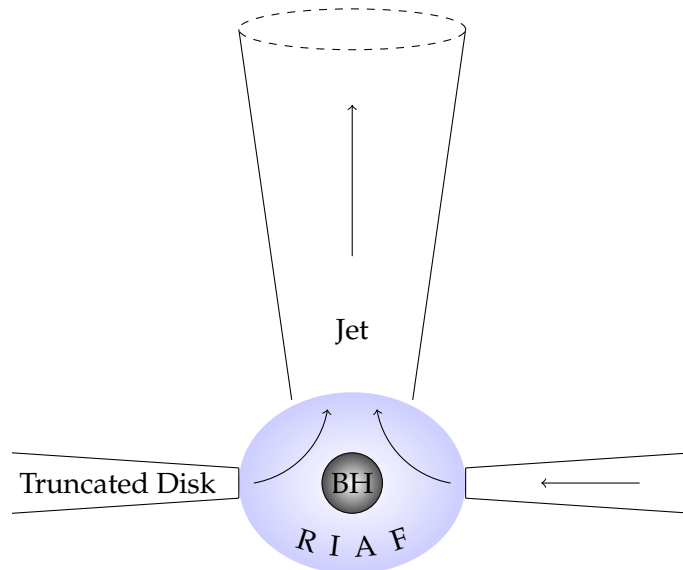


FIGURE 1.3: Cartoon of the accretion scheme for LLAGNs. For small accretion rates the inner region of the thin accretion disc vanishes and is converted into a puffed-up, radiatively inefficient accretion flow (RIAF), which channels/helps channelling particles into polar regions, where a jet is launched (only one side of the jet shown). The arrows illustrate the route of matter which enters the jet. Inspired by (Ho 2008). Graphic created with TikZ.

Besides AGNs, similar things seem to appear at the other extend of the mass range in black hole X-ray binaries (BHXBs). While their so-called soft state is characterised by high accretion rates ( $\gtrsim 1.5\%L_{\text{edd}}$ ), and a strong thermal spectrum - well described by the standard thin disc, their hard state is found at lower luminosities (Yuan and Narayan 2014). This state is spectrally dominated by a hard power law and shows compact and steady jets (Markoff 2010). These parallels suggest that the basic mechanisms around black holes are similar over the entire mass range.

Independent of their mass, RIAFs and the launch mechanism seem to be intimately linked (Narayan and Yi 1995; Ho 2008, and references therein). In particular RIAFs seem to facilitate the launch by large scale poloidal magnetic field components and support the collimation of outflows (e.g. Rees et al. 1982). The poloidal field has another implication. General relativity predicts the so-called frame dragging effect: A rotating black hole twists up the space-time in its close environment. Within a certain distance particles and light are forced to co-rotate; the so-called ergosphere (Rees 1984). Poloidal magnetic fields in the ergosphere of the black hole are wound up and create a strong toroidal field. These fields trigger an effect known as the Blandford-Znajek mechanism (Yuan and Narayan 2014). The Blandford-Znajek mechanism results in a Poynting flux from the black hole, i.e. it extracts rotational energy in electromagnetic form (Blandford and Znajek 1977).<sup>12</sup> Simulations show, that this effect is naturally capable of explaining relativistic jets. Weaker, quasi relativistic jets may be driven by (a combination of this and) other effects which extract energy from the accretion flow, e.g. the model of Blandford and Payne (1982) (Yuan and Narayan 2014).

Independent of the actual effects, non-thermal emission processes are expected to play an important role in LLAGNs and therefore are likely to contribute to the observed continuum emission. To distinguish between the different mechanisms which could be radiatively dominant, models with focus on predictions of the continuum emission can be tested versus measurements. However, the expected spectral shape of the particular processes is

<sup>12</sup>See section 2.3 for Poynting flux.

very different. While models for RIAFs (including ADAFs) must be complemented by an additional jet component, we believe that models consisting of a detailed description of a compact jet and a thin truncated disc component -as the model which will be used here- can capture most complexity shown by the SEDs of LLAGNs.

## Chapter 2

# Radiative Processes

As pointed out in [chapter 1](#), non-thermal processes are an important contribution to the radiation in the vicinity of the SMBH. Synchrotron emission and inverse Compton scattering are fundamental processes which produce non-thermal radiation.

Section 2.1 introduces basic principles of radiation, specifically radiative quantities and radiative transfer are briefly defined. In [section 2.2](#) the Planck formula and connected important relations are stated. From first principles of electrodynamics the Larmor formula is derived in [section 2.3](#). Starting with this formula, [section 2.4](#) presents the derivation of synchrotron emission and ends with characteristic SED shape associated with the emission from a compact jet. Also, starting with the Larmor formula, [section 2.5](#) describes Thomson scattering, the scattering of a photon off a relativistic electron, the Compton spectrum, and synchrotron self Comptonisation (SSC). Free-free emission (Bremsstrahlung) and absorption are discussed in a similar fashion in [A.3](#). All constants involved are tabulated in the end of this work. If not stated otherwise, SI units are used.

## 2.1 Radiative Basics

### 2.1.1 Intensity, Flux and Luminosity of Isotropic and Lambertian Sources

Before talking about radiative processes, radiation should be defined quantitatively. The task is in detail to create connections between measurements of an observer, quantities of the macroscopic source, and microscopic emission and absorption processes within that source.

The definitions below can be found in many textbooks about radiative processes. However, the description here aims at providing a straight forward and complete framework to follow the investigation within this work. The entire section is inspired by [Mihalas \(1978\)](#) and [Ghisellini \(2013\)](#). In the first part all quantities are considered to be spectral, i.e. referring to a certain frequency. To yield observable it will be necessary to consider quantities in a certain frequency interval, but it is not important at which step the spectral integration is done. Within the basic definitions a special case is also mentioned, the case of a Lambertian surface. This will be important for further analysis, and is presented here already.

The specific intensity is the basic and most useful radiative quantity, since it incorporates all the information necessary to characterise radiation completely. Therefore all quantities of interest can be derived from it. The specific intensity, sometimes called spectral radiance, depends, on the frequency  $\nu$ , the considered direction, and the position in space. In more detail the specific intensity is the spectral energy per time interval,  $d^2 E / (d\nu dt)$ , emitted from (equivalently passing through) a projected unit surface element  $dA_{\perp} = dA \cos \theta$  into a certain direction  $d\Omega$ . Hence the spectral intensity is defined as

$$I_{\nu} = \frac{d^4 E}{d\nu dt dA \cos \theta d\Omega} \quad (2.1.1.1)$$

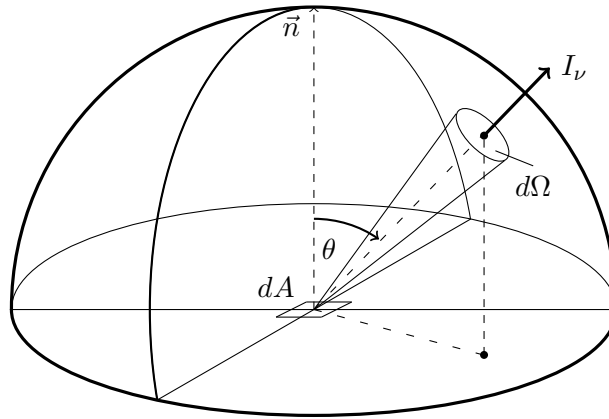


FIGURE 2.1: A scheme to illustrate the radiative quantities.  $I_\nu$  is the specific intensity, i.e. the spectral energy  $dE/d\nu$  passing the projected area element  $dA_\perp$  into the solid angle  $d\Omega$  per time  $dt$ . For clarity only  $dA$  is drawn in the figure. Considering energy conservation, the total power permeating the area upwards must equal the total power going through the overlying hemisphere. Graphic created with TikZ.

Its unit is  $[\text{W m}^{-2} \text{ Hz}^{-1} \text{ sr}^{-1}]$ . It is a directional quantity, but here directly the projection onto the unit surface element is considered, to keep it as clear as possible. The projection term  $\cos \theta$  ensures that the quantity is independent of the orientation of the unit surface element, since an inclined area is permeated by less rays and the specific intensity would depend on the orientation.

The specific flux is the total energy per time originating from (or equivalently passing through) a unit surface element into a certain direction cone  $d\Omega$ . Here we discuss two different cases: In the first case, we consider the specific flux permeating the unit surface area of the source itself. In the second case, the receiving unit surface is located at a distance  $R$  from the source - the case for a detector.

In the first case the flux directed into the entire surrounding sphere is considered. Then the specific intensity must be integrated over the surface of the sphere. In spectral notation

$$F_\nu = \int_{\Omega} I_\nu \cos \theta d\Omega \quad (2.1.1.2)$$

This is the specific flux permeating the surface unit element at the element of consideration. No distinction is made between radiation permeating upwards or downwards. In contrast for the calculation of the flux at the surface of a radiating source, only the overlying hemisphere is irradiated. Then the solid angle integral is carried out over the overlying hemisphere.

Now a particularly special surface is introduced: A Lambertian source has a constant specific intensity independent of inclination  $I_\nu(\theta) = I_0$ . A flat Lambertian surface is equally bright when observed from different directions. However, the flux emitted into a certain direction scales with  $\cos \theta$ . This corrects for the projection of the surface, because the projected area is smaller for high inclinations. The following flux passes through the surface of a Lambertian source into the integrated overlying hemisphere:

$$F_\nu = \int I_0 \cos \theta d\Omega = 2\pi \int_0^{\pi/2} I_0 \cos \theta \sin \theta d\theta = \pi I_0 \quad (2.1.1.3)$$

Here azimuthal symmetry is used which contributes  $2\pi$ .

Turning to the second case: We consider a unit area at a distance  $R$  from the source,

and want to calculate the crossing flux. This is equal reversing the thought direction of the rays: Instead of the flux passing the area into a solid angle, the flux originates from a source occupying a solid angle and is received from the observer's detector area. This is the usual case in astrophysical measurements. The limits of integration are the solid angle subtended by the source as seen from the observer  $\Delta\Omega = A/R^2$ , where  $A$  denotes the into the plane of the sky projected area of the source, and  $R$  is the distance between source and observer. Instead of integrating one can multiply the specific intensity with the solid angle, valid if the flux is constant over the source and the solid angle is sufficiently small. The Lambertian flux emitted in the solid angle  $\Delta\Omega$  at inclination  $\theta$  is:

$$F_\nu(T) = \Delta\Omega I_0 \cos\theta \quad (2.1.1.4)$$

We also describe here the case of isotropic radiation: a source emitting a constant flux in each direction radiates isotropically, e.g. a spherical Lambertian source or a point source. It holds  $F_\nu(T) = \Delta\Omega I_0$ .

The luminosity quantifies the radiative power that a source emits. To obtain the luminosity  $L$  two different, but equivalent, calculations can be carried out: either the total spectral flux emitted per unit area element is integrated over the surface of the source. Alternatively the flux crossing a sphere of radius  $R$  enclosing the source is integrated over its surface.

The luminosity is no a spectral quantity, since it denotes the total power emitted by a source in a certain frequency interval  $[\nu_1, \nu_2]$ . Thus at this step the spectral integration of the flux is carried out,  $F = \int_{\nu_1}^{\nu_2} d\nu F_\nu$ .

In the case of a Lambertian plane surface we carry out the calculation over the emitting surface. For a Lambertian plane surface of area  $A$  one gets  $L = \int_A F dA' = \pi I_0 \int_A dA' = 2\pi I_0 A$ , when considering both sides of the surface with a constant flux  $F = \pi I_0$  (see [equation 2.1.1.3](#)). For an isotropic emitting source, the flux evaluated at the spherical surface is constant, hence:

$$L = 4\pi R^2 F = 4\pi R^2 \Delta\Omega I_0 = 4\pi A I_0 \quad (2.1.1.5)$$

By comparing both results one notices that the flux from a face-on Lambertian plane surface has half of the luminosity when compared to an isotropic source.

### 2.1.2 Radiative Transfer: Optically Thick versus Thin

Now the focus is changed towards the interaction of radiation with matter. A medium releasing radiation possesses a certain emissivity. The latter is the power integrated over frequency produced in a volume and radiated to a certain direction,  $j = d^2L/(dV d\Omega)$ . In the case of isotropic radiation the emissivity can be described as:  $j = 1/(4\pi)dL/dV$ . This is the most relevant quantity related to microscopic emission processes. The emissivity can also be described as:

$$j = \frac{nP}{4\pi} \quad (2.1.2.1)$$

where  $n$  denotes the density of emitting particles and  $P$  is the power emitted by an individual particle. Analogously instead of density times power, the number of emission events per time and the corresponding released energy can be multiplied.

On the other hand particles can absorb the radiation field. For simplicity, scattering is not considered. For further purpose  $\alpha_\nu$  and  $j_\nu$  represent spectral absorption and emissivity,

respectively. To describe the processes of extinction and emission along a certain infinitesimal path  $ds$  the radiative transfer equation is

$$\frac{dI_\nu}{ds} = -\alpha_\nu I_\nu + j_\nu \quad (2.1.2.2)$$

The change of the specific intensity in a medium is due to attenuating absorption proportional to the intensity itself and emission into the path by the medium itself. The coefficient  $\alpha_\nu$  is related to the cross section  $\sigma_\nu$  and density  $n$  via  $\alpha_\nu = n\sigma_\nu$ . The optical thickness is defined as  $\tau_\nu = \int_S ds\alpha_\nu(s)$ .

A general distinction shall be made right here: The difference between optically thin and thick sources. The former means that the optical thickness is small,  $\tau_\nu \ll 1$ , hence absorption within the source is negligible. This implies for an optically thin medium that the intensity at the surface into a certain direction is simply the integral of the emissivity along the path through the source. Optically thick means that the free path length of a photon is much smaller than the size of the source,  $\tau_\nu \gg 1$ . Radiation is reprocessed in the source: Absorption and re-emission redistribute the radiation inside. The radiation leaving the source is effectively arising from the surface layer of the source from  $\tau_\nu \sim 1$ .

When the optical thickness increases, the energy exchange by absorption and emission inside the source becomes more efficient. If energy transfer establishes the so called local thermal equilibrium (LTE) for a certain volume in the source, there is no net energy flow towards or outwards the volume,  $dI_\nu/ds = 0$ . Absorption and emission are balanced. This is sort of the statement of Kirchhoff's law regarding thermal emission, while the real result is even stronger: emission and absorption are even balanced for arbitrary directions and in general holds  $I_\nu = j_\nu/\alpha_\nu$ . Within a thick source a thick volume element absorbs all the received radiation. It absorbs an isotropic surrounding radiation field. Consequently, it re-emits isotropically. Independent of its shape, it is equally bright from each viewing angle. Thus an optically thick medium is Lambertian. Additionally, a perfect absorber is a perfect emitter. By definition, a black body has an absorption coefficient of unity at all wavelengths. Inversely no source in LTE can emit radiation more efficiently at a given temperature than a black body. From another perspective: An optically thick source in thermal equilibrium with its environment absorbs all received radiation, it is black. Hence in general, an optically thick source in thermal equilibrium emits as a black body. Its specific intensity is given by Planck's law [equation 2.2.0.1](#), and it holds

$$B_\nu(T) = \frac{j_\nu}{\alpha_\nu} \quad (2.1.2.3)$$

Here  $B_\nu(T)$  is the usually used letter to denote black body radiation, whose spectrum solely depends on temperature.

## 2.2 Black Body Emission: Planck, Rayleigh-Jeans and Stefan-Boltzmann

When a thermal source is optically thick, its absorption and emission coefficients are unity and it is called black body radiator. Its specific intensity obeys the Planck formula, usually denoted by  $B_\nu$  (instead of  $I_\nu$ ), and stated here in frequency representation,<sup>1</sup>

$$B_\nu(T) = \frac{2h}{c^2} \frac{\nu^3}{e^{h\nu/k_B T} - 1} \quad (2.2.0.1)$$

<sup>1</sup>Throughout the work all calculations will be strictly in the frequency representation.

where  $h$  is Planck's constant,  $k_B$  is the (Ludwig) Boltzmann constant and  $c$  the speed of light (e.g. [Rybicki and Lightman 1979](#)). The Planck formula connects the specific intensity with frequency  $\nu$  and temperature  $T$ . The distribution peaks at  $\nu_{\max} = \tilde{x}k_B T/h$  with the numerical value  $\tilde{x} \approx 2.82$ . The peak frequency of the distribution grows linearly with temperature, which is known as Wien's displacement law. Reinserting the peak frequency into the Planck formula one yields

$$B_{\nu_{\max}}(T) = \frac{2k_B^3 \tilde{x}^3}{h^2 c^2} \underbrace{\frac{1}{e^{\tilde{x}} - 1}}_{=const.} T^3 \quad (2.2.0.2)$$

The peak of the specific intensity grows as  $\propto T^3$ . In the Rayleigh-Jeans limit for low frequencies,  $\nu \ll k_B T/h$ :

$$B_\nu(T) \approx 2k_B T \frac{\nu^2}{c^2} \quad (2.2.0.3)$$

The specific intensity increases with the frequency squared in this regime. For this region the brightness temperature is defined: a source has a certain specific intensity at a certain frequency. If the frequency of interest is very small, e.g. in the radio, the Rayleigh-Jeans limit is applicable. Solving the Rayleigh-Jeans limit for the temperature yields the temperature that a black body would need to produce the observed specific intensity,  $T = I_\nu c^2 / (2k_B \nu^2)$ . For a black body the brightness temperature is uniquely defined, due to the monotonicity of the Planck function (e.g. [Rybicki and Lightman 1979](#)).<sup>2</sup>

Another useful result is the integral over the frequencies, the Stefan-Boltzmann law

$$\int_0^\infty B_\nu(T) d\nu = \frac{2\pi^4 k_B^4}{15c^2 h^3} T^4 \quad (2.2.0.4)$$

which is only dependent on the temperature to the fourth power. By reconsidering the flux for a lambertian surface element,  $F_\nu = \pi B_\nu$  and introducing the Stefan-Boltzmann constant  $\sigma_B = 2\pi^5 k_B^4 / (15c^2 h^3)$  the flux crossing a surface element is  $F = \sigma_B T^4$ . The corresponding luminosity of an area  $A$  emitting black body radiation at temperature  $T$  is  $L = A\sigma_B T^4$ .

Summarising, the following scaling relations hold: luminosity  $\propto T^4$ , peak frequency  $\propto T$ , and peak specific intensity (and flux)  $\propto T^3$ .

## 2.3 Basics of Electrodynamics

### 2.3.1 Lorentz Force, Maxwell Equations and Poynting Vector

The basic principle behind the interaction of electric and/or magnetic fields and point charges is the electromagnetic force or Lorentz force, acting onto an electric charge  $q$  moving with velocity  $\vec{v}$  (e.g. [Griffiths 1999](#))

$$\vec{F} = q\vec{E} + q\vec{v} \times \vec{B} \quad (2.3.1.1)$$

where  $\vec{E}$  and  $\vec{B}$  denote the electric field and the magnetic field, respectively. This equation describes how a charged particle reacts when exposed to external fields. The first part is the electric force and the second part the magnetic force.

The nature of light is twofold: light must be described as particles (photons) or as electromagnetic waves, depending on the physical problem under investigation - the so-called

<sup>2</sup>When comparing the spectra of two black bodies of different temperatures, the planck formula of the hotter one exceeds the other for all frequencies.

"wave-particle duality" (Einstein 1905). While a photon is a quantised amount of energy  $h\nu$  with  $h$  being the Planck constant and  $\nu$  the frequency, an electromagnetic wave is treated in the framework of Maxwell's equations. The Maxwell equations are relativistically covariant (e.g. Jackson 1975). Within the purpose of this work, the classical formulation by Heaviside of Maxwell's equations in derivative form is used (e.g. Griffiths 1999). They are:

$$\nabla \vec{E} = \frac{\rho}{\epsilon_0} \quad (2.3.1.2)$$

$$\nabla \vec{B} = 0 \quad (2.3.1.3)$$

$$\nabla \times \vec{E} = - \frac{\partial \vec{B}}{\partial t} \quad (2.3.1.4)$$

$$\nabla \times \vec{B} = \frac{1}{c^2} \frac{\partial \vec{E}}{\partial t} + \mu_0 \vec{J} \quad (2.3.1.5)$$

where  $\nabla$  is the gradient,  $\epsilon_0$  and  $\mu_0$  are the electric and magnetic vacuum permittivities,  $c = 1/(\epsilon_0\mu_0)^{1/2}$  the velocity of light,  $\rho$  denotes the charge density and  $\vec{J} = \rho\vec{v}$  the displacement current.  $\rho$  and  $\vec{J}$  are each zero in the vacuum. From the two latter Maxwell equations the well known wave equation for the vacuum can be derived.

$$\left( \nabla^2 - \frac{1}{c^2} \frac{\partial^2}{\partial t^2} \right) \vec{E} = 0 \quad (2.3.1.6)$$

$$\left( \nabla^2 - \frac{1}{c^2} \frac{\partial^2}{\partial t^2} \right) \vec{B} = 0 \quad (2.3.1.7)$$

The Maxwell equations together with the Lorentz force provide the description for a variety of electromagnetic phenomena and radiative processes, as shown below.

A useful quantity derived from conservation of energy, Lorentz force and Maxwell equations is the Poynting vector (e.g. Jackson 1975)

$$\vec{S} = \frac{1}{\mu_0} (\vec{E} \times \vec{B}) \quad (2.3.1.8)$$

which can be identified with the energy content that a wave is carrying, or the flux through an area with orientation  $\vec{n}$ , hence  $F = \vec{n} \cdot \vec{S}$  (see subsection 2.1.1).

While the Lorentz force incorporates the effect of an external field on a particle, one should also explain how particles emit radiation. The former can be understood easily, but the latter requires more insight about electrodynamics, namely the Larmor formula as a basic description. Therefore the derivation of this formula is illustrated below, to understand the radiation processes connected to accelerated charged particles. First, one should distinguish between different mechanisms emitting radiation: when charged particles experience acceleration by other charged particles the electric force (Coulomb interaction) takes place. The radiation then is called Bremsstrahlung, due to the historical discovery of energetic radiation in rapidly decelerating charged and quickly moving particles inside materials. When a charged particle moves along a trajectory forming an angle with the magnetic field lines, the acceleration due to the magnetic force leads to cyclotron emission (for relativistic particles synchrotron emission), similar to the radiation losses found in circular particle accelerators. In the wave picture of light, an electromagnetic wave induces acceleration of a charged particle. The oscillating electric field drives the oscillation of the particle of the same frequency.<sup>3</sup> The accelerated particle radiates with the same frequency as the incident wave (principle of Thomson scattering). Within the particle picture, elastic

<sup>3</sup>The magnetic acceleration is negligible for low velocities.

photon scattering takes place. While the processes above can be fully understood within the wave-picture there exists another mechanism, the Compton effect. Therefore, one requires to change into the particle picture of light. Briefly, the collision of photons with particles and the classically invoked conservation of energy, conservation of momentum and the relativistic energy momentum relation lead to a change of the photon energy, hence of the frequency. This is not explainable in the wave picture. However, to describe the inverse Compton effect it will turn out, that the process can be approximated by elastic photon scattering in the frame of the electron by the application of special relativity.

### 2.3.2 Relativistic Larmor Formula

The derivation of the Larmor formula completely takes place in the wave picture of light. The electric and magnetic field of a relativistically moving point charge can be obtained within the theory of retarded potentials (Liénard-Wiechert potentials, e.g. [Rybicki and Lightman 1979](#)) where they take the form

$$\vec{E}(\vec{x}, t) = \frac{q}{4\pi\epsilon_0} \left\{ \frac{\vec{n} - \vec{\beta}}{\gamma^2(1 - \vec{\beta}\vec{n})^3 R^2} + \frac{\vec{n} \times [(\vec{n} - \vec{\beta}) \times \dot{\vec{\beta}}]}{c(1 - \vec{\beta}\vec{n})^3 R} \right\}_{t_{ret}} \quad (2.3.2.1)$$

$$\vec{B}(\vec{x}, t) = \frac{1}{c} (\vec{n} \times \vec{E}) \quad (2.3.2.2)$$

Here is  $\vec{\beta} = \vec{v}/c$  and the Lorentz factor  $\gamma = 1/(1 - |\vec{\beta}|^2)^{1/2}$ .  $\vec{\beta}$  and  $\dot{\vec{\beta}}$  are the particle's scaled velocity and acceleration, respectively.  $\vec{n}$  is normalised to unity and pointed towards the observer. The geometry is illustrated in [figure 2.2](#). The quantities inside the bracket are evaluated at the retarded time  $t_{ret}$ : the distance of the point source to the observer at time  $t_{ret}$  is  $R$  and an electromagnetic signal spreads with velocity  $c$ . At time  $t = t_{ret} + R/c$  the observer then measures the fields, since the signal lasted the time interval  $R/c$  to arrive.

The corresponding energy flux, the power per unit area  $dP/dA$  is the magnitude of the Poynting vector ([equation 2.3.1.8](#)). In [equation 2.3.2.1](#) the second part of the bracket, the so-called acceleration term, causes the radiation, as it decays as  $\propto 1/R$ , from what follows  $|\vec{S}| \propto 1/R^2$ . The energy flux is distributed into a sphere whose surface goes like  $\propto R^2$ . Just the acceleration term has a non-vanishing contribution to the energy flux for  $R$  tending towards  $\infty$ .

In the non-relativistic limit ( $\vec{\beta} \ll \vec{n}$ ,  $1 - \vec{n}\vec{\beta} \approx 1$ ) the radiated power per solid angle can be rewritten

$$\frac{dP}{d\Omega} = R^2 \frac{dP}{dA} = R^2 |\vec{S}| = \frac{q^2}{\mu_0(4\pi\epsilon_0)^2 c^2} |\vec{E} \times (\vec{n} \times \vec{E})| = \frac{q^2 a^2}{(4\pi)^2 \epsilon_0 c^3} \sin^2 \theta \quad (2.3.2.3)$$

by evaluating  $\vec{E} \times (\vec{n} \times \vec{E}) = |\dot{\vec{\beta}}|^2 \sin^2 \theta \vec{n}$  where  $\theta$  denotes the angle between  $\vec{n}$  and  $\dot{\vec{\beta}}$ , and rewriting  $\dot{\vec{\beta}}$  in terms of acceleration. Finally, spherical integration leads to the classical Larmor formula

$$P = \frac{2}{3} \frac{q^2 a^2}{4\pi\epsilon_0 c^3} \quad (2.3.2.4)$$

$P$  is the total energy a non-relativistic charged particle radiates when (de)accelerated by an external force. The angular dependency  $\sim \sin^2 \theta$ , shows, that the radiation is emitted mainly perpendicular to the direction of acceleration, equally forward and backward with respect to the velocity.

[Rohrlich \(1964\)](#) shows that the radiated energy is invariant under Lorentz transformation. One needs to transform the power in an appropriate way to yield the relativistic

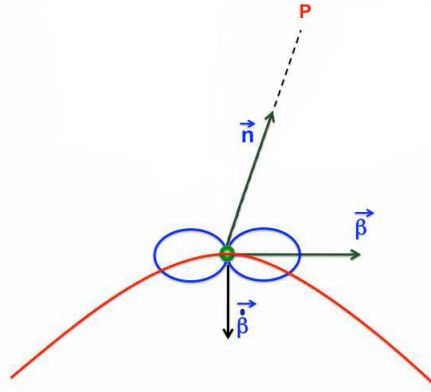


FIGURE 2.2: Sketch of the geometry. A charge is moving with  $\vec{\beta}$  and accelerated with  $\dot{\vec{\beta}}$ . Additionally the emission cones of the charge are indicated in blue for the non-relativistic case ( $\sin^2 \theta^2$  characteristic, see text). Figure from Ghisellini 2013.

expression. The relativistic form of the Larmor formula, also known as Liénard's generalisation reads (Jackson 1975)

$$P = \frac{2}{3} \frac{q^2 \gamma^6}{4\pi\epsilon_0 c} \left[ |\dot{\vec{\beta}}|^2 - (\vec{\beta} \times \dot{\vec{\beta}})^2 \right] = \frac{2}{3} \frac{q^2 \gamma^4}{4\pi\epsilon_0 c^3} \left( \gamma^2 a_{\parallel}^2 + a_{\perp}^2 \right) \quad (2.3.2.5)$$

where the latter expression is just an algebraic reformulation. Starting from this expression we will develop the synchrotron emission.

Since electrons and protons possess the same absolute charge value but protons have a roughly by three orders of magnitude higher inertial mass, the resulting acceleration of a proton by the Lorentz force is much smaller when compared to the acceleration for an electron. Because of that it is sufficient to only consider electrons in the context of radiation.<sup>4</sup>

## 2.4 Synchrotron Emission

### 2.4.1 Emitted Power of a Single Relativistic Electron

An electron moving at a non-relativistic velocity perpendicularly with respect to an external homogeneous magnetic field  $B$  experiences a Lorentz force perpendicular to its movement direction. This leads to a circle-shaped trajectory of the particle, where the radius is the Larmor radius  $r_L$ , resulting from equality of the centripetal and the Lorentz force:

$$r_L = \frac{mv}{qB} \quad (2.4.1.1)$$

where the electron of charge  $q$  and of mass  $m$  moves at velocity  $v \ll c$ . The corresponding gyration frequency is

$$\nu_L = \frac{qB}{2\pi m} \quad (2.4.1.2)$$

where besides the external magnetic field only the ratio  $q/m$  is important, but not the velocity.

<sup>4</sup>From now on the radiating particle is called electron. This implicitly includes also positrons, but is not important for the treatment here.

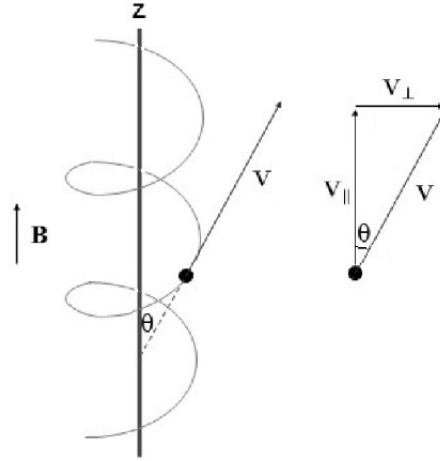


FIGURE 2.3: Helical trajectory of an electron in an external magnetic field. From [Singal \(2016\)](#).

In the relativistic case (see [A.2](#)), the time between moving frame and observer frame at rest "scales" with  $\gamma$ , thus the relativistically corrected gyration frequency for a rest-frame observer is  $\nu_R = \nu_L/\gamma$  (e.g. [Ghisellini 2013](#)).

The starting point for the description of synchrotron emission is the radiative loss of a single particle accelerated in a magnetic field according to the relativistic Larmor formula ([equation 2.3.2.5](#)); [figure 2.3](#) illustrates the geometry. In the case of synchrotron emission the energy losses are assumed to be negligible during a single gyration, hence the Lorentz factor is held constant. For the relativistic case, an acting force changes the relativistic impulse with respect to time by (e.g. [Ghisellini 2013](#))

$$\vec{F} = \frac{d(\gamma m \vec{v})}{dt} = \gamma m \vec{a} \quad (2.4.1.3)$$

A particle moving with  $\vec{v}$  in a homogeneous magnetic field experiences an acceleration due to the Lorentz force, which is perpendicular to the direction of the field and the movement, denoted by  $a_{\perp}$ . Equating the change of the relativistic impulse with the Lorentz force yields

$$\gamma m a_{\perp} = q |\vec{v} \times \vec{B}| = qvB \sin \theta = qv_{\perp} B \quad (2.4.1.4)$$

where the pitch angle  $\theta$  between the velocity and the magnetic field is introduced. Inserting this into the relativistic Larmor formula ([equation 2.3.2.5](#)) one yields the total power a single particle emits while gyrating in a magnetic field

$$P = \frac{2}{3} \frac{q^2 \gamma^4}{4\pi \epsilon_0 c^3} \left( \frac{qv |\vec{B}| \sin \theta}{\gamma m} \right)^2 = \frac{2}{3} \frac{q^4 \gamma^2}{4\pi \epsilon_0 m^2 c^3} v^2 |\vec{B}|^2 \sin^2 \theta \quad (2.4.1.5)$$

By averaging over pitch angles, i.e. by making the simplifying assumption of isotropically distributed velocities, one can replace  $\sin^2 \theta$  with  $2/3$ .

## 2.4.2 Typical and Critical Frequencies

At first a more qualitative approach is illustrated, which captures in fact all important characteristics, following [Ghisellini \(2013\)](#). A full derivation is not the scope of this work but some results are included, where necessary.

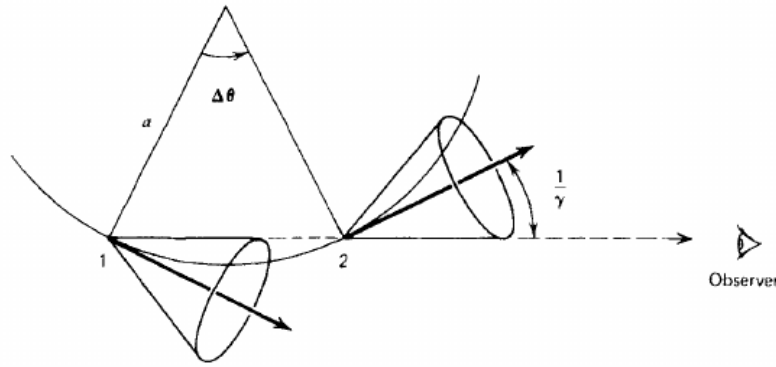


FIGURE 2.4: The emission cone of a gyrating relativistic electron. From Rybicki and Lightman (1979).

In contrast to the classical emission pattern, for a relativistic electron the emission is confined in a cone, due to aberration (see section A.2). The electron emits most of its radiation towards a observer in the time interval while the observer is in the emission cone. Let us focus on the quantities in the observer frame. The ratio of the cone opening angle,  $2/\gamma$ , over a full gyration,  $2\pi$ , times the gyration time,  $1/\nu_R$ , leads to the time the electron is emitting towards the observer, the emission time  $t_E = 1/(\pi\nu_R)$ . Since the electron is (in approximation) moving towards the observer during the emission time interval, the observer's receiving time is shortened  $t_O = (1 - \beta)t_E \approx t_E/(2\gamma^2)$ , which is just the classical Doppler shift since time dilation in  $\nu_R$  is already included. The approximation in the last step is simply obtained by expanding the term  $1 - \beta$  with  $1 + \beta \approx 2$  and inserting the definition of  $\gamma$ .

The emission from a relativistically gyrating electron, measured from the observer, is a strongly peaked time series, where approximately each peak has a width of  $t_O$  and the "spacing" between the peaks is  $1/\nu_R \sim t_E \gg t_O$ . Consequently the power spectrum of the Fourier transformation is expected to have a maximum at frequencies which directly sample the peak-width. In this idealised case the typical frequency, i.e. the frequency where the power spectrum peaks and most energy is radiated to the observer, is the inverse of the time-scale  $\nu_T \approx 1/(2\pi t_O) = \gamma^2 \nu_L = \gamma^3 \nu_R$ .

Now we compare the result of the exact derivation to our approximative case. Considering the transformation of the emission cones and the development of the power spectrum in a more rigorous mathematical fashion, which can be found in e.g. Pacholczyk (1970), the power per frequency emitted by an electron of given pitch angle then is <sup>5</sup>

$$P(\nu) = \frac{\sqrt{3}q^3 B \sin \theta}{8\pi^2 \epsilon_0 m_e c} \left( \frac{\nu}{\nu_c} \right) \int_{\nu/\nu_c}^{\infty} K_{5/3}(\zeta) d\zeta \quad (2.4.2.1)$$

where the critical frequency is defined as  $\nu_c = 3/2\gamma^2 \nu_L \sin \phi$  and  $K_{5/3}$  is a modified Bessel function (see e.g. N. Bronstein and A. Semendjajew 1979). In figure 2.5 the function  $F(x) = x \int_x^{\infty} K_{5/3}(\zeta) d\zeta$  is shown to illustrate its shape and the legitimacy of assuming a peaked single electron emission spectrum. The critical frequency shows the same dependencies as the typical frequency, derived above in the simplified fashion: it depends on the square of the Lorentz factor and linearly on the magnetic field strength,  $\nu_c \propto \gamma^2 B$ , only the pre-factor differs. The similar behaviour of typical frequency and critical frequency emphasises, that

<sup>5</sup>Theoretically the power spectrum is non continuous. In practice, however, e.g. fluctuations of electron or magnetic field energy lead to an effectively continuous spectrum (<http://www.cv.nrao.edu/~sransom/web/Ch5.html>, accessed 2017-06-19).

the simplified treatment closely recovers the results of the mathematically more sophisticated derivation. Indeed, it captures the physical essence in spite of the approximations. We will continue with the result of the simplified treatment.

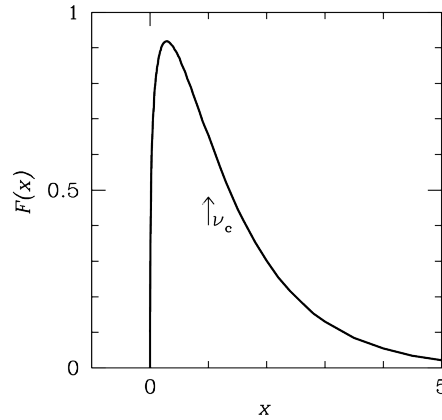


FIGURE 2.5: Spectral shape of the single electron synchrotron spectrum. The function shown is  $F(x) = x \int_x^\infty K_{5/3}(\zeta) d\zeta$ . The peakedness of the function shall justify the approximation, that the entire power is radiated at a certain frequency. From <http://www.cv.nrao.edu/~sransom/web/Ch5.html>, accessed 2017-06-19.

### 2.4.3 Electrons with a Power Law Energy Distribution

So far we derived the power emitted of a single electron and the (typical) frequency, at which the power is expected to be preferentially observed. Now the aim is to calculate the resulting spectrum of an ensemble of many electrons, distributed energetically according to a power law. A power law distribution of electrons represents the simplest and an idealised case. However, electrons in jets, i.e. accelerated or shocked electrons, typically show a power law distribution. The concept introduced can be applied to arbitrary distributions, e.g. for electrons in a thermal (Maxwellian) distribution.<sup>6</sup>

The emissivity of multiple electrons distributed energetically is the summed contribution of each individual electron. On the way to the composite spectrum furthermore the following simplification is relevant: A sum of peaked functions is not sensitive on the intrinsic shape of the functions, if accumulating the individual functions in a range much broader than the single functions themselves (Jones 1968). As there are electrons with a wide range of energies the importance of the wings of the individual spectra recedes. This means, that assuming simply that all energy of a single electron is emitted at its typical frequency leads to quantitatively quite correct results (Ghisellini 2013). In the following, this simplification is applied and for the emitted power equation 2.4.1.5 used. Additionally is used that the pitch angles are isotropically distributed, independently on the electron energy.

Consider an ensemble of electrons distributed according to  $n(E) \propto E^{-p}$ , where  $n(E)$  is the electron density in dependence on the energy and  $p$  a positive number, fixing the slope of the distribution. Energy, Lorentz factor and typical frequency are linked by  $E = \gamma mc^2 \approx \sqrt{\nu_T/\nu_L} mc^2$ . The density can be expressed equivalently in terms of the Lorentz factor,

$$n(\gamma) \propto \gamma^{-p} \quad (2.4.3.1)$$

<sup>6</sup>Thermal electron distributions produce (non-thermal) synchrotron emission. That should not be confused with thermal electron distributions producing (thermal) free-free or black body emission.

When integrating that just the normalisation constant differs. Our aim is to derive the spectral dependencies, so all other constants are left out, too. From now on the index of the typical frequency is skipped: Above it is used to denote the frequency emitted by electrons of certain  $\gamma$ . In what follows the spectral dependency on the frequency is of interest, thus frequency is a variable,  $\nu = \nu_T$ .

The emissivity within a frequency interval  $d\nu$  is proportional to the the integral of the convolution of electron density and specific power  $P(\gamma)$ . In general the integration must be carried out over all energies (Lorentz factors),

$$\int_{\nu_1}^{\nu_2} j(\nu) d\nu \propto \int_{\gamma_1}^{\gamma_2} n(\gamma) P(\gamma) d\gamma \quad (2.4.3.2)$$

but in this approximative case only the electrons with the "right" energy contribute to the emission at a certain frequency: The contribution from electrons of different energies is neglected. This way we can consider the integrands only. By recalling the defining relations ( $\nu_L \propto B$ )

$$n \propto \gamma^{-p}; P(\gamma) \propto \gamma^2 B^2; \gamma^2 \propto \frac{\nu}{B} \quad (2.4.3.3)$$

we obtain

$$\begin{aligned} j(\nu) &\propto n(\gamma) P(\gamma) \frac{d\gamma}{d\nu} \\ &\propto (\gamma^{-p}) (\gamma^2 B^2) (\nu^{-1/2} B^{-1/2}) \\ &\propto \left(\frac{\nu}{B}\right)^{-p/2} (\nu B) (\nu^{-1/2} B^{-1/2}) \\ &\propto \nu^{\frac{1-p}{2}} B^{\frac{1+p}{2}} \end{aligned} \quad (2.4.3.4)$$

In spite of the approximations, these are the same dependencies as in the full derivation ([Ghisellini 2013](#)).

For a different electron distribution, e.g. a (relativistic) Maxwellian distribution,  $n(\gamma)$  must be exchanged appropriately. The spectral shape will in that case resemble to an extend the underlying thermal electron distribution. However, it is still non-thermal radiation.

#### 2.4.4 Thin Emission and Self Absorption

If the frequency under consideration is sufficiently high, there are only few electrons emitting or absorbing since their population is small. This guarantees for photons to have a mean free path length large enough, ensuring that almost all photons produced in the source escape. In this case, the source is optically thin and the specific intensity at the surface is the emissivity integrated along the path of the ray through the source. For constant emissivity, i.e. homogeneous electron distribution and magnetic field, the intensity is directly proportional  $I_{\text{thin}}(\nu) \propto j(\nu)$ . The flux, is proportional to the intensity and the angular size of the source (compare [subsection 2.1.1](#)), effectively leading to

$$F_{\text{thin}}(\nu) \propto \nu^{\frac{1-p}{2}} B^{\frac{1+p}{2}} \quad (2.4.4.1)$$

A important result to underline from [equation 2.4.4.1](#) is the tight connection between the slope  $p$  of the power law distribution and the spectral slope  $\alpha$  of the optically thin synchrotron emission

$$\alpha = \frac{p-1}{2} \quad (2.4.4.2)$$

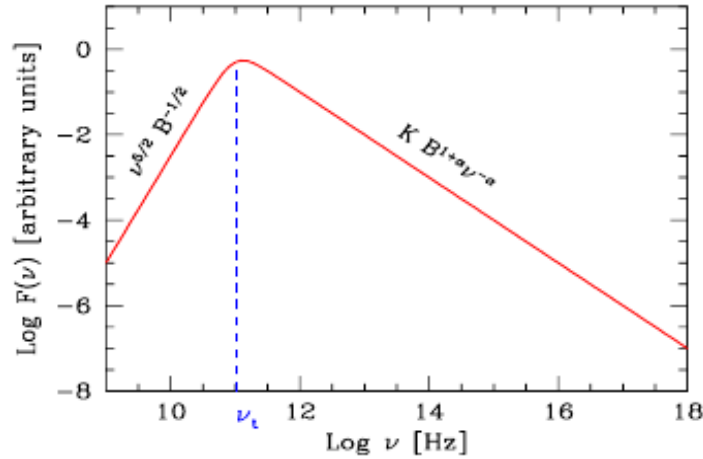


FIGURE 2.6: Shape of the synchrotron spectrum.  $\nu_t$  is the self absorption frequency where  $\tau = 1$ . From Ghisellini (2013).

Now the optically thick region is explored. When the optical thickness  $\tau$  of the source exceeds unity, reprocessing (in terms) of photons becomes a dominant mechanism and the source so-called self absorbed. This expression points out, that electrons capable of emitting at a certain frequency preferentially absorb at that frequency as well (Ghisellini 2013). This was already stated in section 2.1 for thermal sources, but is mentioned again, on the basis of its importance. The difference to thermal emission is, that in the present case no LTE can exist - there is no well defined overall temperature. However, one can assign a pseudo temperature to each electron, which is related to its (kinetic) energy and hence, absorbable and emitable frequency.<sup>7</sup>

$$3k_b T \approx \gamma m c^2 \propto \sqrt{\frac{\nu}{B}} \quad (2.4.4.3)$$

Although, this is strictly speaking not a physical temperature, this can be done since within this derivation the electron energy (pseudo temperature) is directly linked to the frequency. That means radiative interaction only takes place between electrons of the same "temperature". This way the medium can establish local radiative equilibrium at certain isolated temperatures, regardless of the actual shape of the energy distribution.

If choosing a particular frequency  $\nu$ , where the source is optically thick, we have radiative equilibrium. It holds  $dI_\nu/ds = 0$  for an arbitrary path  $ds$ . By the same argumentation like in subsection 2.1.2 the source is a perfect absorber at this frequency. It emits perfectly, and consequently its maximum specific intensity is given by the Rayleigh-Jeans law<sup>8</sup> (equation 2.2.0.3), where the temperature is replaced by frequency and magnetic field of the electrons (equation 2.4.4.3).

$$F_{\text{thick}}(\nu) \propto I_{\text{thick}}(\nu) \approx B_\nu \approx \frac{2\nu^2 k_B T}{c^2} \propto B^{-1/2} \nu^{5/2} \quad (2.4.4.4)$$

Here  $B_\nu$  denotes the specific intensity of a black body (not to confuse with the magnetic field  $B$  without subscript). Towards lower frequencies the electrons "visible" for the radiation field become progressively colder. This leads to the remarkable slope of 5/2, which is

<sup>7</sup>We are dealing with highly relativistic electrons here.

<sup>8</sup> $h\nu \ll k_B T$ .

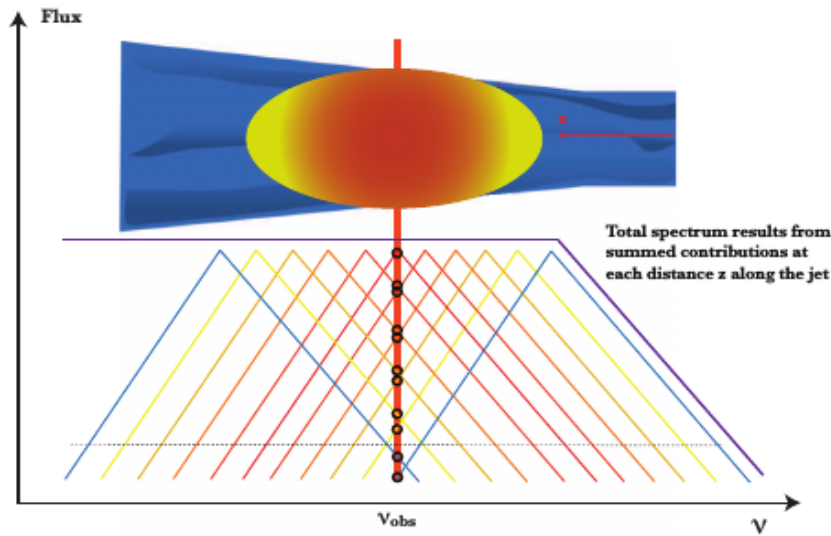


FIGURE 2.7: Superposition of synchrotron components producing a flat spectrum. The upper schematic graphic shows the jet (blue) with the emission patch observed at a certain frequency. Below it is illustrated how qualitatively the superposition of laterally cooling synchrotron components may result in a flat spectrum. The part of the jet whose turnover frequency corresponds to the observed one contributes most. Neighbouring ("hotter" and "colder") components contribute decreasingly, resulting in an elongated patch. From [Markoff \(2010\)](#).

the maximal slope of a homogeneous source (e.g. [Kellermann and Pauliny-Toth 1969](#)).

### 2.4.5 Superposition of Synchrotron Components in a Jet

Electrons distributed energetically according to a power law in a homogeneous magnetic field emit the characteristic synchrotron spectrum derived in [subsection 2.4.4](#). The spectrum of a jet can be treated as a superposition of multiple synchrotron components. While the jet expands adiabatically, electron and magnetic field densities decrease.<sup>9</sup> The synchrotron emission becomes less energetic, the self absorption frequency decreases. As illustrated in [figure 2.7](#), the superposition of these multiple self absorbed synchrotron components may result in a flat spectrum. One can show, that optically thick emission of a conically expanding and adiabatically cooling jet gives rise to a flat composite spectrum, if the electron number is conserved and the equipartition factor<sup>10</sup> remains constant ([de Bruyn 1976](#)).

### 2.4.6 Energetic Argument Towards Equipartition

Equipartition in the context of synchrotron sources names the state of having the same amount of electron energy and energy contained in the magnetic field. There exists a natural argument for rough equipartition in a synchrotron source. This does not mean that sources generally obey equipartition, but motivates, why assumptions of rough equipartition are energetically meaningful.

In the fashion of a very illustrative approach (c. f. [Ghisellini 2013](#)), the luminosity of a homogeneous synchrotron source is the number of electrons  $N$  times the averaged power emitted by each electron,  $L \propto N \langle \gamma^2 \rangle B^2$ . The internal energy of all particles, radiating electrons and protons, is  $U_{\text{int}} = U_e + U_p = U_e(1 + l)$ , where  $U_e \propto N \langle \gamma \rangle$ . The constant

<sup>9</sup>We continue neglecting radiative losses in the simplified approach.

<sup>10</sup>The ratio between magnetic and electron energy density, see below.

$l$  is the ratio between proton and electron energy. It is not further specified, since it is unknown how energy is distributed between them. The magnetic field density scales as  $U_B \propto B^2$ . Inserting both into the expression for the luminosity one yields

$$L \propto U_B U_{\text{int}} \frac{\langle \gamma^2 \rangle}{\langle \gamma \rangle} \quad (2.4.6.1)$$

The fraction only depends on the energy distribution of the particles. A certain luminosity can be achieved by different combinations of magnetic field and electron energy, but the minimum of total energy  $U_{\text{tot}} = U_B + U_{\text{int}}$  occurs for  $U_B \approx U_{\text{int}}$ . A source in equipartition has the maximum efficiency in converting particle and magnetic field energies into non-thermal radiation. To characterise a source away from equipartition, commonly  $U_B = kU_e$  is introduced, where  $k$  is called equipartition parameter.

## 2.5 Inverse Compton Effect

The direct Compton effect is inelastic scattering of photons by electrons. Direct Compton scattering transfers energy from the photon to the electron. The inverse Compton effect appears when photons are scattered by relativistic electrons. The scattering process, even for the elastic case in the rest frame of a relativistic electron, can increase the photon's energy. This process energises photons in a relativistically hot medium. It is likely to be the dominant production mechanism of (hard) X-ray emission associated with black holes.

The inverse Compton effect will be treated by only considering elastic Thomson scattering of photons in the electron rest frame, which is valid when the photon energy is much smaller than the electron rest energy;<sup>11</sup> the momentum transfer from the photon is neglected. For high energy photons one must consider the Compton effect and the Klein-Nishina high energy corrections for the Thomson cross section (see e.g. [Heitler 1954](#)). However these effects decrease the energy of the scattered photons and the probability of scattering by reducing the cross section for high energy photons ([Rybicki and Lightman 1979](#)). Hence the following idealised treatment deals strictly with Thomson scattering in the electron frame,  $h\nu' \ll mc^2$ .

### 2.5.1 Thomson Cross Section

Consider a charged particle, initially at rest, exposed to continuous electromagnetic radiation ([Jackson 1975](#)). Solving the wave equation 2.3.1.7 and considering for now only linear polarised light, one finds a stationary time dependent electric field  $\vec{E} = \vec{E}_0 \cos(\omega t)$  at the position the particle. The Lorentz force acting on the particle induces an acceleration. Requiring the amplitude of the wave to be sufficiently small, the resulting velocity of the oscillating particle will also be small compared to  $c$ . Then one can neglect the magnetic part of the Lorentz force and use the classic Larmor formula equation 2.3.2.3.<sup>12</sup> Inserting the quadratic time-averaged acceleration,  $a^2 = (qE_0/m)^2/2$  one gets:

$$\frac{dP}{d\Omega} = \frac{q^2 a^2}{(4\pi)^2 \epsilon_0 c^3} \sin^2 \theta = \frac{q^4 E_0^2}{2(4\pi)^2 \epsilon_0 m^2 c^3} \sin^2 \theta \quad (2.5.1.1)$$

<sup>11</sup>In the case of low energy seed photons, typical for a radiation field for example produced by synchrotron emission, this assumption is valid.

<sup>12</sup>From the magnetic field expression (lower equation in equation 2.3.2.2) one can conclude that the Lorentz force is dominated by the electric force component, as long as the velocity is small compared to the speed of light.

This is the differential re-emitted energy of the particle. The cross section  $\sigma$  can be defined as the ratio of re-emitted energy  $P$  over the incident energy of the radiation  $S$ . The latter is the time-averaged Poynting flux of a plane wave,  $S = \epsilon_0 c E_0^2 / 2$  (see [equation 2.3.1.8](#) and [2.3.2.2](#)). This can be used to calculate the differential cross section:

$$\frac{d\sigma}{d\Omega} = \frac{dP}{S d\Omega} = \frac{q^4}{(4\pi)^2 \epsilon_0^2 m^2 c^4} \sin^2 \theta \quad (2.5.1.2)$$

where  $\theta$  is the angle between the oscillation axis and the considered direction. To make the geometry clearer: the incident wave comes e.g. along the x-axis and is polarised in the z-direction. The oscillation of the electron takes place along the z-axis, and with the same frequency as the incident wave. The direction of considered emission is  $\vec{n}$ , hence it holds  $\cos \theta = \hat{e}_z \vec{n}$  with  $\hat{e}_z$  being the unit vector in z-direction. The  $\sim \sin^2 \theta$  factor forms a toroidal shaped emission pattern with azimuthal symmetry. Integrating the angular dependence yields the Thomson cross section for an electron ( $q = e, m = m_e$ )

$$\sigma = \frac{e^4}{6\pi \epsilon_0^2 m_e^2 c^4} \quad (2.5.1.3)$$

This is the total cross section for elastic scattering off electrons, independent of the polarisation of the incident wave.

For the case of a non-polarised incident wave the cross section can be represented by the average of both orthogonal polarisation directions, y- and z-direction. Then the total cross section is the average of the cross section of each polarisation ([Ghisellini 2013](#)). The superposition of the two orthogonal tori results in a peanut shaped angular dependence of the scattered radiation pattern. An important implication of this geometry is a forward-backward symmetry of the scattering direction and intensified scattering probability aligned along the x-axis, the incident direction.

## 2.5.2 Electron Energy Loss

This section is mainly based on [Rybicki and Lightman \(1979\)](#) and [Ghisellini \(2013\)](#). To derive the energy a photon gains in a single scattering process, consider a photon of energy  $\epsilon$  in the observer frame. This photon scatters off a relativistically moving electron. The corresponding geometry is shown in [figure 2.8](#). Since energy and frequency are directly connected the energy of the photon in the electron frame,  $K'$  is transformed according to the relativistic Doppler shift ([equation A.2.2.1](#))

$$\epsilon' = \epsilon \gamma (1 - \beta \cos \theta) \quad (2.5.2.1)$$

In the Thomson regime the photon's energy remains the same in the electron frame during the scattering process  $\epsilon'_1 = \epsilon'$ . Transforming back to  $K$  holds:

$$\epsilon_1 = \epsilon'_1 \gamma (1 + \beta \cos \theta'_1) \quad (2.5.2.2)$$

Putting these equations together with the transformation of angles, (cf. inverse of the [equation A.2.3.3](#))

$$\cos \theta'_1 = \frac{\cos \theta_1 - \beta}{1 - \beta \cos \theta_1} \quad (2.5.2.3)$$

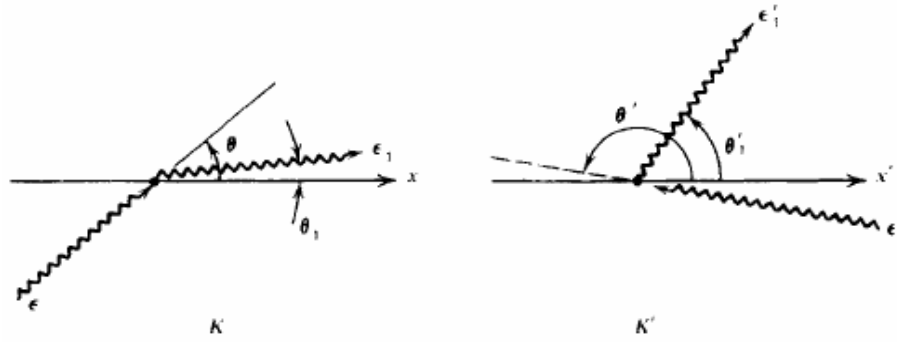


FIGURE 2.8: The geometry of the scattering process in the observer frame and rest frame of the electron. From Rybicki and Lightman (1979).

one can derive the energy in the observer frame of the photon after the scattering, related to quantities in the observer frame only:

$$\epsilon_1 = \epsilon \frac{1 - \beta \cos \theta}{1 - \beta \cos \theta_1} \quad (2.5.2.4)$$

This equation relates the initial photon energy  $\epsilon$  with the energy after the scattering  $\epsilon_1$ . Photons can gain or lose energy, depending on the detailed scattering geometry.

If all incident photons have energy  $\epsilon$ , and come from one direction  $\theta$ , then the number of scattering events per unit time in the observer frame is  $dN_\epsilon/dt = n(\epsilon)\sigma(c - v \cos \theta)$ . The photon density is  $n(\epsilon)$  and in the bracket is the relative velocity between electron and incident photons.<sup>13</sup> The outgoing power of the scattered photons of initial energy  $\epsilon$  can be calculated via  $dE_\epsilon/dt = \epsilon_1 dN_\epsilon/dt$ .

In order to consider the outgoing power for one directional incident photons with a certain energy distribution, one must integrate over incoming photon energies. By expressing  $\epsilon_1$  in terms of  $\epsilon$  results:

$$\frac{dE}{dt} = \sigma c \int \frac{(1 - \beta \cos \theta)^2}{1 - \beta \cos \theta_1} n(\epsilon) \epsilon d\epsilon \quad (2.5.2.5)$$

In the electron frame the emission pattern of the Thomson scattering is symmetric in both, forward and backward directions (see subsection 2.5.1): When averaging over the scattering of multiple photons there is no preferred forward or backward scattering. The average scattering angle is  $\pi/2$  or  $\langle \cos \theta'_1 \rangle = 0$  implying  $\langle \cos \theta_1 \rangle = \beta$  (Rybicki and Lightman 1979, see equation A.2.3). It follows

$$\frac{dE}{dt} = \sigma \gamma^2 c \int (1 - \beta \cos \theta)^2 n(\epsilon) \epsilon d\epsilon \quad (2.5.2.6)$$

which is the power of scattered photons, incident from a certain direction  $\theta$ , and inversely Compton scattered off a electron with Lorentz factor  $\gamma$ .

Now we consider an isotropic distribution for the incident direction of the scattered photons. By averaging over  $\theta$  one yields  $(1 - \beta \cos \theta)^2 = 1 + \beta^2/3$ . The initial photon energy density is  $U_{\text{ph}} = \int n(\epsilon) \epsilon d\epsilon$ . Its average decrease rate is  $-dN_\epsilon/dt = -\sigma c U_{\text{ph}}$ , because scattered photons are not counted. Balancing the scattered power ( $dE/dt$ ) and the incident

<sup>13</sup> Thomson cross section times relative velocity gives volume per time, similar to the derivation of the number of weak encounter in the section about free-free emission (subsection A.3.2).

power  $\sigma c U_{\text{ph}}$  for a single electron leads to its average electron loss power

$$P_c = \frac{dE}{dt} = \sigma c U_{\text{ph}} = \sigma c U_{\text{ph}} \left[ \gamma^2 \left( 1 + \frac{\beta^2}{3} \right) - 1 \right] = \frac{4}{3} c \sigma \gamma^2 \beta^2 U_{\text{ph}} \quad (2.5.2.7)$$

Interestingly the electron loss power scales quadratically with the electron energy but linearly with the total energy of the surrounding radiation field.

### 2.5.3 Compton Spectrum

Rybicki and Lightman (1979) show, how to obtain the spectrum for scattering mono-energetic photons off electrons with a given energy. They assume isotropic distributions for incident photons, electrons, and scattered photons in the observer frame. They further assume that the Thomson scattering in the electron frame is isotropic. Even though these approximations describe an idealised case, they will serve us to understand the important concepts. The average energy of a photon after single scattering in the observer frame is then

$$\langle \epsilon_1 \rangle = \frac{4}{3} \gamma^2 \epsilon \quad (2.5.3.1)$$

For an incident photon energy  $\epsilon$  and electron Lorentz factor  $\gamma$ . In order to obtain the composite spectrum of energetically distributed electrons one must go through a number of steps: At first only incoming photons with energy  $\epsilon$  are considered. The electrons are assumed to be distributed according to a power law  $n_e(\gamma) = K \gamma^{-p}$ , as before for synchrotron emission (see subsection 2.4.3). It is assumed that only the electrons with Lorentz factor  $\gamma = \sqrt{3\epsilon_1/(4\epsilon)} = \sqrt{3\nu_1/(4\nu)}$  are scattering up seed photons of scattered frequency  $\nu_1$ . Each scattering electron emits the power  $P_c(\gamma)$ . So far this is similar to the concept adopted for synchrotron emission.

The spectral emissivity in the frequency interval  $[\nu_1, \nu_1 + d\nu_1]$  for incident photons of frequency  $\nu_0$  and an ensemble of electrons distributed according to  $n_e(\gamma)$  is then  $\epsilon(\gamma, \nu_1) d\nu_1 = 1/(4\pi) P_c(\gamma) n_e(\gamma) d\gamma$  (see equation 2.1.2.1). We further approximate  $\beta \approx 1$ . In the case of single frequency incident photons, the scattered frequency depends only on the electron energy and it is sufficient to consider only the integrands. Combining this (and inserting  $d\gamma/d\nu_1 = 1/2\sqrt{3/(4\nu\nu_1)}$ ) we arrive at

$$\begin{aligned} \epsilon(\gamma, \nu_1) &\approx \frac{K}{4\pi} \frac{4}{3} c \sigma \gamma^{2-p} U_{\text{ph}} \frac{d\gamma}{d\nu_1} \\ &\approx \frac{K}{4\pi} \frac{4}{3} c \sigma \left( \frac{3\nu_1}{4\nu} \right)^{(2-p)/2} U_{\text{ph}} \frac{1}{2} \left( \frac{3}{4\nu\nu_1} \right)^{1/2} \\ &\approx \frac{K c \sigma}{8\pi} \left( \frac{3}{4} \right)^{(1-p)/2} \frac{U_{\text{ph}}}{\nu} \left( \frac{\nu_1}{\nu} \right)^{(1-p)/2} \end{aligned} \quad (2.5.3.2)$$

For monochromatic seed photons of frequency  $\nu$ , the resulting spectrum is a power law with the same relation between electron power law index  $p$  and spectral slope,  $\alpha = (1 - p)/2$ ,  $\epsilon(\nu_1) \propto \nu^{(1-p)/2}$  as for synchrotron emission.

Now, we consider the case of seed photons with distributed energies. The difference to the case above is that the typical photon energy is not only a function of the electron energy but it also depends on the seed photon energy. A certain energy for the scattered photons can be achieved by different electron energies and incident photon energies, as long as equation 2.5.3.1 is fulfilled. Hence one must integrate equation 2.5.3.2 over the range of

seed photon frequencies which contribute to the frequency  $\nu_1$

$$\epsilon(\nu_1) \approx \frac{Kc\sigma}{8\pi} \left( \frac{3}{4}\nu_1 \right)^{(1-p)/2} \int_{\nu_{\min}}^{\nu_{\max}} U_{\text{ph}} \nu^{(p-3)/2} d\nu \quad (2.5.3.3)$$

This relates the emissivity with the properties of the seed radiation field and those of the electron distribution.

The correct choice of integration limits is explained as follows. We assume that the seed radiation field extends from frequencies  $\nu_a$  up to  $\nu_b$ , and the electron energies range from  $\gamma_a$  up to  $\gamma_b$ . We consider the low energy cut-off of the electrons  $\gamma_a$ . Only photons which have initial frequency  $\tilde{\nu} \geq 3\nu_1/(4\gamma_a^2)$  can be upscattered to the frequency  $\nu_1$  or higher. The lower limit of integration is therefore  $\nu_{\min} = \max(\tilde{\nu}, \nu_a)$ . The same argument holds for the high energy cutoff of the electrons  $\gamma_b$ , corresponding to an upper frequency  $\nu^* \leq 3\nu_1/(4\gamma_b^2)$ . The upper limit of integration is  $\nu_{\max} = \min(\nu^*, \nu_b)$ . Since  $\tilde{\nu}$  and  $\nu^*$  depend on  $\nu_1$ , the resulting value of the integral depends on  $\nu_1$ . Only in the region where the integration limits are  $\nu_a$  up to  $\nu_b$ , the integral value is constant. In that case the emissivity is a clean power law.

If the seed radiation field is produced by synchrotron emission of the same distribution of electrons, the mechanism is called synchrotron self Comptonisation (SSC). Its functional dependence on the frequency is  $U_{\text{ph}} \propto \nu^{(1-p)/2}$  in the optically thin regime for a power law distribution of electrons (see [section 2.4](#)). Hence, in the range of constant integration limits the value of the integral is independent on  $\nu_1$ , and the Comptonisation spectrum has the same slope as the seed synchrotron spectrum.

Regarding the (relativistic) Maxwellian distribution of the electrons, the change in the synchrotron spectrum is achieved by folding the Maxwell distribution with the single electron loss (see [section 2.4](#)). If the seed radiation field is emitted from thermal electrons radiating synchrotron, and scattered by the same electrons, we obtain thermal SSC radiation. Specifically, in [equation 2.5.3.3](#) enter the Maxwellian electron distribution expressed in terms of  $n(\gamma)$ , and the synchrotron radiation field  $U_{\text{ph}}$ . The spectrum of the incident radiation is expected to have a minor impact on the resulting Compton spectrum, since it is fairly peaked. This, by parallelism to the monochromatic seed radiation field, results in a Compton spectrum which is mainly determined by the underlying electron distribution. Therefore, for this special case of thermal SSC, both, synchrotron and Compton spectra will tightly resemble the underlying electron distribution in their shape.

## 2.5.4 Compton and Synchrotron - Similarities

[Jones \(1968\)](#) solved the problem of scattering for an isotropic photon field from an isotropic electron distribution, including the Klein-Nishina cross section. They compared their analytic result with the simplified case, which is used here. Specifically assuming that all energy is emitted at the same frequency is a very strong simplification. They state, that it can be shown that for power law distributions of electrons the approximation is applicable for synchrotron and Compton emission. This justifies the approximate derivation and the concepts for the use here.

Since the form of the equations describing the radiated power for synchrotron and inverse Compton is quite similar, they can be compared. Using the pitch angle averaged synchrotron power of a relativistic electron [equation 2.4.1.5](#), substituting the Thomson cross section, and introducing the magnetic field density  $U_B = B^2/(2\mu_0)$ , the synchrotron power can be rewritten as:

$$P_s = \frac{4}{3}c\sigma\gamma^2\beta^2U_B \quad (2.5.4.1)$$

Hence the fraction of synchrotron to Compton losses of an electron is directly linked to magnetic and radiation field energy density, respectively

$$\frac{P_s}{P_c} = \frac{U_B}{U_{ph}} \quad (2.5.4.2)$$

This holds generally, when Thomson scattering in the electron rest frame is valid ([Rybicki and Lightman 1979](#)).

## Chapter 3

# The Model

After the introduction given in [chapter 2](#), focused on the non-thermal radiative processes in AGNs, here the model is described, consisting of a jet and a truncated accretion disc. In particular, it is relevant to understand the different radiative processes involved in the generation of the continuum emission. This will allow us to control the model spectrum for different configurations and provide a physical interpretation of the modelled data.

In [section 3.1](#) the model is briefly introduced and thereafter characterised in detail by explaining each component individually. In [section 3.2](#) the relevant physical parameters in the model are described.

### 3.1 Description

The semi-analytical model `agnjet` focuses on the spectral prediction of mildly relativistic jets ([Markoff et al. 2005](#)). It is developed on the basis of the initial work of [Blandford and Königl 1979](#) and [Falcke 1996](#). The model is able to describe the characteristic flat-to-inverted continuum spectral distribution, i.e. flat in the radio and steeply decreasing at higher frequencies by a superposition of self-absorbed jet components ([Markoff et al. 2005](#); [Markoff 2010](#), see [section 2.4](#), [figure 2.7](#)).

The version of the model `agnjet` used in this thesis contains minor modifications with regard to the version applied to the case of M87 in [Prieto et al. 2016](#). Similar or slightly modified versions have already been applied to BHs (e.g. [Markoff et al. 2005](#); and see others in [van Oers et al. 2017](#)), and to other LLAGNs, such as M87, M81, NGC4051, M94, and Sgr A\* (e.g. [Prieto et al. 2016](#); [Markoff et al. 2008](#); [van Oers et al. 2017](#); [Markoff et al. 2001](#)). Descriptions can be found in e.g. [Maitra et al. \(2009\)](#); [Markoff et al. \(2008\)](#); [Prieto et al. \(2016\)](#); a detailed description can be found in [Markoff et al. 2005](#), chapter 2; Appendix. A scheme illustrating the geometry of the innermost region of the model is given in [figure 3.1](#).

Hot particles are injected into the nozzle, where thermal electrons<sup>1</sup> produce synchrotron emission. The synchrotron photons act as seed photons and interact with the electrons, producing inverse Compton emission, so-called synchrotron self Comptonisation (SSC). The plasma starts expanding beyond the nozzle: laterally, i.e. radially, it expands with constant sound speed; longitudinally it is accelerating weakly by pressure gradients and eventually approaching mildly relativistic bulk velocities. Beyond the shock a fixed particle fraction is accelerated into a power law, which is maintained along the jet. Additionally the model includes a thin truncated accretion disc.

The model is developed in the framework of five basic assumptions, which can be found in a similar form in [Markoff et al. 2005](#):

1. The jet power scales with the accretion rate.

---

<sup>1</sup>The model does not differentiate between positrons or electrons. In the following the terms leptons, electrons and radiating particles are used equivalently.

2. The jet expands freely and accelerates weakly via the pressure gradient.
3. The Protons carry most of the kinetic energy and leptons do most of the radiating.
4. The particles are eventually accelerated into a power law energy distribution.
5. This power law is maintained along the jet.

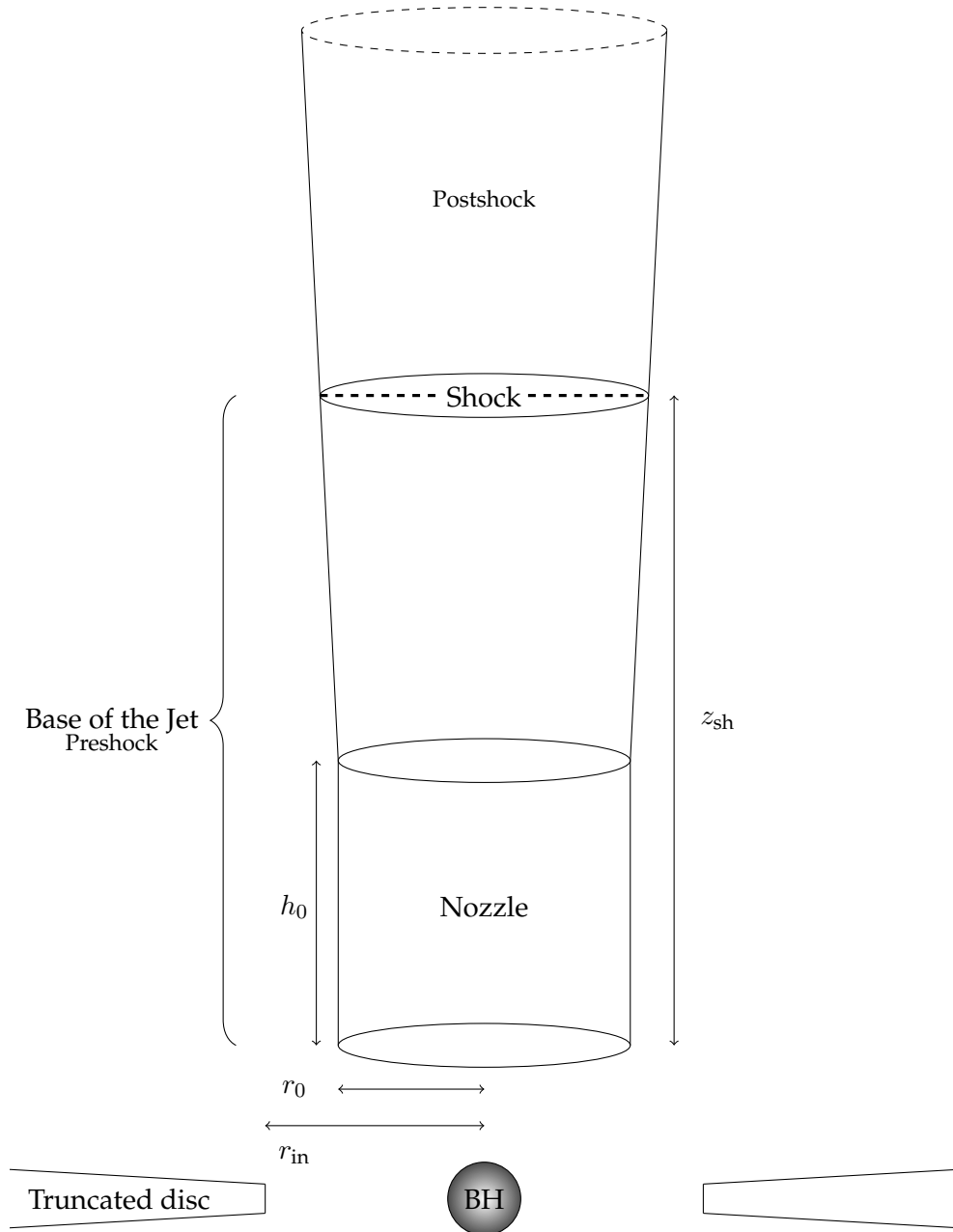


FIGURE 3.1: Geometry of the model. Only upper nozzle and jet are shown. Approaching matter in the accretion disc at  $r_{in}$  is advected into the nozzle, via a radiatively inefficient accretion flow (not modelled). The cylindrical nozzle of radius  $r_0$  and height  $h_{rat} = h_0/r_0$  contains relativistic thermal plasma of temperature  $T_e$ . The plasma starts expanding beyond the nozzle. At the shock distance  $z_{sh}$  distributed acceleration begins, which accelerates a fraction of the particles to a power law energy distribution. Laterally the plasma is expands with constant speed of sound adiabatically. The black hole (black shaded circle) is shown for clarity only. Graphic created with TikZ.

As indicated in [figure 3.1](#) the entire structure defining the jet can be subdivided into three parts: the nozzle, where densities are highest and no bulk acceleration occurs; an intermediate region where the plasma expands, still belonging to the "Base of the Jet"; and the region beyond the shock where expansion continues, and additional particle acceleration -in an energetic sense- occurs.

### 3.1.1 Nozzle and Energy

The nozzle, is a cylindrical volume of radius  $r_0$  and height  $h_0$ , establishing the base of the jet. It has, at least spectrally, the role of the corona. In relativistic magnetohydrodynamical simulations hot material is removed from the accretion flow and likely is, what enters or becomes the jet ([Markoff et al. 2005](#)). A (relativistic) thermal plasma of electron temperature  $T_e$  is injected into the nozzle. Instead of a thermal distribution one can choose a power law distribution with cut off energy. However, as checked in this work and as stated in [Markoff et al. \(2005\)](#), the results differ only slightly to the thermal distribution when the characteristic energy of both distributions is similar. As [Prieto et al. 2016](#) note, it seems more physical to accelerate the thermal particles to a power law after injection into the jet than accelerating them first and injecting them into the jet afterwards. Hence, for all objects in this work a pure thermal particle distribution is injected into the nozzle. Due to present magnetic fields the electrons radiate synchrotron emission. Their thermal distribution gives rise to a different spectrum than for a power law (see [figure 2.6](#)). In particular, a (relativistic) Maxwellian particle distribution must be inserted in into [equation 2.4.4.1](#), which results qualitatively in a more rounded spectral shape. In the model this spectral component is called preshock component. It is produced by the nozzle and also by the expanding intermediate region up to the shock.

The synchrotron photons of these thermal electrons make up the dominant part of the radiation field. Inverse Compton scattering of these photons off the same entity of electrons, creates the X-ray radiation ([Markoff et al. 2005](#), see [section 2.5](#)). The contribution from photons of the accretion disc to the seed radiation field is minor, synchrotron self Comptonisation (SSC) is the dominant process [Markoff et al. \(2005\)](#). Most Comptonised radiation arises in or close to the base of the jet, since there particle densities and energies are highest.

The most important parameter is the energy normalisation  $N_j$ , in fractions of Eddington luminosity.  $N_j$  is the energy which is given to the particles and magnetic fields in the nozzle. Here an important point shall be highlighted: The total energy entering the jet, the jet power input  $P_j$ , is approximately one order higher than the normalisation  $P_j \sim 10 \times N_j$ . That factor appears, since further energy is necessary to provide the initial collimation of the nozzle and for the distributed acceleration ([Markoff et al. 2005](#)). The total jet power  $P_j$  input must account for the rest frame luminosity, and the magnetic and the kinetic energies carried by the jet. It is noted, that the model assumes same energy density in protons and electrons. If instead assuming same number density,  $N_j$  would be one order higher to yield the same radiative output ([Prieto et al. 2016](#)).

Another very important parameter related to energetics is the equipartition factor  $k$ . It relates the magnetic field energy to the energy density of the radiating particles,  $k = U_B/U_{\text{int}}$ , and is directly linked to the relative strength of synchrotron and Compton losses (see [subsection 2.4.6](#) and [subsection 2.5.4](#)).

### 3.1.2 Compact Jet

Once the nozzle's geometry,  $k$  and  $N_j$  are fixed, energy densities and geometry along the entire jet can be determined. Weak acceleration allows to solve the adiabatic and relativistic

Euler equation for the velocity profile, resulting in a roughly logarithmic velocity dependence upon distance (Falcke 1996). Conservation of energy and particles and lateral expansion with relativistic sound speed, determine the jet's radius, particle density and energy, and magnetic field strength profiles along the jet (Falcke 1996). As mentioned above, the plasma within the base of the jet up to the shock distance  $z_{\text{sh}}$  consists solely of thermal plasma. Starting at  $z_{\text{sh}}$  a fraction of 60 per cent of the thermal plasma is accelerated into a power law energy distribution with index  $p$ . This establishes a power law tail which is maintained along the jet by so-called distributed acceleration. The region beyond the shock radiates the postshock component. Distributed acceleration takes place up to the distance  $z_{\text{max}}$ .

This should not be confused with bulk acceleration: bulk acceleration begins beyond the nozzle where it is strongest and progressively decreases, until the bulk velocity eventually saturates at  $\gamma \sim 2 - 3$  (Markoff et al. 2005). In general bulk acceleration is considered to be weak, in order to allow for solving the adiabatic Euler equation.

The resulting bulk velocity profile is approximatively logarithmic with distance, while the lateral expansion takes place with the constant sound speed of a relativistic gas,  $\beta_s = \sqrt{(\Gamma - 1)/(\Gamma + 1)} \sim 0.4$ , where the adiabatic index is  $\Gamma = 4/3$  (Falcke et al. 1995). Despite radiative losses, adiabatic expansion is assumed to be the dominant cooling process. The cooling is compensated by distributed acceleration, to maintain the particle power law distributions along the jet, where the high energy cut off of the energy distribution is determined by the equilibrium of cooling rates and acceleration. In situ injection is required for explaining the persistence of particle distributions along jets (e.g. Jester et al. 2001). The true mechanism causing distributed acceleration is not further specified in the model, but e.g. diffuse shock acceleration (Jokipii 1987) as well as stochastic resonant acceleration (Miller and Ramaty 1987) are possible mechanisms (Markoff et al. 2005). Electrons distributed in a power law in a homogeneous magnetic field emit the characteristic synchrotron spectrum derived in subsection 2.4.5.

### 3.1.3 Truncated Accretion Disc

The matter inflow is modelled by a geometrically thin truncated multi colour black body, the accretion disc, following Mitsuda et al. (1984); Makishima et al. (1986), and on the pioneering work of Shakura and Sunyaev (1973).

Shakura and Sunyaev (1973) develop a physical model of a Newtonian accretion disc around a black hole of mass  $M$ . Briefly speaking, it is a geometrically thin and optically thick disc, with a radial temperature profile. Its integrated spectrum can be described as the contribution of thermal emission from infinitesimal rings at different temperatures, becoming hotter at smaller radii. The basic idea is to convert locally a fraction of the released gravitational potential energy into black body radiation. A viscosity prescription results in torques, which transport angular momentum outwards. That enables matter to spiral further in, providing the mass supply for the AGN. For simple treatment, equating gravitational release and radiative power for a infinitesimal ring at distance  $r$  leads to (c.f. Makishima et al. 1986)

$$\frac{GM\dot{M} dr}{r^2} \sim r dr T^4 \quad (3.1.3.1)$$

From this simplified equation one can extract the relation  $T(r) \propto r^{-3/4}$ . As it will be discussed in subsection 5.4.1 in more detail, this leads to a composite spectrum with an intermediate region of slope 1/3. The spectral shape of an accretion disc is shown in figure 3.2. Qualitatively, the composite spectrum (and the total luminosity) of the Shakura-Sunyaev accretion disc is dominated by the emission from the inner regions and the outer emission regions extend the composite spectrum towards lower frequencies.

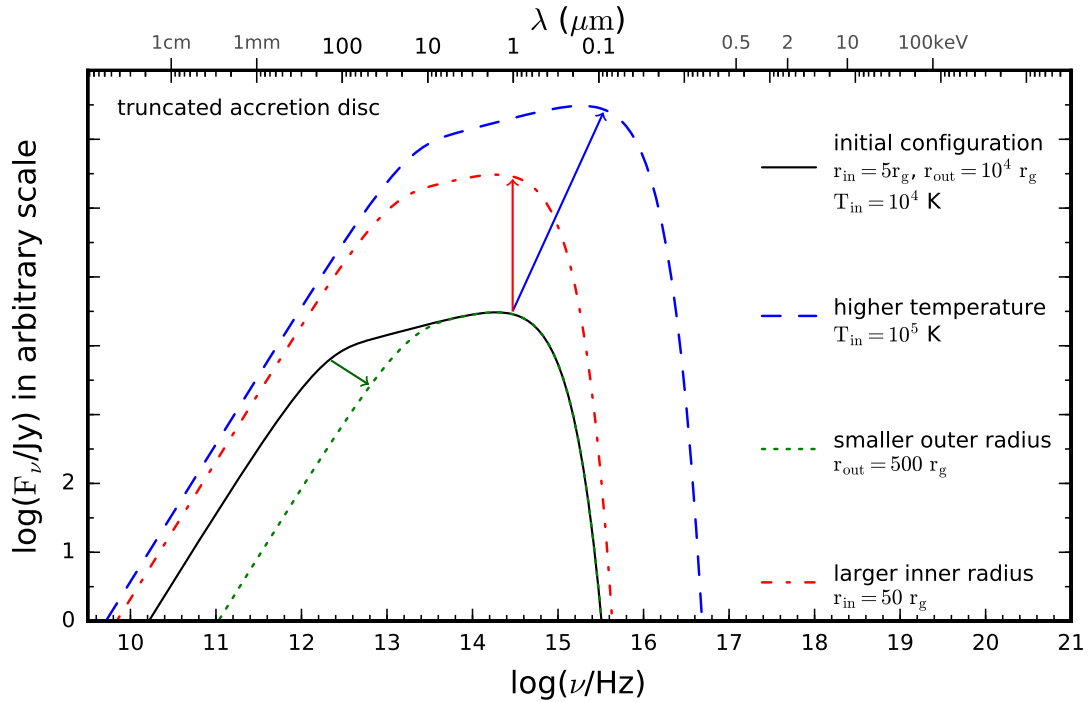


FIGURE 3.2: Spectrum of the thin truncated accretion disc. The y-axis offset is arbitrarily scaled. The solid line shows the shape of the spectrum for the initial configuration. Arrows indicate the qualitative change of the spectrum when changing one parameter. The blue arrow shows how the spectrum changes, for a temperature increase by one order of magnitude, resulting in three orders in flux. The red arrow shows the change for an one order larger inner truncation radius, resulting in two order higher flux. The green arrow shows the change for a order smaller outer disc radius. For the blue-dashed and solid black initial configuration the intermediate region of spectral slope  $\sim 1/3$  is clearly visible. In the low frequency limit the slope approaches 2 (Rayleigh-Jeans limit). The spectra presented here are created with the truncated accretion disc component included in the model.

The standard accretion disc is usually characterised with a fairly high efficiency in converting mass to light. The innermost stable circular orbit ( $3r_g$ ) of a non-rotating black hole corresponds to a binding energy of matter of 5.7 per cent of its rest mass. The innermost stable co-rotating orbit of a maximally rotating Kerr black hole approaches  $r_g$  (e.g. Rees 1984). The binding energy of matter in this orbit is 42 per cent of its rest mass, setting the maximum theoretical efficiency of mass to light conversion. For the accretion disc typically 10 per cent efficiency is assumed in mass to light conversion,  $L_{\text{bol,disc}} = \eta \dot{M} c^2$  (Peterson 1997).

Effects of general relativity are not considered in the description. Firstly, Shakura and Sunyaev (1973), state, that "it is necessary to take into account relativistic effects only in the region  $r < 3r_g$ ". Secondly, Paczyński and Wiita (1980) evolve a concept, of treating the accretion process in a pseudo-Newtonian fashion. Lastly, recent numerical investigations of Campitiello et al. (2017) show, that the accretion disc spectrum is "almost exactly" degenerate with respect to spin, accretion rate and black hole mass. There exists a family of parameter sets of different spins, yielding the same spectrum by appropriate choice of the other parameters: At a fixed viewing angle, there exists a relativistic model equivalent to a standard disc with same accretion rate. Additionally noted, they find a change in the emission pattern characteristic; in detail, thin accretion discs around quickly co-rotating black holes are significantly brighter than the standard disc, especially when observed from high inclinations, due to light-bending. For counter-rotation this effects are inverted.

The accretion disc in the model is implemented following [Mitsuda et al. \(1984\)](#); [Makishima et al. \(1986\)](#). In contrast to the standard disc, which extends in up to the innermost stable orbit at  $3r_g$ , the truncated accretion disc has its inner edge further out, in the distance  $r_{\text{in}}$ . The temperature at the inner edge is  $T_{\text{in}}$ , and the outer radius  $r_{\text{out}}$ . The latter is not constrainable in the present cases and loosely influences the disc's bolometric luminosity. In [figure 3.2](#) the impact of the parameters on the shape is illustrated. The inner edge radius, or truncation radius, marks the transition, where the accretion disc is converted into an inefficiently radiating accretion flow. We assume that this flow does not contribute significantly to the total flux. It is not considered in the model. From a physical point of view it has the function to advect matter further in to the black hole while a fraction is directed into the nozzle. As mentioned above, disc photons can act as seeds for inverse Compton scattering, but they are not the dominant component ([Markoff et al. 2005](#)).<sup>2</sup> On the other hand the accretion disc could be irradiated by the jet, but [Maitra et al. \(2009\)](#) suggest that the influence is small.

## 3.2 The Parameters

All parameters which undergo changes in the process of modelling are listed and briefly described below.<sup>3</sup>

**$n_{\text{H}}$** : This value specifies the hydrogen column density in  $10^{22} \text{ cm}^{-2}$  which is responsible for the extinction of especially soft X-rays.

**$m_{\text{bh}}$** : The mass of the central black hole in solar masses. The black hole mass sets the gravitational radius and therefore the absolute scale of the geometry and the Eddington luminosity (see [subsection 1.1.1](#)).

**$r_{\text{out}}$** : The outer edge of the accretion disc in units of the gravitational radius.

**$N_{\text{j}}$** : This value,  $N_{\text{j}}$  is the energy normalisation in fractions of the Eddington luminosity. This energy enters the the nozzle in form of particles and magnetic fields. Important: this is not the jet power input, which is approximately one order higher (see [section 3.1](#)).

**$p$** : The particles entering the jet are accelerated into a power law energy distribution ( $n(\gamma) \sim \gamma^{-p}$ ) of index  $p$ . The index is linked to the spectral index  $\alpha$  of optically thin synchrotron emission,  $\alpha = (p - 1)/2$  (see [subsection 2.4.4](#)).

**$z_{\text{sh}}$** : The distance in units of the gravitational radius, where the fraction of 60 per cent of the leptons is accelerated to the power law distribution of index  $p$ .

**$r_0$** : The radius of the nozzle in units of the gravitational radius.

**$h_{\text{rat}}$** : The height of the nozzle expressed in units of the nozzle radius  $h_{\text{rat}} = h_0/r_0$ .

**$\theta$** : The inclination  $\theta$  of the model with respect to the line of sight. For  $\theta = 90^\circ$  the jet is parallel to the plane of the sky (disc in edge on view).

<sup>2</sup>The SEDs applied in this work furthermore forbid to include a hot and far inwards extended accretion disc.

<sup>3</sup>The parameters fixed in the entire modelling routine are:  $norm= 1$ ,  $visco= 1$ ,  $mxsw= 1$ ,  $plotsw= 1$ ,  $fsc= 10^{-7}$ ,  $tbb2= 50000$ ,  $bbf2= 10^{-7}$ ,  $irradsw= 0$ .

$T_{\text{in}}$ : The temperature in K of the inner edge of the accretion disc.

$T_{\text{e}}$ : The temperature in K of the radiating particle injected into the nozzle.

$d_{\text{kpc}}$ : The distance of the host galaxy in kpc.

$z_{\text{max}}$ : This is the logarithm of the distance in cm where the acceleration ends.

$k$ : The equipartition parameter is defined as the ration between magnetic energy density and particle energy density,  $k = U_{\text{B}}/U_{\text{e}}$ .

$r_{\text{in}}$ : The inner edge or truncation radius of the accretion disc in units of the gravitational radius. For  $r_{\text{out}} < r_{\text{in}}$  no disc component is present.



## Chapter 4

# The Sample

The model introduced in [chapter 3](#) is the central tool for investigation in this work. Its spectral predictions will be used to characterise a sample of LLAGNs. Therefore the spectral data of the individual nuclei must be as representative as possible of the physical region in direct vicinity of the supermassive black hole. A true picture of this region can only evolve by tracing the emission originating from the very central parsecs: due to their relative faintness highest angular resolution data is necessary to minimise the contamination by light of the host galaxy. Hence, the resolution of the SEDs is the crucial point which strongly determines the results of modelling.

This chapter presents in [section 4.1](#) the observations, which enter the compilation of sub-arcsec resolution SEDs. Consecutively each object is individually presented. Specifically fundamental properties of the host galaxy, observational peculiarities of the nuclear region, and the high angular SEDs are presented. A resume of the fundamental properties can be found in [table 4.1](#)

TABLE 4.1: General Properties of the Sample

LLAGN	$D$ [Mpc]	$M_{\text{BH}}$ [ $M_{\odot}$ ]	$L_{\text{Edd}}$ [ $\text{erg s}^{-1}$ ]	$\theta$	$n_{\text{H}}$ [ $10^{20} \text{cm}^{-2}$ ]	Type	Scale 1'' in pc	Ref.
(1)	(2)	(3)	(4)	(5)	(6)	(7)	(8)	(9)
NGC 4594	9.4	$1 \times 10^9$	$1.26 \times 10^{47}$	$\lesssim 25^\circ$	$18_{-1}^{+1}$	LINER 2	46	a, b, c, d, e
NGC 1097	14.5	$1.4_{-0.32}^{+0.27} \times 10^8$	$1.76 \times 10^{46}$	$< 90^\circ$	$2.3_{-1.7}^{+2.8}$	LINER I	70	f, g, h, i, j
NGC 1052	18.0	$1.54 \times 10^8$	$1.94 \times 10^{46}$	$64^\circ - 87^\circ$	$\sim 1^{2-3}$	LINER 1.9	87	k, l, m, n, e

**Notes.** (1) Name; (2) Distance; (3) Black hole mass in units of solar masses; (4) Eddington luminosity inferred from  $M_{\text{BH}}$ ; (5) Inclination; (6) Total hydrogen column density; (7) Type; (8) linear scale inferred from  $D$ ; (9) **References** for columns 2, 3, 5, 6, 7: (a) [Ajhar et al. \(1997\)](#) (b) [Kormendy et al. \(1996\)](#) (c) [Hada et al. \(2013\)](#) (d) [Pellegrini et al. \(2003\)](#) (e) [Heckman \(1980\)](#) (f) [Tully \(1988\)](#) (g) [Onishi et al. \(2015\)](#) (h) [Mezcua and Prieto \(2014\)](#) (i) [Nemmen et al. \(2006\)](#) (j) [Storchi-Bergmann et al. \(1993\)](#) (k) [Jensen et al. \(2003\)](#) (l) [Woo and Urry \(2002\)](#) (m) [Baczko et al. \(2016\)](#) (n) see [section 4.4](#).

### 4.1 High Angular Resolution SEDs

This work is based on high angular resolution datasets covering the nuclear regions of the galaxies in the sample in multiple spectral regions -radio, IR, visible, UV and X-rays. These include observations acquired with the Very Large Telescope (VLT) using Adaptive Optics in the near-IR (NACO) and diffraction limited imaging in the mid-IR (VISIR), which provide sub-arcsec ( $\lesssim 0.4''$ ) resolution to truly image the nucleus ([Fernández-Ontiveros et al. 2013](#); [Reunanen et al. 2010](#)). In the visible/UV archival data of highest resolution available of the *Hubble Space Telescope* (HST) complement the observations. Nuclear fluxes are measured using aperture photometry of the unresolved central component by subtracting the local background from an annulus. The spectral ranges are completed by flux measurements in radio and X-ray, which have been collected by an extensive and careful search

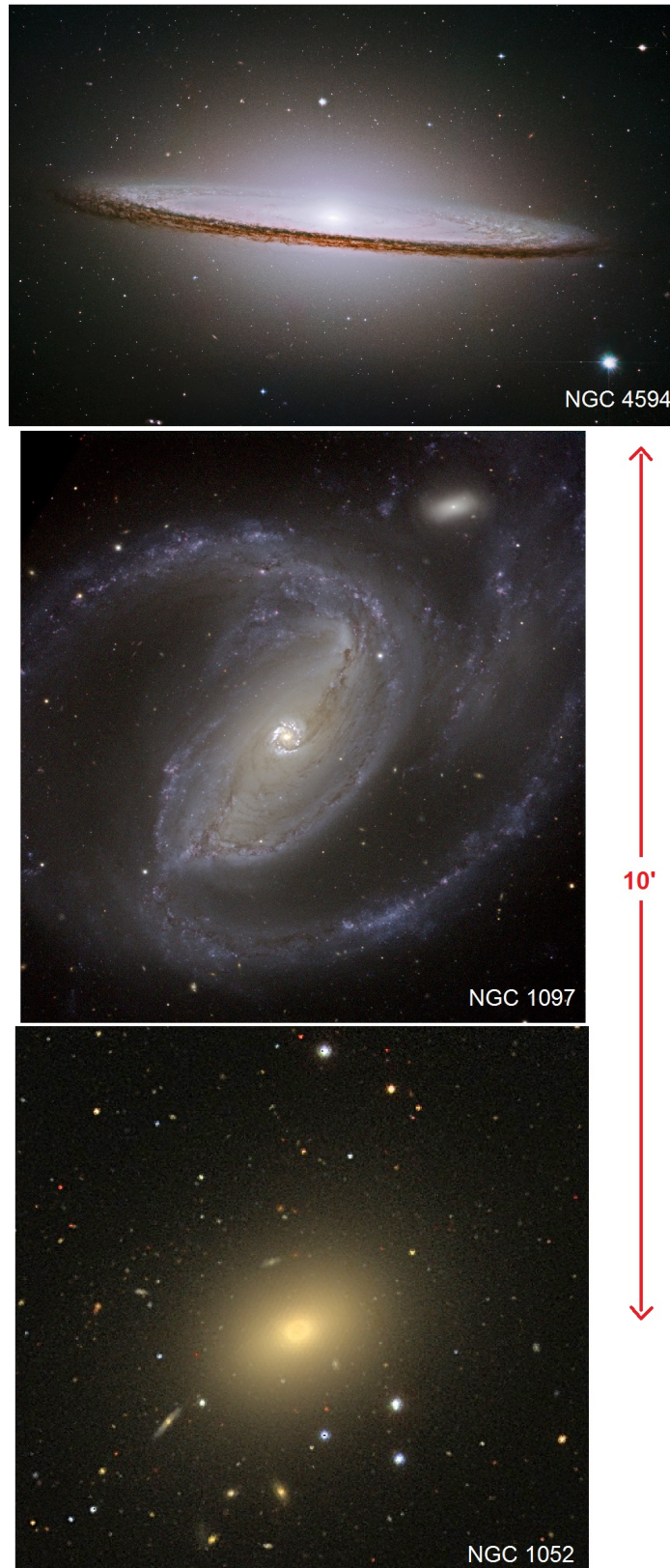


FIGURE 4.1: The Sample Galaxies, NGC 4594, NGC 1097, and NGC 1052 in a common scale. B, V, and R filter overlay from *HST* for NGC 4594, and from VLT for NGC 1097. NGC 1052 colour image extracted from the Sloan Digitized Sky Survey (SDSS). Credit: ESO *HST*, VLT; SDSS (Simbad). Sub-arcsec resolution (in this work  $\lesssim 0.4''$ ) corresponds to less than one single dot or pixel in the picture. This thesis is modelling the individual central pixel - yet, that central pixel is the master of the whole galaxy (Almudena Prieto).

in the literature. Radio measurements, mainly coming from Very Large Array (VLA) and Very Long Baseline Interferometry (VLBI), are naturally of even higher spatial resolution and thus image nuclear (or jet) emission. In the contrary X-ray observations from *Chandra*, *XMM-Newton*, *Integral*, and *Nustar*, have lower spatial resolution but can be consistently compared to sub-arcsec measurements at other frequencies, since the high energy flux is dominated by the nucleus, with negligible contribution from the host galaxy.

Applying these methods similarly to several objects leads to well sampled SEDs at sub-arcsec ( $< 50$  pc at the distance of the galaxies in our sample) resolution of the nuclear region over nearly the entire electromagnetic spectrum (see Prieto et al. 2010; Fernández-Ontiveros et al. 2012, 2013; Prieto et al. 2016). In addition to the unprecedented resolution, the application of the same methods for several objects is an indispensable prerequisite for inter comparison.

An essential requisite for these high quality SEDs is high angular resolution IR imaging by Adaptive Optics acquired with the VLT (NACO). Without this, the SEDs are poorly constrained in the IR. Only few nearby galaxies of the southern hemisphere which contain point-like nuclei in the IR can be studied in this detail by the VLT. This, and the faint nature of LLAGNs restrict the number of LLAGNs available for this sort of observations to only few nearby galaxies on the southern hemisphere. This is the reason for the choice of this particular sample. All objects investigated in this thesis, namely NGC 1052, NGC 4594, and NGC 1097 fulfil these requirements and contain high angular data in the mid-IR. The SEDs are updated versions of the SEDs presented in (Prieto et al. 2010; Fernández-Ontiveros et al. 2012).

Multi epoch observations frequently show short and/or long times-scale flux variability of different strengths, where coarsely speaking variability increases towards higher frequencies and larger time-scales. In order to minimise bias in the SEDs by comparing measurements of different times with different nuclear activity levels, contemporaneity of the selected data is essential. Hence, whenever possible, measurements from the same epochs are included. If not, the only possibility is to trace fluxes over time to avoid including measurements of extreme activity, e.g. of outbursts, and measure the intrinsic variability. If significant variability is present, its impact will be individually discussed.

The data selection for modelling consists of primarily high resolution data, the SEDs are shown in chapter 4. Under specific conditions low resolution data is used to complement the SED, but only when firstly, at this frequency no high angular resolution is available, and secondly the low resolution data smoothly follows the visible trend imposed by the high angular resolution data. The second requirement shall avoid biasing the model towards higher fluxes by the low resolution data. The inclusion of low resolution data is noted in the individual SED and discussion.

For later modelling, the X-ray region of each SED is supplemented with a calibrated and reduced X-ray spectrum from the archive.

## 4.2 NGC4594

NGC 4594, M104, or also known as the Sombrero galaxy, is a nearby galaxy of Hubble morphological type Sab (de Vaucouleurs et al. 1991), for which a distance of 9.4 Mpc (Ajhar et al. 1997) is assumed throughout this work. NGC 4594 contains a stellar disc with approximately exponential brightness distribution (van Houten 1961), while the optical structure of the large bulge resembles that of a giant elliptical galaxy (Faber et al. 1977). The H1, coincident with the dust distribution, is situated in two concentric rings, outside the optical bulge (Bajaja et al. 1984).

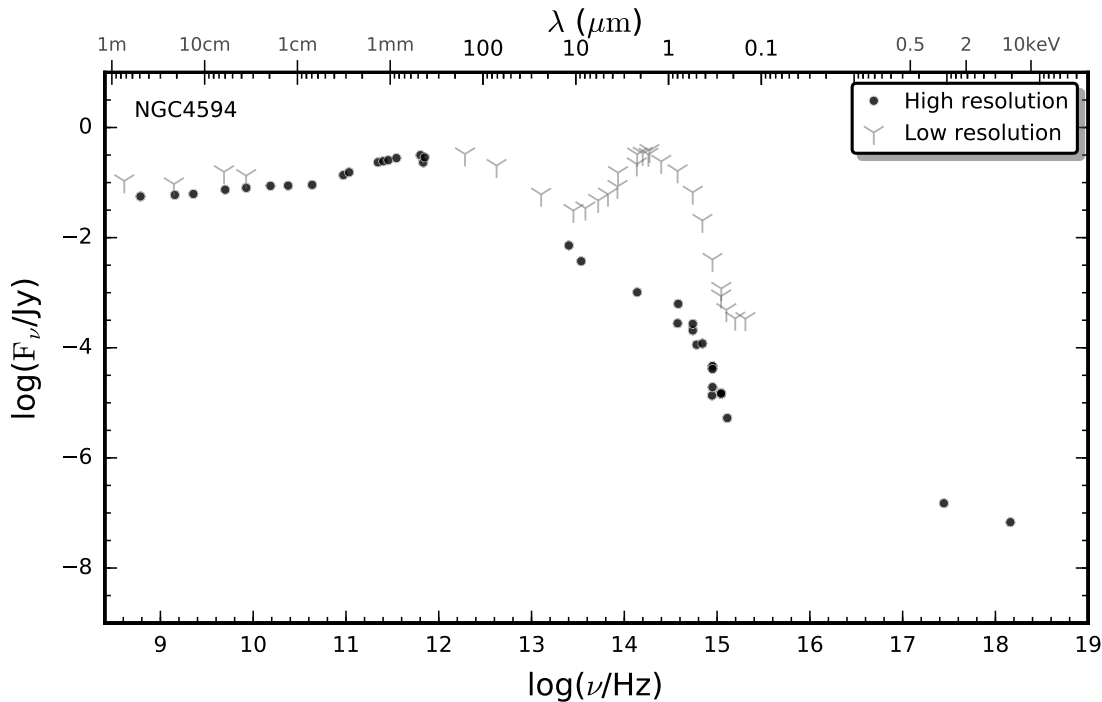


FIGURE 4.2: SED of NGC 4594. The double logarithmic plot shows the flux (Jy) versus frequency (Hz). High angular observational data is represented by black dots, the grey spikes are measurements of lower resolution.

It harbours a type 2 LINER (Heckman 1980), which is faint, although its SMBH is the heaviest in the sample with  $\sim 1 \times 10^9 M_{\odot}$  (Kormendy et al. 1996). Optical and X-ray observations show an unobscured nucleus (Ho et al. 1997; González-Martín et al. 2006).

While low resolution X-ray observations (50") show higher X-ray luminosities ( $L_{0.2-4 \text{ keV}} = 1.1 \times 10^{41} \text{ erg s}^{-1}$ ,  $L_{2-10 \text{ keV}} \sim 1.1 \times 10^{41} \text{ erg s}^{-1}$ ) and softer spectra (e.g. Nicholson et al. 1998), nuclear extraction (15") reveals X-ray luminosities of  $L_{0.1-2.4 \text{ keV}} \sim 1 \times 10^{40} \text{ erg s}^{-1}$ ,  $L_{2-10 \text{ keV}} \sim 1.5 \times 10^{40} \text{ erg s}^{-1}$  (Fabbiano and Juda 1997; Pellegrini et al. 2003).<sup>1</sup> By modelling a thermal hot gas component for the extended and presumably softer X-ray component Pellegrini et al. (2003) derive a Bondi accretion rate (see Bondi 1952), whose expected luminosity is far higher than the observations. They conclude, that either accretion is radiatively inefficient and/or the mass supply is far less than idealised Bondi-accretion predicts. They find a nuclear hydrogen column density of  $\sim 1.8 \times 10^{21} \text{ cm}^{-2}$ . In this SED the X-rays are covered with calibrated and reduced archival *Chandra* data from December 2008. It covers the 0.3-8 keV range with a total exposure time of 90 ks. The dataset used here differs in the overall flux level to the observations of Pellegrini et al. (2003) by a factor of 2-3, therefore the source might be variable up to a factor 2-3. Different X-ray observations suggest only possible variability of the nucleus (Fabbiano and Juda 1997).

A compact and variable (de Bruyn et al. 1976) flat continuum radio core with an extended jet (Mezcua and Prieto 2014) is attributed to the point like optical nucleus (Hummel et al. 1984). Multi wavelength radio observations by Hada et al. (2013) show higher symmetry at lower frequencies than for higher frequencies. They conclude a fairly face on view of an of inclination  $\theta \lesssim 25^{\circ}$ , which leads them to the conclusion to have a "true" type

<sup>1</sup>Fabbiano and Juda 1997 find  $\sim 3.5 \times 10^{40} \text{ erg s}^{-1}$  for a luminosity distance of 18 Mpc, which is converted to the 9.4 Mpc assumed in this work.

2 AGN, since there is no BLR detected (e.g. [Nicholson et al. 1998](#)); the bulk motion of the jet appears to be highly sub-relativistic,  $\beta \lesssim 0.2$ .

Despite of the missing signature of a blue bump in the UV, there is a thermal-like bump at  $\sim 1 \mu\text{m}$  (IR) in the high resolution data which shows variability in a time-scale of a few years and thus cannot have a stellar origin ([Fernández-Ontiveros et al. 2012](#)). However the non-detection of the Fe  $K\alpha$  line ([Pellegrini et al. 2003](#)) casts doubts on the presence of an far inward extending typical accretion disk.

### 4.3 NGC 1097

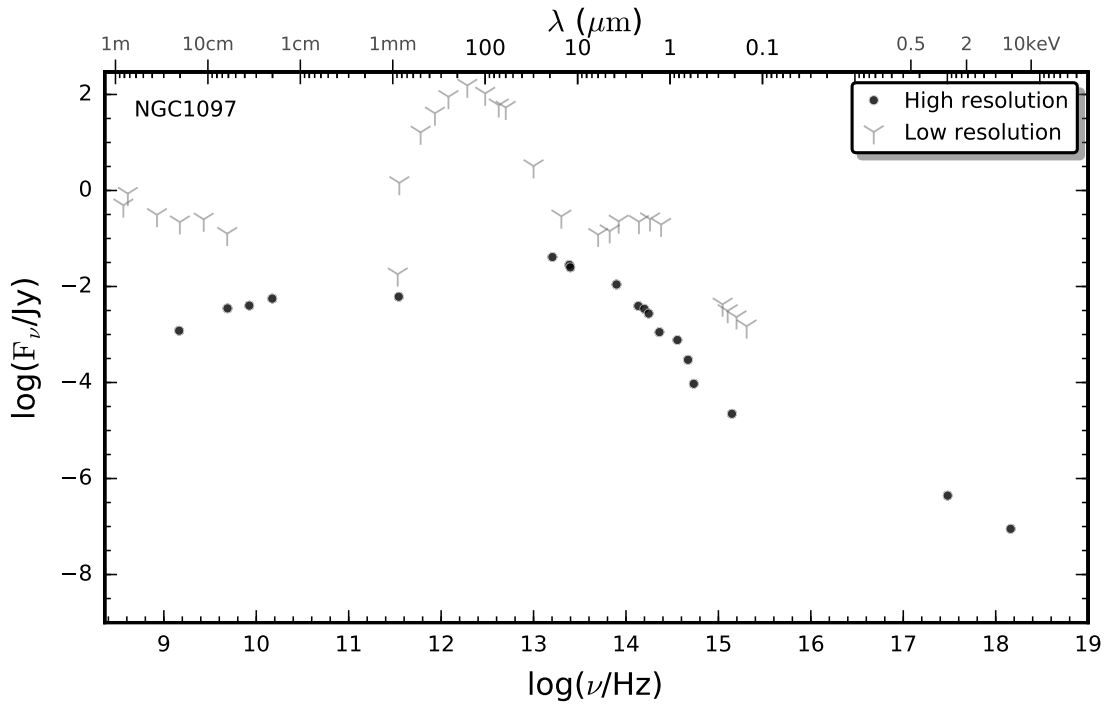


FIGURE 4.3: SED of NGC 1097. The double logarithmic plot shows the flux (Jy) versus frequency (Hz). High angular observational data is represented by black dots, the grey spikes are measurements of lower resolution.

NGC 1097 is a nearby spiral galaxy of Hubble morphological type SB(s)b.<sup>2</sup> In this work a distance of 14.5 Mpc is assumed [Tully \(1988\)](#). There is a prominent star-forming ring with a radius of 5 arcsec around the central region ([Prieto et al. 2010](#)). The LINER 1 shows broad  $H\alpha$  emission lines and harbours a SMBH with a mass of  $1.4 \times 10^8 M_\odot$  ([Storchi-Bergmann et al. 1993](#); [Onishi et al. 2015](#)). The double peaked  $H\alpha$  line was investigated by [Storchi-Bergmann et al. \(1993, 2003\)](#), who derived an inner truncation radius of  $\sim 450 r_g$ .

The nuclear region is visible from radio to UV; [Nemmen et al. \(2006\)](#) find small X-ray extinction, a total hydrogen column density of  $n_H \sim 2.3 \times 10^{20} \text{ cm}^{-2}$ . They furthermore derive a hard X-ray luminosity of  $L_{2-10 \text{ keV}} \sim 4.4 \times 10^{40} \text{ erg s}^{-1}$ , and find a RIAF solution in agreement to the truncation radius. However, their SED is not constrained in the far-IR and only by low angular resolution in the mid-IR and near-IR. At mm-wavelengths a high flux variability of up to one order of magnitude in approximately one year is detected ([Izumi et al. 2017](#)). The nuclear soft X-ray luminosity is  $L_{0.1-2.4 \text{ keV}} \sim 1.2 \pm 0.26 \times 10^{41} \text{ erg s}^{-1}$

<sup>2</sup>NED. <http://ned.ipac.caltech.edu/>

(Perez-Olea and Colina 1996).<sup>3</sup> Nemmen et al. (2006) state within a smaller energy range a lower value of  $L_{0.5-2\text{keV}} \sim 2.5 \times 10^{40} \text{ erg s}^{-1}$ . The present SED is supplemented with a calibrated and reduced archival *Chandra* X-ray spectrum from January 2001. It covers 0.3 – 8 keV with a total exposure time of 5.7 ks.

Mezcua and Prieto (2014) find at 8.4 GHz an extended radio source with two components: a stronger and a fainter one with spatial separation of  $\sim 0.7$  arcsec. This suggests to observe the radio core, and a parsec scale jet somewhat aligned with the line of sight,  $\theta \lesssim 90^\circ$ .

#### 4.4 NGC1052

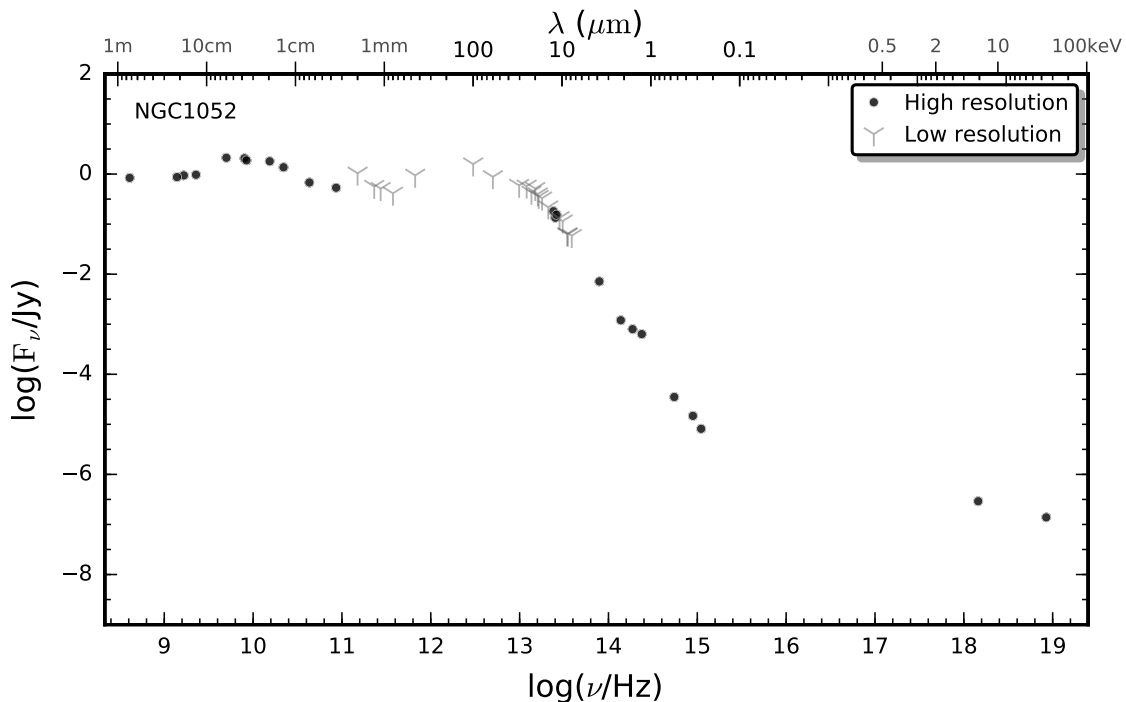


FIGURE 4.4: SED of NGC 1052. The double logarithmic plot shows the flux (Jy) versus frequency (Hz). High angular observational data is represented by black dots, the grey spikes are measurements of lower resolution. For this object only the low angular resolution is shown from far-IR to mid-IR. These data agree in flux level with the high angular resolution data in radio and mid-IR and thus are independent of aperture - a strong indication to be dominated by the point-like nucleus.

NGC 1052 is an elliptical galaxy with elongated shape (E4) and a presumed distance of 18 Mpc is adopted (Fernández-Ontiveros et al. 2012; Jensen et al. 2003). Its nuclear region characterised to be a LINER 1.9 (Heckman 1980), i.e. no broad  $H\beta$  line is detected in the nuclear region. Woo and Urry (2002) estimated a central black hole mass of  $1.54 \times 10^8 M_\odot$ . The galaxy might have experienced a merger approximately one billion years ago (Fernández-Ontiveros et al. 2011 and references therein).

The central kpc region reveals decoupled rotational dynamics of gas and stars (Dopita et al. 2015). In the north east of the nucleus, gas is approaching towards us while it symmetrically recedes in the south west. Barth et al. (1999) found the polarised  $H\alpha$  emission line to be broader than in direct flux measurements. They suggest, that a obscuring torus according to the unified scheme (chapter 1) might be responsible for that.

<sup>3</sup>Adopted to the distance used here.

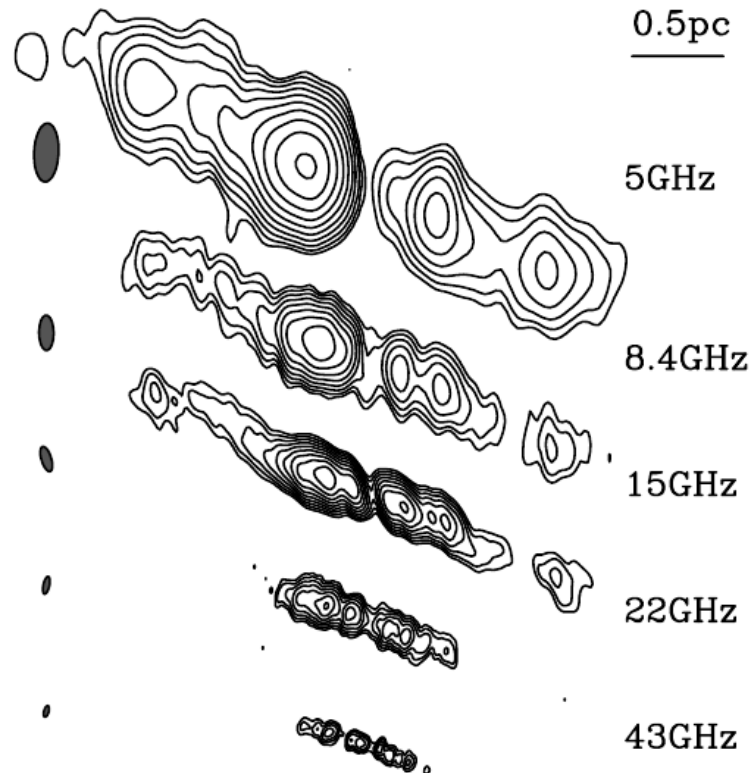


FIGURE 4.5: Contour radio images of the nuclear region of NGC1052. Adopted from [Vermeulen et al. \(2003\)](#). The two-sided jet system at the central parsecs is shown for different frequencies. The emission is shown as contour map with its beam size appropriate to the frequency. The eastern part of the jet is the stronger component and likely the approaching side, somewhat directed towards us. Towards higher frequencies the regions of strongest emission are closer to the centre. At low frequencies there is a gap in the centre, due to free-free absorption by a plasma in front of the nucleus (see text). By definition of the position angle, east is left on the map.

[Kadler et al. \(2004a\)](#) found in their investigation in radio, optical and X-ray, that the positions of emission knots at 1.4 GHz coincides with extended soft X-Ray emission a few arcsec eastward and westward away from the centre. This indicates jet-triggered shocks to be important. [Dopita et al. \(2015\)](#) attribute the diffuse radio emission to a cocoon of hot plasma, which might emerge by the mixing of jet plasma with the ambient medium.

[Heeschen and Puschell \(1983\)](#) monitored the source fluxes at three radio frequencies, namely at 15.5, 31.4 and 89.6 GHz, where they found simultaneous variability at both higher frequencies. Their observations showed outbursts where the flux increased up to a factor of two and declined to its initial value in less than two years. The rise in flux was similarly strong and simultaneous at both higher frequencies. Interestingly the signal at 15.5 GHz was not following the pattern of the higher frequencies. Since the time scale was less than two years, the region where the outburst occurred must be confined within the central parsec, probably very close to the nucleus. The non-detection at the lower frequency suggests, that there might be a free-free absorbing medium in front of the emitting region (see [section A.3](#)).

There exists evidence for an absorber at high angular resolution radio maps (see [figure 4.5](#)) e.g. of [Vermeulen et al. \(2003\)](#). An emission gap around the centre loses its

strength for increasing frequencies, in accordance with the expectations of a free-free absorber.<sup>4</sup> Even more support for a free-free absorbing plasma can be found in [Kameno et al. \(2001\)](#). They analysed the jet emission at three different frequencies. The asymmetry is more pronounced at smaller frequencies, where the western part of the jet is more suppressed. By modelling a free-free absorbing torus and an ambient plasma distribution they explain the observed obscuration, which is more strongly pronounced for the receding part of the jet.

[Kameno et al. \(2001\)](#) interpolated their flux measurements to derive the turnover frequency and peak flux density. By measuring further the angular size of the components and by assuming equipartition they estimated the magnetic field strength of approaching and receding jet component. They argue, that the necessary magnetic field strengths to account for the measured fluxes are too high to sustain synchrotron emission over time (since their injection), when assuming no re-acceleration.

[Vermeulen et al. \(2003\)](#) traced the flux evolution of moving jet components over time. Flux changes with distance demonstrates the patchiness or of the absorber in the foreground. They analyse the 21 cm HI line and find absorption in front of the parsec scale jet structure around the nucleus, likely local to the environment.<sup>5</sup> The most prominent absorption is due to a high velocity (125-200 km s<sup>-1</sup>) hence in-falling system. In front of the receding jet (around 1.5 pc away from the core) its absorption is strongest. The absorption is weaker in front of the approaching jet, and not detected in front of the nucleus. They suggest that the coincidence of non-detection of atomic gas and strongest free-free absorption in front of the nucleus might be due to the ionizing radiation in the proximity to the AGN.

[Impellizzeri et al. \(2008\)](#) detected a broad absorption line of OH at 13.4 GHz, specifically relatively strong in front of the presumably receding western jet, weaker in front of the nucleus, but not detected towards the eastern jet. This imposes evidence for molecular material in the central region. Interestingly, water maser emission is collocated to the OH absorption. [Claussen et al. \(1998\)](#) found in front of the western jet two maser groups, which indicate a velocity gradient of  $\sim 100$  km s<sup>-1</sup> of the receding (with respect to the systemic velocity) maser emission along the western jet. The emission region closer to the nucleus is brighter and more strongly red-shifted. They argue, that there are two possibilities to explain the maser, which is, in their impression not part of a torus like structure: Either the emission could be driven by slow shocks in the jet or around it. Alternatively, the masers could amplify the radio continuum emission of the jet in the background.

[Sawada-Satoh et al. \(2008\)](#) confirmed the masing regions at the western jet and found additional maser emission along the receding jet, also red-shifted. They favour the explanation by the existence of a circumnuclear torus: The red-shifted maser emission is located next to high free-free absorbing opacities. This indicates the presence of contracting material at both edges of a circumnuclear torus.

Besides the findings of ionised, atomic and molecular material in the vicinity of the nucleus, X-ray measurements offer a distinct approach to proof the existence of material in front of the core. [Brenneman et al. \(2009\)](#) found a neutral hydrogen column density of  $\sim 10^{23}$  cm<sup>-2</sup> with a covering fraction<sup>6</sup> of 84 percent and an ionised hydrogen column density of  $\sim 1.37 \times 10^{22}$  cm<sup>-2</sup>. They found neither evidence for Comptonised reflection of X-rays by an accretion disc nor for variability. In contrary [Hernández-García et al. \(2014\)](#) found flux variations for *XMM-Newton* of 20 percent in a time-scale of 8 years. Interestingly these variations led to a change of not only the normalisation constant but also of

<sup>4</sup>[Vermeulen et al. \(2003\)](#) allocated the nucleus by tracing the movement of different jet knots over time, see below.

<sup>5</sup>They measure 21 cm ( $\sim 1.4$  GHz) absorption in front of the jet continuum.

<sup>6</sup>The covering fraction is related to (neutral) clouds which shield direct X-rays.

the molecular hydrogen column density by 32 per cent. By simultaneous fitting of *Chandra* and *XMM-Newton* data their best fit resulted in a column density of molecular hydrogen of  $7.54 \times 10^{22} \text{cm}^{-2}$  for the nuclear region. Connolly et al. (2016) (*Swift*) found a column density of  $8.6 \times 10^{22} \text{cm}^{-2}$  in agreement with Hernández-García et al. (2014), while the covering fraction of 91 per cent they found is in line with Brenneman et al. (2009). Evidence for higher column densities arises from Guainazzi and Antonelli (1999) and Fukazawa et al. (2011), which find  $2.5 \times 10^{23} \text{cm}^{-2}$  and  $2 \times 10^{23} \text{cm}^{-2}$ , respectively. Estimations of Kameno et al. (2001) of the electron column density from their model (see above) derived opacities which results in a similar value,  $\sim 10^{23} \text{cm}^{-2}$ . To sum that paragraph up, there is no consensus on the hydrogen column density, due to variations in the absorbing material in front of the nucleus.

In contrary to all this findings above there is evidence for an freely visible nucleus. The high angular resolution SED (see figure 4.4) shows a visible core in the UV. The core is not hidden by reddening in the UV as expected of a typical LINER 2, but shows a power law spectrum from mid-IR up to the UV. Further there is evidence for non-thermal origin of the radiation from IR to UV: Rieke et al. (1982) found 4.5 per cent linear polarisation in the IR (7" aperture), and Heeschen (1973) found 3.82 per cent linear polarisation in the UV (10"). This high degree of polarisation suggests, that at torus, if present, has a minor contribution to the total emission.

Now we will discuss the inclination of the jet system. Kameno et al. (2001) estimate from first, the 15 GHz flux ratio between jet and counter-jet and second, the apparent velocity from Kellermann et al. (2004) an inclination of  $50^\circ$  and intrinsic jet velocity of  $0.25c$ .<sup>7</sup> A few years later long term VLBI multi-epoch monitoring at 15 GHz was used to perform a kinematic study, by Vermeulen et al. (2003). They traced individual jet knots over time and applied a ballistic model to derive the apparent velocity, which lead to an lower limit of  $57^\circ$  for the inclination. They concluded, that the fairly symmetric structure at 43 GHz suggests small beaming effects (see figure 4.5). A high frequency study at 86 GHz estimated the inclination by the flux ratio of eastern and western jet and the apparent velocity of Vermeulen et al. (2003) (Baczko et al. 2016). They derived the inclination to lie between  $64^\circ - 87^\circ$  and noted, that differences to earlier estimations might be due to several things: underestimation of free-free absorption, curvature or intrinsic asymmetry between the two jets.

Summing up the findings from above, the geometry and kinematic of ionised, atomic and molecular gas in the nuclear region support the existence of an ionised torus. The high inclination, together with the free view in the UV of the nuclear region cast doubt on the presence of an obscuring optically thick dusty torus. The hydrogen column density of  $\sim 10^{23} \text{cm}^{-2}$  is variable. This proves the existence of some material close to the nucleus, but does neither show the expected obscuration of a classical torus, according to the unified scheme. These observations cast doubt on the applicability of the unified model and suggest a more complex structure, consisting of infalling gaseous filaments ionised, shocked and/or ripped apart in the vicinity of the nucleus.

In this SED the X-rays are covered with calibrated and reduced archival *Nustar* data from February 20136. It covers the 1-50 keV range with a total exposure time of 15 ks. The low angular resolution measurements at mm and sub-mm wavelengths follow the trend of the high angular resolution measurements and thus seems to be representative for the nucleus (Fernández-Ontiveros et al. 2012). All low angular resolution measurements shown in figure 4.4 complement the high angular resolution measurements in the modelling.

<sup>7</sup>All these estimations assume intrinsic symmetry of the jets. The flux ratio and the apparent velocity together give two constraints, which allow to solve the unknowns, inclination and intrinsic velocity (see A.2.4).



## Chapter 5

# Methods

After the description of the model in [chapter 3](#) and the sample in [chapter 4](#), we will focus in this chapter on the concrete application of the model to the observational data. In [section 5.1](#) model specific technical details are briefly stated. [Section 5.2](#) explains a basic scheme for obtaining satisfactory model configurations, as far as standardisation is possible. The spectral behaviour of the model is qualitatively given and related to the underlying physical processes introduced in [chapter 2](#). In [section 5.3](#) physical quantities related to the model output are defined. In [section 5.4](#) a method is developed, which allows to infer limits on truncation radius and efficiency of the truncated thin accretion disc, in dependence of observational data and accretion rate.

### 5.1 Invoking the Model

The program `agnjet` is compiled within the Interactive Spectral Investigation System (ISIS) (e.g. [Houck and Denicola 2000](#)).<sup>1</sup> The advantage of ISIS is that it can use ASCII tables of observational data and the X-ray spectrum simultaneously, by folding the model result into X-ray detector space. ISIS fits therefore in both, the physical regime and in the detector space and performs simultaneous  $\chi^2$  minimisation.

ISIS itself is started in the terminal. A script loads the model `agnjet`, the measurements in a table and the X-ray data, together with auxiliary files, which are necessary to map the model spectrum into detector space. The X-ray data is binned, a signal to noise ratio  $S/N=5$  is chosen. An initial parameter configuration is loaded (about the parameters involved see [section 3.2](#)). Then everything is prepared for modelling: The model can be evaluated, the resulting spectrum directly inspected, and parameters changed.

Fitting a complex model to data can become very time consuming. The larger the number of free parameters, the larger are the dimensions of the parameter space. A model with a large number of free parameters like this (compare [section 3.2](#)) is hard to solve iteratively. Especially, there may be multiple local  $\chi^2$  minima, which confuse the iteration. Additionally there might be solutions, which are physically not very meaningful. In that case it is more efficient to trim the model manually first, and find a parameter configuration which is close to a (physical meaningful) minimum, i.e. with a small  $\chi^2$ -value. Then, the final convergence can be found iteratively, because one can enclose the desired minimum in a substantially smaller parameter space.

### 5.2 General Modelling Approach

A general approach is given in what follows, which is found to be useful in determining satisfactory configurations. Specifically the influence of the parameters on the model's continuum spectrum is described. In [chapter 6](#) this scheme will be assumed to be known.

---

<sup>1</sup>For further information, including manual, see <http://space.mit.edu/asc/isis/index.html>.

Deviations from this procedure due to special peculiarities of the objects will there be discussed in their individual treatment.

There are in total four model parameters which can be constrained by complementary observations. These parameters are namely the distance  $d_{\text{kpc}}$ , the mass of the central black hole  $m_{\text{bh}}$ , the inclination  $\theta$  and the hydrogen column density  $n_{\text{H}}$ . If not stated otherwise, they are fixed at their individual value and enter modelling as input.

We will focus first on the emission originating from the jet, i.e. preshock, postshock, and Compton component. We assume for this scheme, that no disc signature is present in the data. How to invoke the accretion disc ( $T_{\text{in}}, r_{\text{in}}, r_{\text{out}}$ ) will be explained afterwards. The following parameters determine the shape of the jet spectrum: power normalisation  $N_{\text{j}}$ , electron temperature  $T_e$ , nozzle radius  $r_0$ , nozzle height  $h_{\text{rat}}$ , equipartition  $k$ , power law index  $p$  and shock distance  $z_{\text{sh}}$ . The end of distributed acceleration  $z_{\text{max}}$  has only loose influence on the spectrum. It determines the radio cut off frequency and is chosen sufficiently large  $z_{\text{max}} \gtrsim 10^{17}$  cm.

The power normalisation  $N_{\text{j}}$  sets the overall emission level. A good start is to adopt the (postshock) spectrum approximately to the radio data. A higher value results, spectrally spoken, mainly in a vertical shift upwards of the entire spectrum. Additionally, the preshock and Compton component move towards higher frequencies, the Compton component increases most strongly. Physically, a higher energy density in the nozzle results in stronger magnetic fields and higher particle densities. The former shifts the preshock emission to higher frequencies, while the latter enhances the emission. Compton emission is sensitive to the denser and more energetic radiation (preshock) field and higher electron density. This together results in a disproportional increase of the Compton component.

In what follows, we will focus on the interplay between preshock and Compton component. The next step is to consider the nozzle temperature  $T_e$  and radius  $r_0$  to shape the preshock component. At the same time slope and curvature of the Compton component should be brought into agreement with the X-ray dataset. A higher temperature  $T_e$  broadens the preshock and Compton component, where the change of the latter is more pronounced. Physically, a higher temperature of the particle distribution results in a broadening of the preshock component, due to its Maxwellian nature. By broader energy range of seed photons and broader energy distribution of the electrons the broadening effect strengthens in the Compton component.

A larger nozzle radius  $r_0$  shifts the preshock component approximately horizontally towards lower frequencies. The Compton component also is shifted towards lower frequencies, while its strength decreases. Physically, a larger nozzle radius  $r_0$  leads to bigger nozzle volume and in turn to lower magnetic field energy density. The typical photon energy decreases,  $\nu_{\text{T}} \propto B \propto U_{\text{B}}^{1/2} \propto r_0^{-1}$ . The total number of emitting particles, and hence photons, remains constant. As result the preshock component shifts approximately horizontally towards lower frequencies. The larger volume implies a lower seed radiation field density. This and lower seed photon frequencies shift the Compton component downwards and towards lower frequencies.

At this point the radio regime should be in agreement with the data, the preshock component should follow the data, and the Compton component should be vertically shifted to the X-ray observations, while slope and curvature visually agree. The emission level of the Compton component is sensitive on Nozzle height and equipartition parameter. By adapting them, spectral agreement between model and observational data can be reached in the detector space. While synchrotron emission is proportional to particle number, Compton emission is proportional on the particle number squared. Therefore the Compton flux increases strongly for higher nozzle. Increasing the equipartition value  $k$  above equipartition lowers the synchrotron flux. When more energy feeds the magnetic fields (the preshock

component moves slightly to higher energies), the particle density is less. The synchrotron source becomes less efficient when leaving equipartition, the radiation field energy density decreases. Smaller particle density and smaller radiation field density result in an disproportional decrease of the Compton component.

It might be necessary to repeat these changes to find visual agreement and reduce the  $\chi^2$  value further. As soon as sufficiently small  $\chi^2$  values are found, it is promising to be in the vicinity of the global minimum.<sup>2</sup>

This is the time for fine-tuning the postshock component. Parameters directly connected to the postshock component are the power law energy distribution index  $p$  of the accelerated electrons, which is connected to the optically thin synchrotron emission slope, and the shock distance  $z_{\text{sh}}$ , which sets the distance where particle acceleration begins. A higher power law index produces a steeper postshock slope in the optically thin part. A larger shock distance shifts the postshock turnover frequency towards lower frequencies. Physically spoken, increasing the latter lowers the maximum energy available for the electrons at the shock and therefore shifts the optically thin component vertically downwards. This way the turnover frequency between inverted (optically thin) and flat (superposition of components) is shifted towards lower frequencies. However, the changes of the overall spectrum are small. This is, because in turn the preshock emission extends farther towards low frequencies.  $p$  is connected with the slope  $\alpha$  of the optically thin synchrotron spectrum. The objects studied in this work possess a dominant preshock component from IR to UV, and the X-ray data is dominated by the Compton component. Hence  $p$  has only minor influence on the spectrum. It should have a value which is sufficiently large, to reduce active participation in the representation of observational data. Otherwise the subsequent parameter search iteration might be confused.

The automatic parameter search iteration is carried out by ISIS, which samples the parameter space of the specified parameters and constructs single parameter confidence intervals. It was found to be promising to vary all important parameter which define preshock and Compton component simultaneously, in detail  $N_j, T_e, r_0, h_{\text{rat}}, k$ . Whenever ISIS finds an improved fit for a new parameter the confidence search is automatically restarted.<sup>3</sup> This procedure is repeated until no improved fit is found any more. At this stage  $p$  and  $z_{\text{sh}}$  can be lowered, until the postshock component is limited by observational data (UV or soft X-ray). They are fixed at their new values. Now the iteration should be started again, as their might be minor changes induced by the postshock component.

When final confidence intervals are searched, the initial parameter intervals should be fairly enlarged to ensure that all confidence intervals lie inside. This furthermore reduces the likelihood to be next to an only local minimum and not the global one. This final confidence search is the most time consuming task.<sup>4</sup> The confidence intervals are not subject of further parameter investigation, but are rather a validation of having found the stable  $\chi^2$  minimum within the initial parameter interval.

Finally we deal with the truncated accretion disc. The disc is uniquely defined by its inner edge radius  $r_{\text{in}}$ , temperature  $T_{\text{in}}$ , and outer radius  $r_{\text{out}}$  (illustrated in [figure 3.2](#), see [section 5.4](#)). For the case described above, i.e. no signature of the disc visible in the data,

<sup>2</sup>What low values are, is dependent on the individual SED and differs from object to object. More important are visual agreement and the impression to have found a configuration, where further manual improvements become too laborious.

<sup>3</sup>If one parameter confidence interval can not be found, the limits are outside the initial parameter interval. This indicates that a parameter propagates towards an edge of its interval and the current parameter values should be checked (recent parameter file in the folder specified above). This way one can check whether changes must be made.

<sup>4</sup>It is advisable to run the calculations over night. The calculations were carried out with an usual 4 core laptop with 2.5 GHz and 4 GB RAM. Increasing the swap partition to 9 GB -effectively around 12 GB of free memory for ISIS- was necessary in order to avoid system freezes. ISIS supports parallel processing.

model-independent properties of the accretion disc can be constrained by the observational data. Specifically, the IR-UV flux measurements can be used to constrain upper limits on the accretion disc fluxes and hence luminosity, which can be used to derive robust limits, see [section 5.4](#). In order to do this, the inner accretion disc radius  $r_{\text{in}}$  is chosen to  $5r_g$  and subsequently the inner edge temperature  $T_{\text{in}}$  is varied until the thermal spectrum "touches" the data. If in contrast to above a thermal signature is visible, the disc must be adopted to it, before any iterations with regard of jet emission are carried out.

The observational SED, the resulting model spectrum, and the converged model parameters enter into further analysis.

### 5.3 Analysis

One result is the bolometric luminosity obtained from the model spectrum by linear interpolation. The integration of the jet, i.e. preshock, postshock and Compton component is carried out by assuming isotropy. The accretion disc luminosity is corrected for a Lambertian inclined source ([subsection 2.1.1](#)),

$$L_{\text{disc}} = \frac{2\pi}{\cos(\theta)} \int F d\nu \quad (5.3.0.1)$$

The radiative output luminosities from spectral integrations are

- $L_{R-UV}$ : Radio to UV (R-UV) model luminosity (integrated from 1 GHz up to 13.6 eV)
- $L_{0.5-2 \text{ keV}}$ : Soft X-ray luminosity from 0.5 keV to 2 keV
- $L_{2-10 \text{ keV}}$ : Hard X-ray luminosity from 2 keV to 10 keV

The integration is split up, to compare with observed fluxes. For later energetic considerations the further quantities will be defined:

- $L_j$ : Model integrated jet bolometric luminosity (affected by beaming). This value can be considered as a main result from modelling.  $\chi^2$  minimisation tries to reproduce the observed fluxes over the entire sampled spectrum.
- $L_{\text{RF}}$ : Model jet rest frame luminosity. This is the inferred intrinsic luminosity of the jet. To estimate  $L_{\text{RF}}$ , the range for the accessible boosting factors are calculated, which enclose the value. If available, inclination and maximum bulk velocities from the literature are used, together with the assumption of a continuous jet (see [A.2.4](#)). If not, the values produced for lowest ( $90^\circ$ ) and highest boosting ( $\sim 2^\circ$ ) are used as limits.
- $P_j$ : This is the total jet power. This power is required to supply radiative ( $L_{\text{RF}}$ ) and kinetic output and magnetic fields. It is proportional to the energy normalisation parameter  $P_j \sim 10N_j$
- $b$ : The boosting factor  $b$  connects the model integrated jet bolometric luminosity and the rest frame luminosity,  $b = L_j/L_{\text{RF}}$ .

The general approach of the quantitative analysis is to establish relations between these parameters. One robust result is the accretion disc luminosity,  $L_{\text{disc}}$ . By assigning a certain efficiency  $\eta$  to it, its power budget, i.e. the energy equivalent transported inwards in form of mass can be calculated. Comparing this with  $L_{\text{RF}}$  allows to perform a first order energetic balance, e.g. estimate boosting factors or infer the efficiency (see [5.4.2](#)).

## 5.4 Black Body Considerations

A common feature of LLAGN's spectra is the missing blue bump - the SEDs follow rather a power law like behaviour from IR to UV (section 1.3). According to the recent picture of LLAGNs, a truncated accretion disc is expected outside of the RIAF (Ho 2008). This section develops a method starting from Shakura and Sunyaev (1973), which allows to derive limits on the truncated accretion disc's inner radius, mass to light conversion efficiency, temperature, and luminosity. The basic assumptions entering are firstly, that the observational data follows a power law, and secondly, that the accretion disc has a certain accretion rate.

### 5.4.1 Single and Multi Temperature Black Body

At first the behaviour of a single temperature black body radiator is investigated. It shall be carried out, what constraints on distance, temperature and angular size follow, when imposing flux limits by observational data. In order to do this, we consider the Planck formula 2.2.0.1. Substituting  $T$  with  $\nu_{\max}$ , according to Wien's displacement law, and going into log-log space, the equation can be rewritten to

$$\log F(\nu_{\max}) = \log [\Delta\Omega B_{\nu_{\max}}(T)] \propto -2 \log D + 2 \log r + 3 \log \nu_{\max} \quad (5.4.1.1)$$

The area of the black body is considered to be circular and of size  $\pi r^2$  in a distance  $D$ . It covers the solid angle  $\Delta\Omega = \pi r^2/D^2$  in the plane of the sky. Constants are neglected and the distance will be fixed, because the focus shall be on the dependencies. The flux of the emission peak only depends on the area's radius  $r$  of the source and the peak frequency, where the second is tightly linked to the temperature. Visually this relation can be interpreted in log-log space as follows: Increasing the emitting area shifts the peak vertically upwards, while the temperature dependent peak emission frequency shifts the peak along a line with a slope of 3 (equation 2.2.0.2, see figure 3.2).

For a given flux measurement at a frequency the properties of the black body are well defined by assuming the observed frequency to be exactly the peak frequency. Area and temperature of a single-temperature black body can be calculated uniquely. The bolometric luminosity of the black body,  $\propto r^2 T^4$ , can also be inferred directly (see equation 2.2.0.4).

Assuming that points follow a power law of a certain slope,  $F_\nu \propto \nu^{-\alpha}$ , the following considerations can be made. There exists a family of black body functions, whose peaks are all touching the power slope line. Their peaks are then constrained by  $2 \log r + 3 \log \nu \propto -\alpha \log \nu$ , which imposes a relation between radius  $r$  and peak frequency  $\nu$

$$\log r \propto -\frac{\alpha + 3}{2} \log \nu \quad (5.4.1.2)$$

Inserting this equation into the bolometric luminosity results in

$$\log L \propto (1 - \alpha) \log \nu \quad (5.4.1.3)$$

Letting  $\nu_1 < \nu_2 < \nu_3$ , the following considerations can be made:

1.  $\alpha = 1$ : Shifting the peak towards higher frequencies the area must scale as  $A \propto \nu^{-4}$  not to exceed the data points; the bolometric luminosity of the black body remains constant
2.  $\alpha > 1$ : Shifting the peak towards higher frequencies the area must scale down quicker than  $A \propto \nu^{-4}$  resulting in a decreasing bolometric luminosity

3.  $\alpha < 1$ : Shifting the peak towards higher frequencies the area must scale down slower than  $A \propto \nu^{-4}$  resulting in a increasing bolometric luminosity
4. For  $\alpha > 0$  a data point situated at  $\nu_1$  can not be explained by a black body whose peak is situated at  $\nu_2$ , because the peak would exceed the power law at  $\nu_2$
5. Joining 3. and 4.: For a convex broken power law  $\alpha_1 < 1$  in  $[\nu_1, \nu_2]$  and  $\alpha_2 > 1$  in  $[\nu_2, \nu_3]$  the one temperature black body with the highest luminosity can be "hidden" at  $\nu_2$

Additional constraints on the maximum physical size of the one temperature black body can be derived from the spatial resolution of the observational data. If the observed flux originates from a point like source, its maximum linear radius in the plane of the sky is limited by the resolution as  $r \lesssim \theta^2$ , where  $\theta$  is the smallest resolvable linear scale. An elongated source of the same area might exceed the resolution limit - this is a strict limit.

Now a composite spectrum of individual infinitesimal components, each with its own temperature and area is set up by assuming a power-law scaling for simplicity. Further is assumed, that the sum of components produces a composite spectrum similar to the sum of solely the components' peaks. In other words, at a certain frequency only the peaking component contributes.<sup>5</sup> We will consider a disc-shaped black body with a radial temperature power-law profile

$$T(r) \propto r^{-s} \propto \nu(r) \quad (5.4.1.4)$$

with arbitrary finite inner and outer edge. The peak intensity of each infinitesimal ring contributes to the composite spectrum of the disc. Flux and luminosity released within a ring at distance  $r$  of thickness  $dr$ , respectively integrated, scale as

$$dF_\nu \sim r T^3(r) dr \sim r^{1-3s} dr; \quad F_\nu \sim r^{2-3s} \sim \nu^{3-2/s} \quad (5.4.1.5)$$

$$dL \sim r T^4(r) dr \sim r^{1-4s} dr; \quad L \sim r^{2-4s} \sim \nu^{4-2/s} \quad (5.4.1.6)$$

For example, a flat composite spectrum is obtained for  $s = 2/3$ . For larger  $s$  indices, the temperature decreases outwards more quickly and the composite spectrum is dominated by higher frequencies, hence the innermost part makes up the peak emission. For the luminosity the threshold to consider is  $s = 1/2$ . For larger  $s$ , the luminosity decreases outwards and the innermost part dominates the luminosity.

## 5.4.2 Efficiency Scaling of the Truncated Accretion Disc

The radial temperature profile of the (thin) accretion disc scales as  $s = 3/4$ . This was introduced briefly in [subsection 3.1.3](#). The resulting composite spectrum has a slope of  $F \propto \nu^{1/3}$ : luminosity and flux are dominated by the inner region. The more exact treatment of [Shakura and Sunyaev \(1973\)](#) includes viscosity. Their result is

$$\frac{dL(r)}{dA} = \frac{3}{8\pi} \dot{M} \frac{GM}{r^3} \left(1 - \sqrt{r_b/r}\right) \quad (5.4.2.1)$$

for the luminosity released at a certain distance from the centre per surface unit, where they introduced  $r_b = 6r_g$  as inner disc boundary. This equation will now be used as a starting point to infer an scaling of the efficiency with inner truncation radius. As they note, if considering the luminosity radiated within an interval  $L(r_1, r_2) = 4\pi \int_{r_1}^{r_2} [dL(r)/dA] r dr$ ,

<sup>5</sup>This is the same concept as used for synchrotron ([section 2.4](#)) and inverse Compton ([section 2.5](#)) emission (compare [Jones 1968](#), and [subsection 2.5.4](#)).

where  $r_1, r_2 \gg r_b$ , the last term in the bracket,  $\sqrt{r_b/r}$ , vanishes, leading to

$$L(r_1, r_2) \approx \frac{3}{2} \dot{M} GM \left( \frac{1}{r_1} - \frac{1}{r_2} \right) \quad (5.4.2.2)$$

This imposes a strict upper limit on the luminosity,  $L(r_1) \leq 3\dot{M}GM/(2r_1)$  for  $r_2 \rightarrow \infty$ .

For the purpose of considering also smaller radii, the integration can be carried out without this approximation, leading instead to

$$L(r_1, r_2) = \frac{3}{2} \dot{M} GM \left[ \left( \frac{1}{r_1} - \frac{1}{r_2} \right) - \frac{2r_b^{1/2}}{3} \left( \frac{1}{r_1^{3/2}} - \frac{1}{r_2^{3/2}} \right) \right] \quad (5.4.2.3)$$

Taking along the rear term in the bracket of [equation 5.4.2.1](#)  $\sqrt{r_b/r}$ , lowers the luminosity originating from the inner regions of the accretion disc, the upper limit obtained above strictly holds. [Shakura and Sunyaev \(1973\)](#) note, that this rear term is present, because gravitational energy released in the innermost regions of the disc is mechanically transported outwards, before being converted into heat.

Now by setting  $r_b = r_1$  one obtains

$$L(r_1, r_2) = \frac{\dot{M} GM}{2r_1} [1 - C(r_2/r_1)] \quad (5.4.2.4)$$

where the correction function is defined as

$$C(r_2/r_1) = \frac{r_1}{r_2} \left( 3 - 2\sqrt{\frac{r_2}{r_1}} \right) \quad (5.4.2.5)$$

The correction function reduces the luminosity for finite  $r_2$ . For outer radius approaching infinity,  $C(r_2/r_1) \sim 0$  and the expression can be simplified to  $L(r_1) \lesssim \dot{M}GM/2r_1$ .

Equating  $r_b$  with  $r_1$  has an important motivation. When calculating the luminosity for an outer ring of a not-truncated disc the luminosity is fairly larger than the luminosity for the same ring of a truncated accretion disc. If the boundary radius is not changed to the truncation radius, one wrongly sums up energy radiated from the outer disc, which originates (was gravitationally released) from the not present inner disc.

By equating [equation 5.4.2.4](#) with the direct mass to luminosity conversion by  $L = \eta \dot{M} c^2$  one yields

$$\frac{\dot{M} GM}{2r_1} [1 - C(r_2/r_1)] = \eta \dot{M} c^2 \quad (5.4.2.6)$$

which can be rewritten by introducing the dimensionless  $\tilde{r}_{\text{in}} = r_1/r_g$  where  $r_g = MG/c^2$ . Then the efficiency is:

$$\eta = \frac{1}{2\tilde{r}_{\text{in}}} [1 - C(r_2/r_1)] \quad (5.4.2.7)$$

A strong limit following from this is

$$\eta \leq \frac{1}{2\tilde{r}_{\text{in}}} \quad (5.4.2.8)$$

for arbitrary finite outer disc radii. To give some feeling for numbers: the correction function takes the values  $C(4) = 0.5$ ,  $C(10) < 0.25$ ,  $C(26) < 0.1$ . Originally their disc is intended to describe non-rotating black holes and therefore their boundary radius is  $6r_g$ . Using that radius results in an efficiency of about 8.3 per cent with this formula, slightly higher than the maximum value for a non-rotating black hole of 5.7 per cent. For rotating black

holes the innermost stable circular radius decreases which allows higher efficiencies. For a maximally rotating black hole the innermost stable circular radius approaches  $r_g$ , which leads to an maximum of 50 per cent according to this formula, which again, is slightly higher than the theoretical maximum efficiency. The formula here (equation 5.4.2.8) shall be used in that sense, that there can not be an accretion disc which is more efficient than the here imposed limit.

Choosing an dimensionless inner truncation radius of  $\tilde{r}_{\text{in}} = 5$  results according to the above estimation in an maximum efficiency of 10 per cent. This is the typically inferred efficiency for the thin accretion disc ( e.g. Peterson 1997, compare subsection 3.1.3). Summing up so far, the maximal efficiency inferred from equation 5.4.2.1 scales inversely with the inner truncation radius of the disc,  $\eta_{\text{max}} = 1/(2\tilde{r}_{\text{in}})$ .

### 5.4.3 Accretion Rate Dependent Limits for Truncation Radius and Efficiency

The maximum limit efficiency scaling,  $\eta_{\text{max}} = 1/(2\tilde{r}_{\text{in}})$ , can now be further used, to derive constraints on the accretion disc. In detail the constraints imposed by the power law observational data are the first requirement. Equation 5.4.1.2 connects inner truncation radius and inner edge temperature. The luminosity is connected to efficiency and accretion rate via  $L \propto \eta\dot{M} \propto \dot{M}/\tilde{r}_{\text{in}}$ . Putting both into equation 5.4.1.3, one yields the following scaling relations

$$\begin{aligned}\log r_{\text{in}} &\propto \frac{3 + \alpha}{3\alpha + 1} \log \dot{M} \\ \log T_{\text{in}} &\propto \frac{-2}{3\alpha + 1} \log \dot{M}\end{aligned}\tag{5.4.3.1}$$

These equations allow to express inner edge radius and temperature as functions of the accretion rate and power law spectral index. When assuming the typical 10 per cent efficiency in mass to light conversion for a "typical" accretion disc with truncation radius  $\tilde{r}_{\text{in}} = 5$ , one can infer a certain accretion rate from its maximum bolometric luminosity imposed by the data. If that accretion rate does not supply enough total power input for e.g. the jet, these equations provide a possibility to change inner edge radius and temperature in accordance with the observational limits to increase the maximum accretion rate the disc can provide. Under the assumption of maximal efficiency  $\eta_{\text{max}} = 1/(2\tilde{r}_{\text{in}})$  this way a lower limit for the truncation radius and upper limit for the inner edge temperature can be obtained. Combining both equations shows, that for common, i.e. positive values of  $\alpha$ , the edge temperature decreases with increasing truncation radius. Therefore considering the radius only is sufficient for the following qualitative statement for a black hole of a given mass: A larger inner truncation radius leads to a larger disc luminosity and smaller maximal efficiency. Both effects induce a larger accretion rate.

This illustrates, that the lower limit for truncation radius (upper limit for temperature respectively) is a robust limit. One can turn this also other way round: The parameters define the truncated disc with highest possible efficiency which can provide the necessary accretion rate. This rescaling allows to conclude an maximum efficiency of the accretion disc.

# Chapter 6

## Results

The model introduced in [chapter 3](#) was applied to fit the individual SEDs of the objects in our sample characterised in [chapter 4](#). For each object, the final model configuration is presented in this chapter. The continuum spectrum for the best-fit model is shown, together with the corresponding parameters. Specific details for each galaxy are explained in the corresponding section.

### 6.1 NGC 4594

All parameters of the best-fit model are listed in [table 6.1](#). The model spectrum, together with the observed fluxes, are presented in [figure 6.1](#).

The left panel displays the specific flux density (Jy) versus the frequency (Hz). Black dots are the sub-arcsec resolution measurements used for the modelling of the SED. The X-ray data is indicated by the grey squares, taken from [Fabbiano and Juda \(1997\)](#) and [Pellegrini et al. \(2003\)](#); their bars span one order of magnitude. Low angular resolution data is represented by grey spikes.

TABLE 6.1: The parameter values of NGC 4594.

Parameter		Value	Unit	Toggle
$n_{\text{H}}$	hydrogen column density	$1.8 \times 10^{21}$	$\text{cm}^{-2}$	F
$m_{\text{bh}}$	black hole mass	$1 \times 10^9$	$M_{\odot}$	F
$r_{\text{in}}$	inner radius accretion disc	1.1	$r_g$	I
$N_j$	energy normalisation	$6.98 \times 10^{-7}$	$L_{\text{edd}}$	I
$p$	postshock spectral index	2.8		M
$z_{\text{sh}}$	shock distance	277	$r_g$	I
$r_0$	nozzle radius	1.96	$r_g$	I
$h_{\text{rat}}$	nozzle height, $h_0/r_0$	13.2		I
$\theta$	inclination	20	deg.	F
$T_{\text{in}}$	inner edge temperature accretion disc	5500	K	I
$T_e$	preshock Maxwellian temperature	$3.57 \times 10^{11}$	K	I
$d_{\text{kpc}}$	distance	9400	kpc	F
$z_{\text{max}}$	end of jet	19	log (cm)	M
$k$	equipartition value	5.53		I
$r_{\text{out}}$	outer radius accretion disc	2000	$r_g$	M

**Notes.** The final model parameters for NGC 4594. The corresponding model spectrum is presented in [figure 6.1](#). The last column "Toggle" has three different specifier, F (fixed), I (iterated), and M (manually adjusted). This indicates if the value was fixed from the beginning, iterated by ISIS' parameter search or manually adjusted at some step of the procedure (see text). The other model parameters not listed here were fixed, see [section 5.1](#).

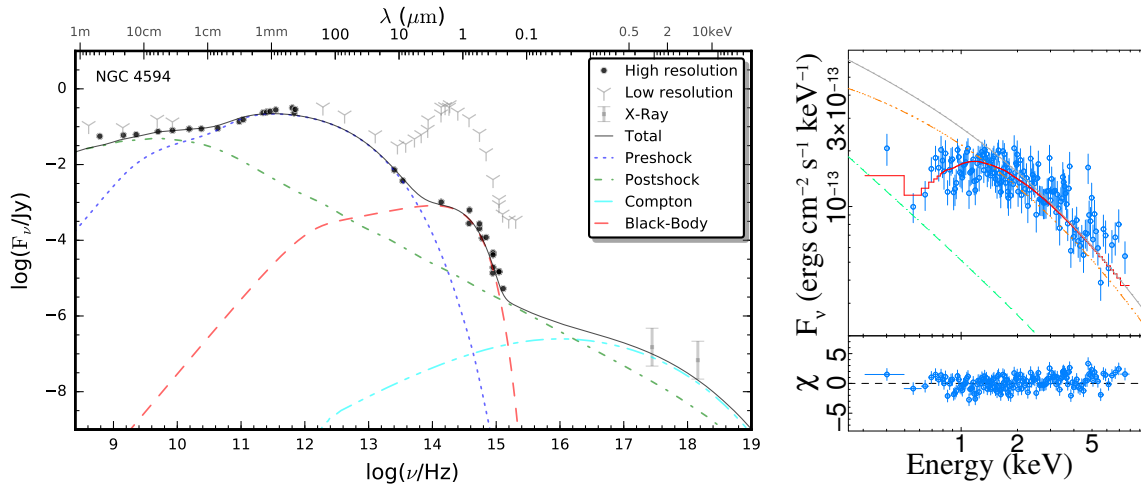


FIGURE 6.1: The model for the SED of NGC 4594. The corresponding parameters can be found in [table 6.1](#). *Left*: Plot in log-log scale shows flux versus frequency. Black dots are the sub-arcsec fluxes used for the modelling. X-ray fluxes from the literature are indicated with grey squares, taken from [Fabbiano and Juda \(1997\)](#) and [Pellegrini et al. \(2003\)](#), their bars span one order of magnitude. Low angular resolution measurements are represented by grey spikes. The coloured lines represent the spectrum of individual model components: the preshock component (dotted blue), the postshock component (dash-dotted green), the Compton component (dash-dash-dotted cyan), the accretion disc (dashed red). Their sum (solid-thin black line) represent the spectrum of the model. *Right*: The X-ray spectrum as seen by *Chandra* in blue. The red line is the model spectrum folded into the detector space. The grey line is the model output in physical units, corresponding to the total model spectrum in the left panel. The panel below shows the residuals. A plot containing the residuals for the left panel can be found in [A.4](#).

The coloured lines represent the spectrum of individual model components: The thermal plasma at the base of the jet radiates synchrotron emission. The spectrum produced is the preshock component, represented by the dotted blue line. Accelerated particles in the jet obey a power law energy distribution. Their synchrotron emission, the postshock component, is shown in dash-dotted green. The energetic particles scatter up photons by the inverse Compton effect, giving rise to the Compton component (dash-dash-dotted cyan). The thermal spectrum of the truncated accretion disc is represented by the dashed red line. The model spectrum, the solid-thin black line, corresponds to the sum of all the components. For details of the model see [section 3.1](#).

The right panel focuses on the X-rays. In blue, the X-ray spectrum is plotted as seen by *Chandra*. The red line is the model spectrum folded into the detector space. The grey line is the model output in physical units, corresponding to the total model spectrum in the left panel. The panel below shows the residuals, i.e. the offset between data (blue dots) and the best-fit model folded in the detector space (red line).

Here follows the detailed description of the determination of the best-fit values presented above. The parameters measured observationally, specifically the hydrogen column density, distance, and black hole mass, were fixed to the value given in [table 4.1](#). The inclination was fixed by an initial guess at  $20^\circ$ . The impact of different inclinations will be discussed below. The distance where acceleration ends, i.e. the end of the jet was set to  $\log(z_{\text{max}} \text{cm}^{-1}) = 19$ .

The spectrum of this nucleus shows a well pronounced peak at  $\sim 1\mu\text{m}$  which was not captured by the pre- or the postshock components of the model. However, this bump is variable and therefore ascribed to the active nucleus ([Fernández-Ontiveros et al. 2012](#)). The thermal-like shape could be described by an accretion disc. Suitable parameters for

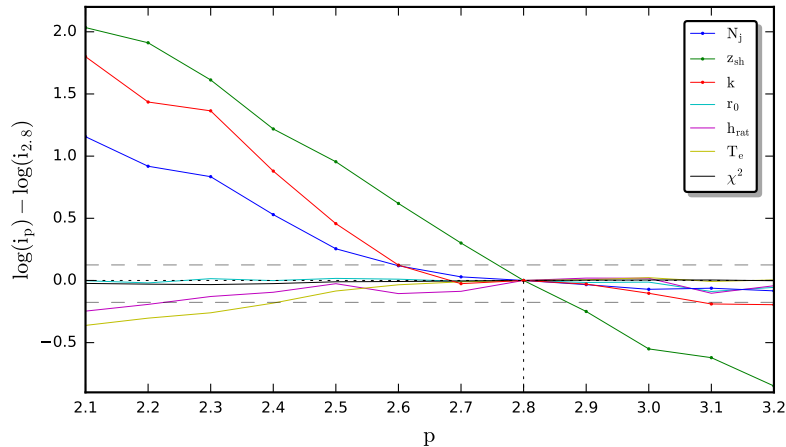


FIGURE 6.2: NGC 4594: parameter changes for different the indices  $p$  of the power law electron distribution in a semi-log plot. Every parameter "i" involved in the iteration, is individually normalised to its value at  $p = 2.8$ , indicated by the intersection of the dotted lines. The dashed horizontal lines show  $2/3$  and  $4/3$ , respectively.

the  $1\mu\text{m}$  peak were searched by including only optical data from IR to UV (shortwards of  $\sim 3\mu\text{m}$ ) and using the inner edge radius and its temperature as free parameters in the iteration. The inner edge radius converged at  $r_{\text{in}} \sim 1.11r_g$  and the temperature at  $T_{\text{in}} \sim 5480$  K. For all subsequent fits, the parameters of the truncated disc were frozen at  $r_{\text{in}} = 1.1r_g$ ,  $T_{\text{in}} = 5500$  K, and  $r_{\text{out}} = 2000r_g$ .

Since the thermal-like bump dominates the UV-fluxes, it did not pose a hard constraint on the postshock component. It was possible to model the X-ray data using solely the postshock component, with different mixtures of both (postshock dominates soft X-rays, Compton hard X-rays), or only the Compton component. In order to investigate appropriate configurations,  $p$  was varied in 0.1 steps in the range  $2.2 - 3.2$ . For each  $p$  the best-fit values were determined for the 6 free parameters ( $N_j$ ,  $z_{\text{sh}}$ ,  $r_0$ ,  $h_{\text{rat}}$ ,  $T_e$  and  $k$ ). The result is shown in figure 6.2.

For all configurations the reduced  $\chi^2$ -value was in the range  $3.8 - 4.2$ . There existed a large number of configurations for different postshock spectral indices resulting in fits of similar quality. However, these degenerate solutions differed strongly - especially in power normalisation  $N_j$  and equipartition  $k$ . From figure 6.2 one can distinguish approximately three groups of parameters. One parameter group underwent only minor changes, their values stayed approximately in the same range for all investigated  $p$ . This group consists out of  $r_0$ ,  $h_{\text{rat}}$  and  $T_e$ , which are the three parameters characterizing the nozzle. The second group consists of  $N_j$  and  $k$ , which showed a strong correlation with  $p$ . Larger values for  $N_j$  implied larger values for  $k$ . While both varied strongly for low values of  $p$ , they seemed to become stable at a certain value above  $p = 2.6$ . The shock distance  $z_{\text{sh}}$  was tightly bound to  $p$  over the full range of values. As visible in figure 6.1, the disc component slightly underestimates the highest frequency UV fluxes. Minimisation of  $\chi^2$  naturally drove the postshock component to fit that data point. While  $p$  sets the slope of the postshock component,  $z_{\text{sh}}$  roughly moves the entire postshock component vertically. Hence the optically thin part of the postshock component effectively "gyrated" around the highest frequency UV flux measurements, resulting in a tight dependence between  $p$  and  $z_{\text{sh}}$ .

The results of these individual plots are briefly discussed now, focusing on the X-ray range. For  $p \lesssim 2.5$  the postshock component dominated the X-ray spectrum. In this case the Compton component is suppressed by high values of  $k$ , which in turn led to an increase

of  $N_j$ , in order to keep the overall radiative output energy at the same level. For  $p = 2.5$  the postshock component was approximately tangential to the Compton component. For  $p > 2.5$  the model's X-ray emission was dominated by the inverse Compton component. Figure 6.2 demonstrates that a value of  $p \gtrsim 2.6$  led to parameter configurations, mostly independent of the actual value of  $p$ .

For  $p = 2.8$  the synchrotron flux contribution to the soft X-rays at 0.5 keV was less than 1/3 of the total model flux. Going even to higher  $p$  led to slightly lower equipartition values and thus lowers the normalisation  $N_j$ . However, this effect was small: Increasing the value for  $p$  from 2.8 to 3.2 resulted in a decrease of  $N_j$  by less than 20 per cent. High power law indices ( $p \gtrsim 3$ ) are not common in LLAGNs since that would imply an extremely fast cooling mechanism (e.g. Markoff et al. 2008). Thus  $p = 2.8$  was chosen as the most representative value for NGC 4594. The reduced  $\chi^2$  value for this configuration is 3.96.

All the best-fit parameters are listed in table 6.1. The model spectrum, together with the observational fluxes, are presented in figure 6.1.

The thermal-like bump is represented by the accretion disc only with no need for the jet in that region. The radio regime is explained by the postshock component, i.e. accelerated particles in the jet. The observational data shows a flat radio spectrum down to cm wavelengths. At that wavelength a bend in the continuum spectrum appears towards the far-IR. This trend is modelled by the preshock component, which dominates the emission in the sub-mm. There, the spectrum of the preshock component has the form of a broad bump, while the low resolution mid-IR data is fairly (factor  $\sim 3$ ) above the predicted flux by the model. In the mid-IR around  $10 \mu\text{m}$  the preshock component is constrained by VLT/VISIR and Gemini/T-ReCS measurements. The X-ray spectrum is mostly represented by SSC of the preshock component.<sup>1</sup> The postshock component contributes less than 1/4 to the X-ray emission at 0.5 keV. A small trend in the residuals at higher energies is visible in the right lower panel. Artificially increasing the electron temperature to avoid that trend is not possible for fixed inclination, since the preshock component is bounded from both sides: radio and IR data constrain its extension and therefore impose lower limits on the curvature in the Compton component.

To investigate the impact of the different possible inclination angles, new models were produced for  $\theta = 5^\circ$  and  $\theta = 90^\circ$ . These values represent approximately the highest and the lowest beaming achievable and therefore the most extreme cases.<sup>2</sup> For  $\theta = 5^\circ$ , the optically thin part of the postshock component became flatter, which resulted in an increase of  $p$  to 3.1, necessary to keep a small X-ray contribution. Besides an increase of the postshock component in radio by a factor of  $\sim 2 - 3$  and a slight decrease in the preshock peak flux no significant spectral changes occurred. To re-adapt the spectrum it was sufficient to decrease  $N_j$  to  $5 \times 10^{-7} L_{\text{edd}}$  and to carry out only minor changes of the other parameters. Interestingly the trend in the X-ray was slightly reduced. The  $20^\circ$ -configuration is considered to be representative for smaller inclinations, too. The same value for  $N_j$  was approximately necessary, to compensate the changes in bolometric luminosity when setting  $k = 1$ . However, the characteristics of the spectrum are not reproduced anymore in that case. The preshock and the Compton components cannot simultaneously model the data. As a result, the value  $N_j = 5 \times 10^{-7} L_{\text{edd}}$  represents the approximate lower limit for the normalisation value necessary to reproduce the spectral shape.

The other extreme is an inclination of  $\theta = 90^\circ$ , corresponding to weakest boosting factor achievable due to beaming effects. In this case, the normalisation was increased to  $\sim 5 \times 10^{-6} L_{\text{edd}}$  to account for the radio fluxes. This value is the approximate upper limit for the normalisation required to reproduce the observed emission. However, this

<sup>1</sup>For this a test was performed to show that switching off the truncated accretion disc had a negligible impact on the X-ray spectrum.

<sup>2</sup>By variation of the inclination,  $\theta \sim 5^\circ$  was visually found to produce the highest radio fluxes.

configuration seems rather unlikely: If a high inclination was real we would expect to see a rather symmetric structure, in contrast with the radio observations by [Hada et al. \(2013\)](#).

As mentioned in [section 4.2](#), the X-ray data set used for modelling differs to other flux density measurements. It shows approximately a factor of 2-3 lower fluxes. In order to investigate the behaviour of the model under variations, the energy normalisation was increased to  $N_j = 1 \times 10^{-6} L_{\text{edd}}$ . That resulted in a higher X-ray flux by a factor of more than 3 and increased the sub-mm flux by approximately a factor of 2.

To check the impact of such changes of the sub-mm fluxes on the determination of the inferred bolometric luminosity, the following exercise was carried out: Changing the flux in the sub-mm of the observational SED by 20 per cent changed the luminosity estimation by roughly 15 per cent. This shows, that this object's bolometric luminosity is dominated by the flux in the sub-mm region.

## 6.2 NGC 1097

The best-fit parameters are listed in [table 6.2](#). The corresponding model is shown in [figure 6.1](#), in the same way as in the previous section (for detailed description, see [section 6.1](#)).

Similar as for NGC4594, distance, black hole mass and hydrogen column density were fixed at their tabulated values (see [table 4.1](#)). As mentioned in [section 4.3](#), the inclination of the jet is loosely constrained by radio observations. [Storchi-Bergmann et al. \(2003\)](#) inferred an inclination of  $34^\circ$  for the accretion disc, which was adopted also by [Nemmen et al. \(2006\)](#). For better comparison with the latter, the same inclination was used here: By the assumption that the jet is ejected perpendicularly to the disc, the inclination was fixed at  $56^\circ$ . By manual variation an intermediate configuration was found, with a nozzle radius converging to  $r_0 \lesssim 1r_g$ . Higher values for  $r_0$  did not fit, because the high angular mm data from ALMA hampered the movement of the preshock component to lower frequencies. The low value for  $r_0$  caused high X-ray model fluxes which in turn drove the equipartition  $k$  towards values high above equipartition, to avoid exceeding the measured fluxes. The

TABLE 6.2: The parameter values of NGC 1097.

Parameter		Value	Unit	Toggle
$n_{\text{H}}$	hydrogen column density	$2.3 \times 10^{20}$	$\text{cm}^{-2}$	F
$m_{\text{bh}}$	black hole mass	$1.4 \times 10^8$	$M_{\odot}$	F
$r_{\text{in}}$	inner radius accretion disc	5	$r_g$	M
$N_j$	nozzle power input	$2.53 \times 10^{-5}$	$L_{\text{edd}}$	I
$p$	postshock spectral index	2.3		M
$z_{\text{sh}}$	shock distance	112	$r_g$	I
$r_0$	nozzle radius	0.80	$r_g$	I
$h_{\text{rat}}$	nozzle height, $h_0/r_0$	3.01		I
$\theta$	inclination	56	deg.	F
$T_{\text{in}}$	inner edge temperature accretion disc	9000	K	I
$T_e$	preshock Maxwellian temperature	$1.70 \times 10^{11}$	K	I
$d_{\text{kpc}}$	distance	14500	kpc	F
$z_{\text{max}}$	end of jet	16.8	lg (cm)	M
$k$	equipartition value	53.3		I
$r_{\text{out}}$	outer radius accretion disc	2000	$r_g$	M

**Notes.** The parameter values of NGC1097. The corresponding model spectrum is plotted in [6.3](#). The last column "Toggle" has three different specifier, F (fixed), I (iterated), and M (manually adjusted). Similar table as for NGC 4594, for more description details see [table 6.1](#).

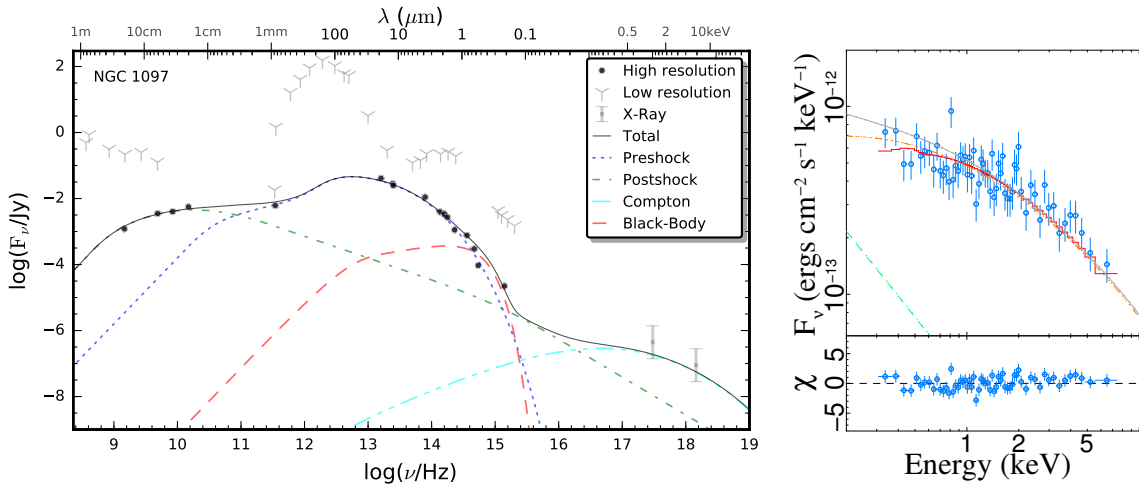


FIGURE 6.3: The model for the SED of NGC 1097. The corresponding parameters can be found in [table 6.2](#). *Left*: Plot in log-log scale shows flux versus frequency. Black dots are the sub-arcsec fluxes used for the modelling. X-ray fluxes from the literature are indicated with grey squares, taken from [Brinkmann et al. \(1994\)](#) and [Nemmen et al. \(2006\)](#), their bars span one order of magnitude. Low angular resolution measurements are represented by grey spikes. The coloured lines represent the spectrum of individual model components: the preshock component (dotted blue), the postshock component (dash-dotted green), the Compton component (dash-dash-dotted cyan), the truncated accretion disc (dashed red). Their sum (solid-thin black line) represent the spectrum of the model. *Right*: The X-ray spectrum as seen by *Chandra* in blue. The red line is the model spectrum folded into detector space. The grey line is the model output in physical units, corresponding to the total model spectrum in the left panel. The panel below shows the residuals. A more detailed description of the figure can be found in [section 6.1](#). A plot containing the residuals for the left panel can be found in [A.4](#).

relatively weak radio emission allowed us to use a small power law index.  $p$  was fixed at 2.3, which resulted in a dominant Compton component in X-rays. The motivation to fix it at that value follows a similar argumentation as in the case of NGC 4594, which is discussed in [section 6.1](#). In the observational SED there can be observed a mutual trend in the 5, 8.4 and 15 GHz observations. This trend is not continued by the 1.4 GHz data. To model that, the end of the jet, i.e. the distance where the acceleration ends, was set to  $\log(z_{\text{max}} \text{cm}^{-1}) = 16.8$ .

Since there is no indication in the SED for an accretion disc, it was not included in the following derivation of the best-fit parameters. The parameter search routine was started:  $N_j, z_{\text{sh}}, r_0, h_{\text{rat}}, T_e$  and  $k$  were iterated simultaneously and their best-fit values were determined as described in [section 5.2](#). The final reduced  $\chi^2$  value was 4.03. Then, the accretion disc was modified to the data by setting  $r_{\text{in}} = 5r_g$  and adopting the temperature to 9000 K.

The model is shown the same way as in the previous section. For detailed description, see [section 6.1](#). The radio data is represented by the jet (postshock component). Towards low frequencies a bend downward is present, marking the transition from the flat spectrum (superposition of self absorbed components) to the optically thick regime of the rearmost component, at the end of the jet. The postshock component is flat up to approximately the 15 GHz flux, where its turnover from optically thick to thin takes place. Towards higher frequencies the preshock component becomes dominant. The total spectrum is remarkably flat in this entire region. The spectrum is only very sparsely sampled in sub cm-wavelengths: the single measurement by ALMA is the only high angular resolution flux over approximately 3 orders of magnitude in frequency. However, the spectral characteristic is strongly dictated by this measurement. Towards higher frequencies the preshock

component bends up to its peak at approximately  $50 \mu\text{m}$ . From far-IR to the UV the entire emission is dominated by the preshock component. The UV data does not show any signature of an accretion disc, but it imposes limits on its maximum flux. X-ray emission is dominated by the Compton component, without showing a trend. The contribution of optically thin synchrotron emission is negligible.

In contrast to Sombrero, there is no clear signature in the data for the accretion disc. Therefore the inner edge temperature is unconstrained. It is possible to change the position of the peak of the disc by varying both, inner edge temperature and radius, as long as it does not contradict the data. This is described in detail in [section 5.4](#). A truncation radius of  $450r_g$  as proposed by ([Nemmen et al. 2006](#)), required an inner edge temperature of at maximum  $\sim 1500 \text{ K}$ .

Some parameters of the configuration show rather unusual values. For instance, the nozzle radius is very small, and the equipartition value is very large. In order to investigate the impact of possible variations, the following two attempts were carried out: The equipartition was limited to a value of  $k = 8$ , and the iteration executed. For that case, the code found a compromise with  $N_j \sim 9.7 \times 10^{-6} L_{\text{edd}}$ , corresponding to  $\sim 0.4$  of the best-fit value. For this "low" equipartition the following spectral changes occurred: The radio emission was slightly underestimated; the model flux overshoot the mm-data by a factor of 2, in the IR at  $10 \mu\text{m}$  the model flux was a factor of 2 too low. Going closer to equipartition these offsets became even worse.

For the second test we fixed equipartition at 1.01, and adapted the fluxes at radio and X-rays. That configuration had an energy normalisation of  $N_j \sim 7 \times 10^{-6} L_{\text{edd}}$ . This model (see [7.3](#)) showed in these both regions a similarly good fit as the final result, while the predicted flux in e.g. the UV was found below by a factor of approximately 5.

### 6.3 NGC 1052

The best-fit parameters are listed in [table 6.3](#). The corresponding model is shown in [figure 6.4](#), in the same way as in the previous section (for detailed description, see [section 6.1](#)).

The parameters measured observationally, specifically the distance and the black hole mass were fixed to their values given in [table 4.1](#). An inclination of  $80^\circ$  was adopted, as suggested by high frequency measurements (see [section 4.4](#)). The hydrogen column density enters modelling as a free additional parameter.

The power law index was fixed at  $p = 3.0$  (motivation see [section 6.1](#)). Interestingly, in contrast to the other two objects investigated before, the UV fluxes are imposing lower bounds for  $p$ , instead of the X-rays spectrum. This made it very hard to model the hard X-ray with the optically thin postshock spectrum. Furthermore, the flat spectrum would need a power law index which is fairly below 2. The end of acceleration was set to  $\log(z_{\text{max}} \text{ cm}^{-1}) = 19.5$ .

By manual variation a intermediate configuration was found. The high radio fluxes turned out to be difficult to be represented by the model, especially for that high inclination. The flat X-ray spectrum and the steep decrease of the observed continuum fluxes from mid-IR to near-IR induced a very large nozzle radius ( $r_0 \gtrsim 50r_g$ ) and a very large electron temperature ( $T_e \gtrsim 7 \times 10^{11} \text{ K}$ ). Similar as for NGC 1097, the accretion disc component did not enter in the following parameter search. The iterative variation resulted in a steadily decreasing equipartition value below 0.1 without finding convergence and without improving the fit significantly.<sup>3</sup> Thus the equipartition parameter was fixed at  $k = 0.9$ . Then the automatic iteration was repeated varying  $n_{\text{H}}$ ,  $N_j$ ,  $r_0$ ,  $h_{\text{rat}}$ ,  $T_e$ , and  $z_{\text{sh}}$

<sup>3</sup>Furthermore it produced unstable runs with system freezes - increasing the available memory (swap partition) solved this issue.

TABLE 6.3: The parameter values of NGC 1052.

Parameter		Value	Unit	Toggle
$n_{\text{H}}$	hydrogen column density	$9.01 \times 10^{22}$	$\text{cm}^{-2}$	I
$m_{\text{bh}}$	black hole mass	$1.54 \times 10^8$	$M_{\odot}$	F
$r_{\text{in}}$	inner radius accretion disc	5	$r_g$	M
$N_j$	energy normalisation	$1.87 \times 10^{-4}$	$L_{\text{edd}}$	I
$p$	postshock spectral index	3		M
$z_{\text{sh}}$	shock distance	5532	$r_g$	I
$r_0$	nozzle radius	68.4	$r_g$	I
$h_{\text{rat}}$	nozzle height, $h_0/r_0$	0.64		I
$\theta$	inclination	80	deg.	F
$T_{\text{in}}$	inner edge temperature accretion disc	9000	K	M
$T_e$	preshock Maxwellian temperature	$7.62 \times 10^{11}$	K	I
$d_{\text{kpc}}$	distance	18000	kpc	F
$z_{\text{max}}$	end of jet	19.5	lg (cm)	M
$k$	equipartition value	0.9		F
$r_{\text{out}}$	outer radius accretion disc	2000	$r_g$	M

**Notes.** The corresponding model spectrum is plotted in [figure 6.4](#). Final reduced  $\chi^2$  amounts to 8.94. Similar table as for NGC 4594, for more description details see [table 6.1](#).

as described in [section 5.2](#). The confidence interval search did not converge, but the parameters stabilised and showed an acceptable result. Then the inner truncation radius of the accretion disc was set to  $r_{\text{in}} = 5r_g$  and its edge temperature to  $T_{\text{in}} = 9000$  K. The resulting parameters are listed in [6.3](#), final reduced  $\chi^2 = 8.94$ . The final model spectrum is shown in [6.4](#), for detailed description of the plot see [section 6.1](#).

Beginning with the X-rays it is interesting to note that the *Nustar* dataset shows indication of a weak, relativistically broadened iron  $K\alpha$  line. The whole X-ray region is reproduced entirely by the Compton component. In the UV, the preshock component slightly underestimates the flux at highest frequency. A small contribution by the optically thin postshock component reduces the deviation (similar as for NGC 4594, [section 7.1](#)). Towards the IR, at first the preshock component slightly overestimates the fluxes, but subsequently bends and underestimates the flux measurements. These low angular resolution flux measurements is considered to represent the nucleus and was included in the iteration (details see [section 4.4](#)). The very broad bump of the preshock component accounts for the entire emission in the IR and reaches down to GHz frequencies. There, the base of the jet becomes self absorbed and the postshock component starts to dominate. Interestingly the same spectral behaviour is observed: in the plot the isolated core emission is represented by grey diamonds in [figure 6.4](#). The high emission in the radio, especially the peak at cm-wavelengths ( $\sim 5$  GHz), is not reproduced. The predicted radio fluxes are up to one order lower than the measured fluxes. Looking at the full picture: Without considering the deviations in the extended radio emission of the jet, i.e. by only taking the true core emission into account (grey diamonds), the preshock and Compton components can entirely reproduce the continuum emission.

In order to investigate the discrepancy in the radio range, the final configuration was tested for lower inclinations. The aim was not to reproduce the 5 GHz bump, but to reproduce the flux level at lower frequencies. The iteration before which produced the best-fit model tried to recover the measured fluxes, but did not reach the flux level of the radio measurements. Therefore the best-fit configuration shows the highest radio fluxes compatible with the rest of the SED. For that configuration higher radio fluxes can only be obtained

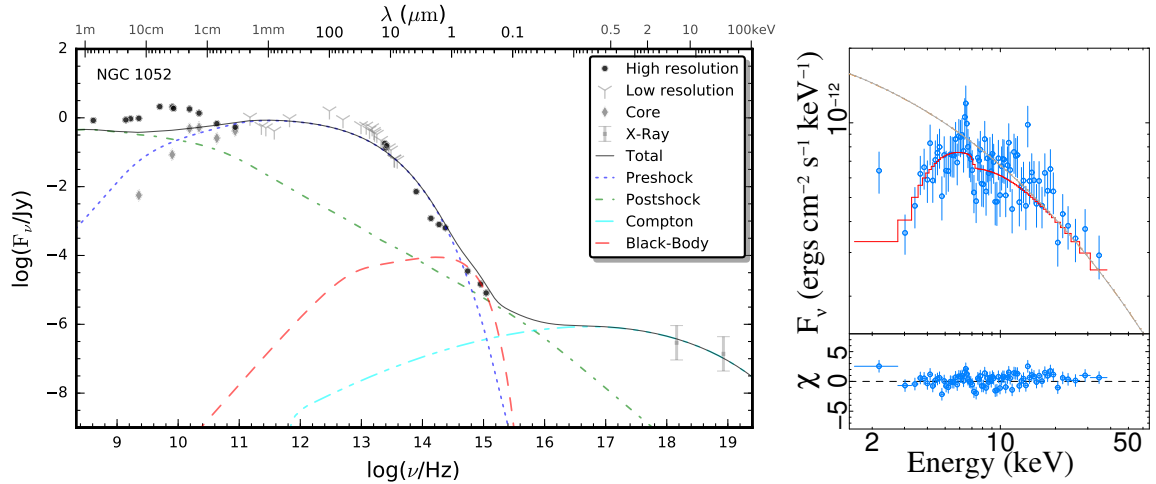


FIGURE 6.4: The model for the SED of NGC 1052. The corresponding parameters can be found in [table 6.3](#). *Left*: Plot in log-log scale shows flux versus frequency. Black dots are the sub-arcsec fluxes used for the modelling. X-ray fluxes from the literature are indicated with grey squares, taken from [Ueda et al. \(2001\)](#) and [Ajello et al. \(2009\)](#), their bars span one order of magnitude. Low angular resolution measurements are represented by grey spikes. Grey diamonds display the measured core emission. They represent lower limits, especially towards lower frequencies due to free-free absorption (see [section A.3](#)) in front of the core (see [section 4.4](#)). The coloured lines represent the spectrum of individual model components, the preshock component (dotted blue), the postshock component (dash-dotted green), the Compton component (dash-dash-dotted cyan), and the truncated accretion disc (dashed red). Their sum (solid-thin black line) represents the spectrum of the model. *Right*: The X-ray spectrum as seen by *Nustar* in blue. The red line is the model spectrum folded into detector space. The grey line is the model output in physical units, corresponding to the total model spectrum in the left panel. The panel below shows the residuals. A more detailed description of the figure can be found in [section 6.1](#). A plot containing the residuals for the left panel can be found in [section A.4](#).

for smaller inclination. Turning the model to an inclination of  $\lesssim 55^\circ$  was necessary to raise the radio fluxes to the mutual level of the data.

The spectral shape of the preshock component hampered to reproduce the bend at approximately  $20 \mu\text{m}$ . In contrast, the choice of the power law distribution allowed to reproduce the spectrum similarly well, especially that bend came out naturally. However, the steep slope from that region to the UV required a power law index of  $p \gtrsim 6$ , which is unlikely (e.g. [Markoff et al. 2008](#)).



# Chapter 7

## Discussion

This chapter discusses the results of [chapter 6](#), for every object individually in one section. This includes testing consistency to observational measurements, highlighting specialities, comparing the model results with complementary observations or other models, and estimating the energetic budget with focus on the jet rest frame luminosity and on the accretion disc. In [section 7.4](#) the parameters of the sample are compared to previous works. The advantage of high angular resolution at all frequencies is highlighted. Thereafter results of this work regarding accretion discs in general is briefly summed up.

### 7.1 NGC 4594

#### 7.1.1 Model Consistency

The luminosity of the model SED from radio to UV results in  $L_{R-UV} = 1.65 \times 10^{41} \text{ erg s}^{-1}$ , which accounts for 36 per cent of the observational SED (see [table 7.1](#)). In [section 6.1](#) the sensitivity of the luminosity on the fluxes of the sub-mm region is shown: most of the radiative spectral energy is received at that wavelengths. First, simple linear interpolation from sub-mm down to the mid-IR of the observational SED, and second, flux deviations of roughly a factor 2 between the observed and the modelled fluxes in that sensitive region can largely change the inferred luminosity. These effects lead for this object to that large differences. For further energetic considerations the model bolometric luminosity will be used. A general remark at this point is, that the bolometric luminosity estimation of objects with rather peaked SEDs might be quite uncertain. For sparsely sampled SEDs a multiple broken power law connecting adjacent observational data is expected to give more representative values for the continuum luminosity.

The considerations above are independent of the X-ray luminosities, since their value is less than 10 per cent of the radio-UV luminosity. The deviations of the X-ray luminosities between the model and [Pellegrini et al. \(2003\)](#) (see [table 7.1](#)) can be explained by different effects: First, the source might be variable up to a factor 2-3. This conclusion comes from the comparison of values published and the X-ray spectrum used here. Second, a small trend in the residuals ([figure 6.1](#)) of the X-ray model towards higher energies causes lower values, amplifying the deviations. However, this effect is less dominant than the variability introduced by the usage of data from different epochs. In [section 6.1](#) it was found, that in order to mimic that level of X-ray variability of approximately a factor 3, it is sufficient to increase the energy normalisation by less than 50 per cent.

Summing up the tests carried out in [section 6.1](#), in detail impact of variation of inclination and power law index show, that the resulting scatter of the values for the energy normalisation are all in accordance with variability estimations here. Especially the approximate lower bound turns out to be quite robust,  $N_j \gtrsim 5 \times 10^{-7} L_{\text{edd}}$ .

TABLE 7.1: Luminosities NGC 4594

	$L_{R-UV}$ [erg s <sup>-1</sup> ] (1)	$L_{0.5-2 \text{ keV}}$ [erg s <sup>-1</sup> ] (2)	$L_{2-10 \text{ keV}}$ [erg s <sup>-1</sup> ] (3)	Ref. (4)
Observations	$4.58 \times 10^{41}$	$5.7 \times 10^{39}$	$1.4 \times 10^{40}$	a, b
Model	$1.65 \times 10^{41}$	$3.78 \times 10^{39}$	$5.13 \times 10^{39}$	a

**Notes.** (1) Integrated luminosity from radio to UV of the observational SED, and the model output spectrum; (2) Soft X-ray luminosity; (3) Hard X-ray luminosity; (4) References: (a) this work (b) [Pellegrini et al. \(2003\)](#).

### 7.1.2 Jet and Accretion Disc

Focusing solely on the energetics of the jet, we want to estimate upper and lower limits for the rest frame luminosity  $L_{RF}$ . For the model inclination of  $20^\circ$  the model integrated jet luminosity is  $L_j \sim 1.49 \times 10^{41} \text{ erg s}^{-1}$ . [Hada et al. \(2013\)](#) estimated the jet bulk velocities to be highly sub-relativistic,  $\beta \lesssim 0.2 c$ , and a spectral index of  $\alpha \sim 1.1$ . We assume a continuous jet,  $F_\nu \sim \delta^{2+\alpha} F'_\nu$ , where the relativistic Doppler factor is  $\delta = 1/[\gamma(1 - \beta \cos \theta)]$  (see [A.2.4](#)). From these quantities we estimate the lower and the upper limit for the boosting factor:

$$1 \lesssim b \lesssim 1.79 \quad (7.1.2.1)$$

Therefore the rest frame luminosity is bound from below by  $L_j/1.79 \lesssim L_{RF}$ .

$$0.83 \times 10^{41} \text{ erg s}^{-1} \sim L_{RF} \lesssim L_j \sim 1.49 \times 10^{41} \text{ erg s}^{-1} \quad (7.1.2.2)$$

NGC 4594 is the only object in the sample which shows a thermal-like bump in the IR. The bump can be represented by a truncated accretion disc with an inner edge temperature of  $T_{in} \sim 5500 \text{ K}$ . For the black hole mass and inclination adopted in the final configuration (see [6.1](#)) the result was an inner radius of  $r_{in} \sim 1.1 r_g$ . The model integrated (isotropic) luminosity of the thermal component is  $3.24 \times 10^{40} \text{ erg s}^{-1}$ . Correcting that for an inclined Lambertian surface results in a disc luminosity<sup>1</sup>  $L_{disc} \sim 1.71 \times 10^{40} \text{ erg s}^{-1}$ .

Assuming a disc efficiency of  $\eta = 0.1$ , the inferred accretion rate is then  $\dot{M} \sim 3.0 \times 10^{-6} M_\odot \text{ yr}^{-1}$ . If we assume as an upper limit, that all the matter entering the inner region is available to power the jet in form of energy, the maximum power provided by the disc is  $L_{disc}^{10\%}/0.1 \sim 1.71 \times 10^{41} \text{ erg s}^{-1}$ . Here we neglect, that effectively the maximum power is below the value above, as the accreted mass presumably has radiated away 10 per cent of its rest mass. Under the assumptions above, the accretion disc supplies enough mass-flow, to account for the model rest frame luminosity. However, the accreted mass would be more than 5 times too less to meet the approximate jet power requirement  $P_j \sim 10 N_j \sim 8.78 \times 10^{41} \text{ erg s}^{-1}$ .

### 7.1.3 A Smaller Black Hole?

The unusual values for the disc parameter, in detail the low temperature, together with an inner radius extending close to the inner most circular stable orbit of a maximally rotating black hole, are an unlikely configuration. Furthermore, for that small inner radius the efficiency in mass to light conversion of the disc is expected to exceed the above assumed 10

<sup>1</sup>It was checked that the outer edge radius of the model's truncated accretion disc has a negligible impact on its integrated bolometric luminosity: the change of the outer edge from  $2000 r_g$  to  $200 r_g$  resulted in a decrease of the luminosity by less than 1 percent.

TABLE 7.2: Model Energetics NGC 4594

$P_j$ [erg s <sup>-1</sup> ] (1)	$L_j$ [erg s <sup>-1</sup> ] (2)	$L_{\text{disc}}$ [erg s <sup>-1</sup> ] (3)	$L_{\text{RF}}$ [erg s <sup>-1</sup> ] (4)
$8.78 \times 10^{41}$	$1.49 \sim 10^{41}$	$1.71 \times 10^{40}$	$(0.83 - 1.49) \times 10^{41}$

**Notes.** (1) Approximate model jet power requirement,  $10N_j$ ; (2) Model jet luminosity; (3) Accretion disc luminosity; (4) Rest frame energy range, constraint by limits of weakest and strongest beaming.

per cent. This would increase the discrepancy between approximate jet power requirement  $P_j$  and accretion power. Similarly the rest frame luminosity could exceed the provided accretion power. Additionally the nozzle radius inferred from modelling is  $r_0 \lesssim 2r_g$ . All these things could be interpreted as indications of a smaller black hole mass. A lower mass would decrease the scale radius and therefore increase the nozzle radius and the inner radius of the accretion disc. A larger inner radius would cause a reduced disc efficiency, and in turn provide a higher maximum accretion power, available to feed the jet.

## 7.2 NGC 1097

### 7.2.1 Model Consistency

The luminosity of the model SED from radio to UV is  $6.56 \times 10^{41}$  erg s<sup>-1</sup>, which differs by less than 2% when compared to the luminosity of the observational SED (see [table 7.3](#)). The best-fit Model soft and hard X-ray luminosities are  $1.76 \times 10^{40}$  erg s<sup>-1</sup> and  $3.20 \times 10^{40}$  erg s<sup>-1</sup>, respectively. They account for  $\sim 70\%$  of the values found by [Nemmen et al. \(2006\)](#). Taken these three model values together they sum up to  $7 \times 10^{41}$  erg s<sup>-1</sup>. If integrating the total model grid (including the UV to X-ray gap and the 10-100 keV luminosity) this value increases to  $7.47 \times 10^{41}$  erg s<sup>-1</sup>. [Nemmen et al. \(2006\)](#) find  $8.6 \times 10^{41}$  erg s<sup>-1</sup>. Summing that up, the model values are very close to observational data. Only in the X-rays occur small differences, but these are rather attributed to the datasets, because the model does not show an offset or trend in the X-ray residuals (see [figure 6.3](#)). Comparing the model results with the findings of [Nemmen et al. \(2006\)](#), the luminosities agree strongly with each other.

### 7.2.2 A Highly Magnetised Outflow

The best-fit model equipartition value is highly above equipartition  $k > 50$ . By assigning a large fraction of the input energy to magnetic energy, less energy is available for particles. The particle number is small and in turn the jet carries relatively little kinetic energy. This is one possible explanation for the weak jets. Further evidence for low kinetic power is the short length of the jet: Its extension on radio maps is only of parsec scale ([Mezcua and Prieto 2014](#)). Spectrally, the model predicts a distance of  $\sim 2$  pc, where distributed acceleration ends. Even though this should not be treated as a robust estimation of the length of the jet, it is interesting to note that this value is in approximate agreement with the projected length evident from radio observations. Kinetically weak jets are expected to be influenced strongly by their environment.

Having a second glance at [table 6.2](#), another unusual parameter is present: The nozzle radius is very small,  $r_0 < 1r_g$ . This arises mainly from the limits of the IR-UV continuum

TABLE 7.3: Luminosities NGC 1097

	$L_{R-UV}$ [erg s <sup>-1</sup> ] (1)	$L_{0.5-2 \text{ keV}}$ [erg s <sup>-1</sup> ] (2)	$L_{2-10 \text{ keV}}$ [erg s <sup>-1</sup> ] (3)	Ref. (4)
Observations	$6.45 \times 10^{41}$	$2.5 \times 10^{40}$	$4.4 \times 10^{40}$	a,b
Model	$6.56 \times 10^{41}$	$1.76 \times 10^{40}$	$3.20 \times 10^{40}$	a

**Notes.** (1) Integrated luminosity from radio to UV of the observational SED, and the model output spectrum; (2) Soft X-ray luminosity; (3) Hard X-ray luminosity; (4) References: (a) this work (b) [Nemmen et al. \(2006\)](#).

and especially from mm-wavelength measurements, which "push" the preshock component to a relatively high frequency. These low mm-wavelength flux level measured by [Izumi et al. \(2013\)](#) are confirmed by [Izumi et al. \(2017\)](#). Indeed, the flux seems to be on average even lower, and additionally shows high variability (see [section 4.3](#)). This high variability requires a high contemporaneity of the data. Since the mm data and the X-rays are from different epochs, caution with the interpretation is necessary. In order to put more weight on the parameters obtained here, a denser and contemporary sampling of that spectral region, together with X-ray observations is necessary. However, independent of this variability, the generally low flux level at that region drives the model to a small nozzle size. By the assumption, to have a nozzle radius, whose value lies in the range of previous findings ( $\sim 2r_g - 10r_g$ , see e.g. [van Oers et al. 2017](#)), one could infer a smaller black hole mass of a factor of approximately 5-10. This speculation bases on the assumption, that the nozzle volume is of the same order in size for all objects.

Physically, the small nozzle radius further enhances the magnetic energy density in the nozzle: it is small in size and magnetically dominated. Within this region an energetic plasma is confined and dominating the entire IR emission. If this model prediction is true, it raises the question of the origin of this unusual compression and the strong magnetic fields. According to [Storchi-Bergmann et al. \(2003\)](#), the accretion disc is truncated fairly outside ( $r_{in} \sim 450r_g$ ). It seems unlikely, that the magnetic fields close to the black hole are produced by material at this large distance by amplification of the magnetic field. It could be speculated, that rather winding up the magnetic field within the ergosphere plays the dominant role, in which case the black hole would necessarily spin quickly. That in turn would increase the efficiency of the extraction of rotational energy by the Blandford-Znajek mechanism ([Blandford and Znajek 1977](#), see [subsection 1.3.2](#)). This LLAGN could represent an object, whose strong magnetic fields are a direct result of a quickly spinning black hole. The ratio of leptons to protons might also be quite high, since pair production is more efficient for higher densities of particle, photon and field energies, further expected to produce a rather weak jet. If the black hole spins quickly and the accretion rate is small, the extraction rate exceeds the advection rate of rotational energy - resulting in a de-acceleration. This object is highly interesting and further investigation of highest angular resolution imaging at higher radio frequencies are necessary, to reject or strengthen this conjecture.

### 7.2.3 Jet and Accretion Disc

The model jet luminosity is  $L_j = 6.91 \times 10^{41} \text{ erg s}^{-1}$ . The approximate total jet power requirement,  $P_j \sim 4.46 \times 10^{42} \text{ erg s}^{-1}$ , is enough to supply the observed jet emission. The alignment of the jet with the line of sight is unconstrained for this object. Therefore we estimate the rest frame luminosity by integrating the model jet luminosity for  $90^\circ$ , and for the the inclination of strongest boost factor due to effects of beaming. Setting the model to  $90^\circ$

TABLE 7.4: Model Energetics NGC 1097

$P_j$ [erg s <sup>-1</sup> ] (1)	$L_j$ [erg s <sup>-1</sup> ] (2)	$L_{\text{disc}}$ [erg s <sup>-1</sup> ] (3)	$L_{\text{RF}}$ [erg s <sup>-1</sup> ] (4)
$4.46 \times 10^{42}$	$6.91 \times 10^{41}$	$4.99 \times 10^{40}$	$(5.19 - 36) \times 10^{41}$

**Notes.** (1) Approximate model jet power requirement,  $10N_j$ ; (2) Model jet luminosity; (3) Accretion disc luminosity; (4) Rest frame energy range, constraint by limits of weakest and strongest beaming.

inclination, to obtain the smallest possible boosting factor, the spectral changes are small: the  $\chi^2$  value doubles to  $\sim 8.6$ . The overall flux level decreases by less than a factor of 2, only the radio fluxes decrease by at least a factor of 3. This small impact is also evident from the value for the model jet luminosity, which is reduced by less than 25%,  $L_{90^\circ} = 5.19 \times 10^{41}$  erg s<sup>-1</sup>. To find the angle of strongest beaming, the inclination was lowered progressively. For  $\theta = 2^\circ$  occurred the highest model jet luminosity. For inclinations smaller than  $2^\circ$  the jet luminosity slightly decreases, which is not expected from the Doppler factor. This could be explained by two possible effects. The jet is not entirely optically thin: When the jet is pointing directly towards the observer, absorption of closer and colder jet components diminishes the flux arriving at the observer. Especially the self absorbed emission of hotter components will be affected. The magnetic field lines are on average pointing directly towards us, parallel to the direction of bulk motion. Even though aberration aligns the beaming cones closer along the direction, the peak of the emission pattern of individual electrons is not completely aligned. Strongest beaming occurs at  $2^\circ$  for this configuration,  $L_{2^\circ} = 3.60 \times 10^{42}$  erg s<sup>-1</sup>. Here is noted, that this value is affected by the low slope of the power law index  $p = 2.3$  of the electrons.<sup>2</sup> These values strictly embrace the model rest frame luminosity ( $L_{90^\circ} < L_{\text{RF}} < L_{2^\circ}$ ):

$$5.19 \times 10^{41} \text{ erg s}^{-1} < L_{\text{RF}} < 3.60 \times 10^{42} \text{ erg s}^{-1} \quad (7.2.3.1)$$

The typical accretion disc is constrained by the upper limit set by the SED. The accretion disc has an inner truncation radius of  $r_{\text{in}} = 5r_g$  and a corresponding maximum inner edge temperature of 9000 K, imposed by the VIS-UV data. The for inclination corrected disc luminosity inferred by these values is  $L_{\text{disc}} = 4.99 \times 10^{40}$  erg s<sup>-1</sup>. Assuming an efficiency of mass to light conversion of  $\eta = 0.1$ , the accretion rate is  $\dot{M} \sim 8.8 \times 10^{-6} M_\odot \text{ yr}^{-1}$ . Assuming as for NGC 4594, that simply all the accreted matter is entirely converted into available energy, the maximum power provided by the disc is  $L_{\text{disc}}/0.1 = 4.99 \times 10^{41}$  erg s<sup>-1</sup>. This power is slightly smaller than the estimated lower limit of the jet rest frame luminosity  $L_{90^\circ}$ . The accretion power of the disc is not large enough to provide the power necessary to explain the lower limit of the rest frame luminosity of the jet, and is approximately one order smaller than the approximate jet power requirement  $P_j$ . If the real bulk velocities of the jet are higher than the of the model, beaming would be stronger and weaken the limits of the model inferred rest frame luminosity. Therefore these limits must be treated with caution.

## 7.2.4 Modelling the Spectrum I - Inflow or Outflow

In the present work NGC 1097's continuum spectrum is modelled by a compact jet. Before the detection of extended radio emission by [Mezcua and Prieto \(2014\)](#), [Nemmen et al.](#)

<sup>2</sup>For a power law index of  $p = 2.8$  this value would reduce to  $\sim 1.36 \times 10^{42}$  erg s<sup>-1</sup>.

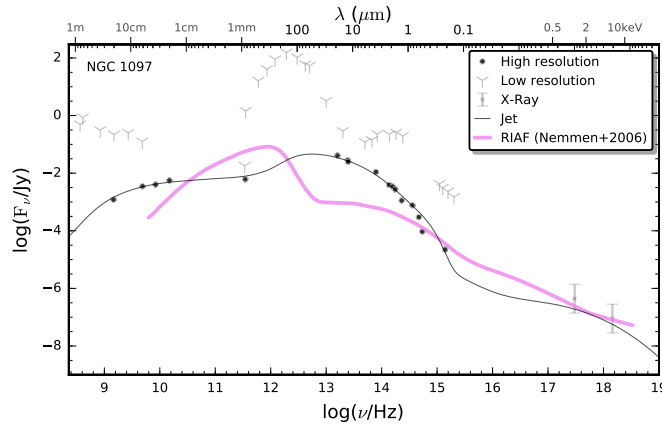


FIGURE 7.1: RIAF and jet model continuum emission. The black line represents the total jet emission, i.e. the sum of preshock, postshock, and Compton component from the best-fit model. The violet line displays the RIAF continuum emission, intended to model the continuum emission with focus on the X-rays and UV (adopted from Nemmen et al. 2006).

(2006) explained the continuum emission with a model, which consisted of an inner radiatively inefficient accretion flow (RIAF) and an truncated thin disc. This section aims to compare their inflow model with the outflow model adopted here. The model used here is described in section 3.1, their model is briefly described below.

In detail, their model consisted of an truncated accretion disc and a RIAF, which should reproduce both the  $H\alpha$  line profiles previously investigated by Storchi-Bergmann et al. (2003) and the continuum emission. Furthermore the RIAF would be origin of the X-ray emission, providing illumination of the disc to explain the strong  $H\alpha$  emission. The transition from disc to RIAF was set to take place at the transition radius  $450 r_g$ . They used the same distance and inclination as adopted here and a black hole mass of  $1.2 \times 10^8 M_\odot$ .

In figure 7.1 both spectra are displayed. It shows X-ray, high, and low angular resolution data as in previous figures. The black line represents the total jet emission, i.e. the sum of preshock, postshock, and Compton component. The violet line displays the RIAF continuum emission. It is noted, that the RIAF is not intended to model the radio region, and neither to represent the near-IR.

A few notes are given, while focusing from X-rays towards lower frequencies: Both models represent X-ray and UV emission similarly well. The original purpose of the isolated RIAF spectrum was to model that frequency range. While the near-IR to mid-IR trend is smoothly represented by the jet model, an accretion disc spectrum (not shown in figure 7.1) is an essential part for the RIAF model to cover that fluxes. However, the thermal shape of the disc spectrum can not represent the near-IR to mid-IR, which follows approximately a power law (see section 6.2). Partly because of that, and their lower resolution in the VIS-UV, they added a spectrum of a young star-burst population to represent this region. At mm-wavelengths the RIAF overpredicts the flux by one order of magnitude. These mm-wavelength data were not available for Nemmen et al. (2006) at that time. In the radio, the RIAF needs the support of a jet (not shown in figure 7.1), to explain the flat radio spectrum.

The RIAF must be complemented by two more additional components to represent the continuum emission (neglecting the star-burst). They incorporate a parametric description of a jet assuming a parabolic continuum shape, and introduce by doing this a new set of parameters - which adds up more complexity to the typically degenerate accretion flow models. The jet model used in this work can explain the nuclear continuum emission over the entire sampled frequency range, in this case even without an accretion disc component.

The striking advantage of complex jet plus disc models as the one in this work is that it can capture most of the complexity shown by the SEDs of LLAGNs, without the need to incorporate additional components.

## 7.3 NGC 1052

### 7.3.1 Model Consistency

The R-UV luminosity of the model is  $L_{\text{model}} = 3.97 \times 10^{42} \text{ erg s}^{-1}$ , corresponding to 57% of the observed luminosity. The underestimation is attributed to the apparent differences at around 10 to 100  $\mu\text{m}$ , where the model predicts slightly lower fluxes.

The soft, hard, and hard X-ray luminosities of the model are  $L_{0.5-2\text{keV}} = 9.54 \times 10^{40} \text{ erg s}^{-1}$  and  $L_{2-10\text{keV}} = 2.97 \times 10^{41} \text{ erg s}^{-1}$ , respectively. The hydrogen column density converged at  $n_{\text{H}} = 8.63 \times 10^{22} \text{ cm}^{-2}$ . For comparison, [Hernández-García et al. \(2014\)](#) found a soft X-ray luminosity of  $L_{0.5-2\text{keV}} \sim 2 \times 10^{40} \text{ erg s}^{-1}$  and hard X-ray luminosity of  $L_{2-10\text{keV}} \sim 2 \times 10^{41} \text{ erg s}^{-1}$ , with a hydrogen column density of  $n_{\text{H}} = 6.11 \times 10^{22} \text{ cm}^{-2}$ . The higher soft X-ray luminosity obtained here might be partly attributed to the slightly higher hydrogen column density ( $n_{\text{H}} = 9.01 \times 10^{22} \text{ cm}^{-2}$ ), while the model's hard X-ray luminosity inferred here is less than 50% higher. On the other hand [Beckmann et al. \(2009\)](#) found an hard X-ray luminosity of  $\sim 3.9 \times 10^{41} \text{ erg s}^{-1}$ , which is  $\sim 1/3$  higher than the model value.<sup>3</sup> The model result for the hard X-ray luminosity lies within the range of literature values. Interestingly the hydrogen column density derived here is agreement with the value of [Connolly et al. \(2016\)](#),  $n_{\text{H}} = 8.6 \times 10^{22} \text{ cm}^{-2}$ . It is noted, that for this object the availability of high X-ray energies constrains the X-ray spectrum slope of the model and therefore allows to constrain  $n_{\text{H}}$  from the modelling. When only soft X-ray datasets are available,  $n_{\text{H}}$  has a higher degeneracy with other model dependent parameters.

### 7.3.2 Magnetic Launch from a Huge Base?

It was not possible to derive confidence intervals for the parameters, which implies, that the  $\chi^2$  minimum is not absolutely robust. The parameters are likely to react sensitively on changes, e.g. if including further observational data in the future. Hence the interpretation of the best-fit parameter values must be carried out carefully. However, neither the model jet luminosity is expected to be influenced significantly, since the  $\chi^2$  minimisation tries to represent the measured fluxes, nor the energy normalisation could be lowered significantly, since the here discussed best-fit model is close to equipartition.

The failure of determining confidence intervals might similarly be a symptom as the deviations in the radio regime: The model is not capable of explaining the strong radio emission entirely. Lowering the inclination below the imposed limits of [Baczko et al. \(2016\)](#) would be necessary to address the strong radio emission by effects of beaming. Therefore the lack of radio emission is not induced by a parameter setting, but due to a physical difference between the model and the jet of NGC 1052.

Interestingly the strong deviations between model and observational data occur only below a certain frequency ( $\sim 30 \text{ GHz}$ ) and can be attributed to the postshock component in the model. In [figure 6.4](#) one can see, that the predicted fluxes of the preshock component agree with the lower limits of measured core emission.<sup>4</sup> The shock distance in the model was derived to be  $z_{\text{sh}} = 5532 r_g$ , which corresponds to a linear scale of approximately  $\sim 0.5 \text{ mas}$  or less than  $0.1 \text{ pc}$ . The multi frequency radio maps from [Vermeulen](#)

<sup>3</sup>Rescaled to the distance adopted here.

<sup>4</sup>Lower limits, because the core is affected by free-free absorption, see [section 4.4](#).

TABLE 7.5: Luminosities NGC 1052

	$L_{R-UV}$ [erg s <sup>-1</sup> ] (1)	$L_{0.5-2 \text{ keV}}$ [erg s <sup>-1</sup> ] (2)	$L_{2-10 \text{ keV}}$ [erg s <sup>-1</sup> ] (3)	Ref. (4)
Observations	$6.98 \times 10^{42}$	$2 \times 10^{40}$	$2 \times 10^{41}$	a, b
Model	$3.97 \times 10^{42}$	$9.54 \times 10^{40}$	$2.97 \times 10^{41}$	a

**Notes.** (1) Integrated luminosity from radio to UV of the observational SED, and the model output spectrum; (2) Soft X-ray luminosity; (3) Hard X-ray luminosity; (4) References: (a) this work (b) [Hernández-García et al. \(2014\)](#).

[et al. \(2003\)](#) indicate (see [figure 4.5](#)), that the jet emission at 22 GHz originates mainly from linear distances of  $\sim 0.5$  pc away from the centre, and for lower frequencies even farther outward.<sup>5</sup> Therefore it can be assumed, that additional effects occur within a physical distance of  $\lesssim 0.5$  pc from the core, which cause the discrepancy between predicted and observed fluxes. Interestingly this approximately agrees with the geometrical estimations of a free-free absorbing torus ([Kameno et al. 2001](#)).

The occurring differences can be explained by various effects: The jet could be intrinsically more strongly aligned with respect to the line of sight, which, however, is rather unlikely due to kinematic and especially high frequency measurements (e.g. [Vermeulen et al. 2003](#); [Baczko et al. 2016](#)). A bending of the jet would lead to stronger boost factors outwards and naturally explain the progressively increasing asymmetries occurring towards lower frequencies, which was also previously suggested by [Kadler et al. \(2004b\)](#); [Dopita et al. \(2015\)](#). As found by [Kameno et al. \(2001\)](#), particle acceleration is necessary to maintain the strong synchrotron emission along the jet. There could occur an additional particle acceleration within the distance to the core of approximately  $\lesssim 0.5$  pc. Since the model dynamics do not include magnetic acceleration ([Markoff et al. 2008](#)), this effect could energise the particles and lead to higher radio fluxes. The time-scale of the simultaneous radio outbursts detected by [Heeschen and Puschell \(1983\)](#) times jet bulk velocity roughly coincide with dimensions of the plasma torus. A sudden acceleration in that region, probably by magnetic reconnection, naturally explains the non-detection at the lower frequency. Bending or acceleration could be confirmed or ruled out by extending the kinematic studies by longer monitoring ([Vermeulen et al. 2003](#)), at different frequencies, which would help to differentiate between ballistic trajectories or curvature/acceleration effects. Another possibility would be magnetic collimation of the jet, which is difficult to detect due to the presence of a free-free absorbing medium. Summing up all possible scenarios, the deviations between the model and observations occur in a distance which coincides with the size of the presumed free-free absorbing torus and are therefore could likely be connected to magnetic effects induced by the plasma torus.

Interestingly, the flux limits from core measurements agree with the model preshock component flux prediction. The freely expanding jet is capable of spectrally explaining the inner launching region of the jet. However, the parameters which characterise the base of the jet, specifically the geometry nozzle, are extreme: The nozzle radius  $r_0 = 68.4 r_g$  and the absolute nozzle height  $h_0 = h_{\text{rat}} r_0 = 43.8 r_g$  produce a larger nozzle than the previously reported parameters for the model of other LLAGNs (see [table 7.7](#)). These unusually large values are due to the unique shape of the SED (see [section 6.3](#)).

[Baczko et al. \(2016\)](#) imaged the nuclear region at a frequency of 86 GHz with the VLBI and derived from their resolution limits upper geometrical sizes for the unresolved bases

<sup>5</sup>The centre is assumed to be located in [figure 4.5](#) approximately in the middle of the fairly symmetric structure observed at higher frequencies.

TABLE 7.6: Model Energetics NGC 1052

$P_j$ [erg s <sup>-1</sup> ] (1)	$L_j$ [erg s <sup>-1</sup> ] (2)	$L_{\text{disc}}$ [erg s <sup>-1</sup> ] (3)	$L_{\text{RF}}$ [erg s <sup>-1</sup> ] (4)
$3.63 \times 10^{43}$	$5.13 \times 10^{42}$	$6.04 \times 10^{40}$	$(4.88 - 7.23) \times 10^{42}$

**Notes.** (1) Approximate model jet power requirement,  $10N_j$ ; (2) Model jet luminosity; (3) Accretion disc luminosity; (4) Rest frame energy range, constraint by limits of weakest and strongest beaming.

of the jet. The lowest resolution limit they state is  $8 \mu\text{as}$  along the jet, corresponding to a linear size in the plane of the sky of  $\sim 116 r_g$ . Therefore the model inferred size of the jet launching region ( $2 h_0 \sim 87 r_g$  plus black hole diameter) is smaller than the resolution limit of [Baczko et al. \(2016\)](#). However, this together indicates that the bases of the jet are located in the direct vicinity of the black hole.

### 7.3.3 Jet and Accretion Disc

A key result from modelling is the model integrated jet luminosity  $L_j \sim 5.13 \times 10^{42} \text{ erg s}^{-1}$ . NGC 1052 has a two-sided jet. The tightly constrained inclination and jet bulk velocity set theoretical limits on the strength of boosting, which we will use to derive the rest frame luminosity. The inclination of  $80^\circ$  assumed here results according to [Baczko et al. \(2016\)](#) in possible intrinsic jet bulk velocities of approximately  $\beta \sim (0.2 - 0.6)c$ . To obtain this result they used a jet spectral index of  $\alpha = -1$  at radio wavelengths, measured by ([Kadler et al. 2004b](#)). Interestingly, from the model power law index  $p = 3$  follows the same value, by the application of the classical relation [equation 2.4.4.2](#) to the optically thin synchrotron emission,  $\alpha = (p - 1)/2 = 1$ . We further assume a continuous jet,  $F_\nu \sim \delta^{2+\alpha} F'_{\nu'}$ , where the relativistic Doppler factor is  $\delta = 1/[\gamma(1 - \beta \cos \theta)]$  (see [A.2.4](#)). From these quantities we can derive the lower and the upper limit for the boosting factor:<sup>6</sup>

$$0.71 \lesssim b \lesssim 1.05 \quad (7.3.3.1)$$

The lower value is a strict limit, because for bulk velocities of smaller than  $\beta = 0.6$  the value moves monotonically towards unity. The upper limit must be considered more carefully: there exists a certain angle dependent velocity, where the boost factor becomes maximal. By varying the velocity stepwise that was found to appear for  $\beta \sim 0.17c$ . The boost factor is slightly higher than for  $\beta = 0.2$ , but lies within the rounding errors from above. These numbers set the maximum range of accessible boost factors, and in turn allow to enclose the jet rest frame luminosity in between

$$4.88 \times 10^{42} \text{ erg s}^{-1} \sim L_j/1.05 \lesssim L_{\text{RF}} \lesssim L_j/0.71 \sim 7.23 \times 10^{42} \text{ erg s}^{-1} \quad (7.3.3.2)$$

We produce the best-fit model for an inclination of  $\theta = 90^\circ$ , to estimate a complementary lower bound for the rest frame luminosity. The integrated jet luminosity is  $L_{90^\circ} \gtrsim 4.97 \times 10^{42} \text{ erg s}^{-1}$ . The minimum rest frame luminosity inferred from the maximum boost factor is slightly below  $L_{90^\circ}$  and therefore a strict lower limit to the rest frame luminosity.

An robust limit can be obtained for the accretion disc independently of the model. For an inner disc radius of  $r_{\text{in}} = 5 r_g$  followed a maximum temperature of  $T_{\text{in}} = 9000 \text{ K}$ , limited by the VIS-UV data. The disc luminosity results in  $L_{\text{disc}} = 6.04 \times 10^{40} \text{ erg s}^{-1}$ . If assuming the canonical efficiency  $\eta = 0.1$  for turning mass into radiation, the disc is fed

<sup>6</sup>At that inclination the threshold between effective boosting and de-boosting is a velocity of  $\beta \sim 0.33c$ .

by an accretion rate of  $\dot{M} = 1.06 \times 10^{-5} M_{\odot} \text{ yr}^{-1}$ . Assuming as before, that simply all the accreted matter is entirely converted into available energy, the maximum accretion power is  $L_{\text{disc}}/0.1 = 6.04 \times 10^{41} \text{ erg s}^{-1}$ . This power is enough to account for the kinetic jet power released into the environment of  $5 \times 10^{41} \text{ erg s}^{-1}$ , which was estimated by attributing the diffuse X-ray emission to jet driven shocks in the surrounding medium (Kadler et al. 2003). But, however, the maximum accretion power is a factor of 8 smaller than the minimum rest frame luminosity derived above  $L_{\text{RF}} \gtrsim 4.88 \times 10^{42} \text{ erg s}^{-1}$ . The maximum inferred accretion rate cannot provide the power to account for the minimum rest frame luminosity. It is even by a factor of  $\sim 60$  too small, to account for the approximate jet energy requirement.

### 7.3.4 Energetic Reasons for Truncation

Since a hypothetical standard accretion disc can not provide the necessary accretion rate to power the jet rest frame luminosity, another mechanism is required to explain that issue. Magnetohydrodynamic simulations of accreting BH show that for a high black hole spin the extraction of rotational energy can reach efficiencies of up to  $\eta \sim 200\%$  (Tchekhovskoy et al. 2011). However, their inferred maximum efficiencies are still too small to account for the here present lack of a factor 8.

At this place we want to apply the method developed in section 5.4. A truncated disc has a smaller efficiency in mass to light conversion (see subsection 5.4.2). It can provide more mass-inflow without contradicting the limits of the SED. The accretion disc spectrum is in this case not constrained by observations, but they impose limits: from mid-IR to the UV the spectrum can be well described by a power law  $F_{\nu} \propto \nu^{-\alpha}$  with  $\alpha \sim 2.7$  (Fernández-Ontiveros et al. 2012). Requiring the disc to account for the minimum rest frame luminosity, its accretion rate must be increased by at least a factor of 8. Under the maximum efficiency assumption (equation 5.4.2.8) we can rescale the disc via the application of the equations from subsection 5.4.3

$$\log r_{\text{in}} \propto \frac{3 + \alpha}{3\alpha + 1} \log \dot{M} \propto \frac{5.5}{9.1} \log \dot{M} \quad (7.3.4.1)$$

$$\log T_{\text{in}} \propto \frac{-2}{3\alpha + 1} \log \dot{M} \propto \frac{-2}{9.1} \log \dot{M} \quad (7.3.4.2)$$

This results in an inner truncation radius of  $r'_{\text{in}} \sim 18 r_g$ , inner edge temperature of  $T'_{\text{in}} \sim 5700 \text{ K}$  and a maximum efficiency of  $\eta' = 2.8\%$ . This rescaled disc would have an accretion rate of  $\dot{M}' = 8.5 \times 10^{-5} M_{\odot} \text{ yr}^{-1}$ . If we request the disc to provide the approximate total jet power requirement, i.e. scale it to 60 times the accretion rate, we would obtain a disc with an inner truncation radius of  $r^*_{\text{in}} \sim 59 r_g$ , inner edge temperature of  $T^*_{\text{in}} \sim 3700 \text{ K}$  and a maximum efficiency of  $\eta^* = 0.8\%$ . This rescaled disc would have an accretion rate of  $\dot{M}^* \sim 6.4 \times 10^{-4} M_{\odot} \text{ yr}^{-1}$ . If this accretion rate was entirely released in radiative energy ( $\eta = 1$ ), the resulting luminosity would be  $\sim 1.9 \times 10^{-3} L_{\text{edd}}$ , and is therefore still expected to fall into the low accretion regime where truncated discs are likely present.

These estimations assume the maximum efficiency of the primary typical accretion disc and of the rescaled disc, which depends only on the inner radius for infinite outer disc radius. For a finite outer radius the efficiency depends on both inner and outer radius and is smaller than the maximum efficiency. In order to make a conservative estimation, we assume that the outer disc radius varies together with the inner radius  $r_{\text{out}} = 4 r_{\text{in}}$ . This halves the maximum efficiency and therefore doubles the maximum accretion rate for the same observational constraints. In this conservative case the rescaled inner radii are lowered to  $r'_{\text{in}} \sim 12 r_g$  and  $r^*_{\text{in}} \sim 39 r_g$  to provide enough accretion power to account for the minimum rest frame luminosity and for the approximate total jet power requirement. These values are considered as lower limits: For the presumed black hole mass a thin

accretion disc of larger truncation radii can provide a higher mass inflow. At smaller radii it would be more efficient and its inner edge colder (data constraints) - consequently not providing enough accretion rate.

Summing that up, the problem of too less accretion rate can be solved by proposing the presence of a truncated accretion disc. To account for the minimum rest frame luminosity the conservatively truncated disc has a truncation radius of  $\gtrsim 12 r_g$ , and a conservative truncation radius of at least  $\gtrsim 39 r_g$  is necessary to account for the approximate total jet power requirement. Brenneman et al. (2009) investigate the accretion flow with *Suzaku*. On the one hand they detect relativistically broadened fluorescent Fe  $K\alpha$  line and constrain the inner truncation radius of the accretion disc to be  $< 45 r_g$ . On the other hand they find in the spectrum above 10 keV an unusually small continuum reflection from the disc, which casts doubt on the persistence of the disc into the innermost region. They suggest, that these might be indications of a transition from an optically thick disc to an optically thin ADAF. Interestingly, the energetic estimations carried here require truncation radii which agree with the findings of Brenneman et al. (2009).

### 7.3.5 Modelling the Spectrum II - Inflow or Outflow

In the present work NGC 1052's continuum spectrum is modelled by a compact jet.<sup>7</sup> As mentioned before in subsection 7.3.4, there are indications of an inefficiently radiating accretion flow inside of the truncated accretion disc. This subsection aims to compare an advection dominated accretion flow (ADAF) with the jet model adopted here. The model from Yu et al. (2011) contains both an ADAF and a jet. It is intended to reproduce the continuum emission from radio wavelengths to the X-rays.

In figure 7.2 both spectra are displayed. It shows X-ray, high, and low angular resolution data as in previous figures. The black line represents the total jet emission, i.e. the sum of preshock, postshock, and Compton component. The green line displays the ADAF+jet continuum emission. The ADAF needs an additional jet component, which introduce a new set of independent parameters. Both models qualitatively represent the radio to mid-IR and X-ray region similarly well. The ADAF overestimates largely the measured UV fluxes, as already pointed out by Yu et al. (2011). The jet model used in this work can explain the continuum emission of the entire sampled frequency range, in this case even

<sup>7</sup>For a description see section 3.1.

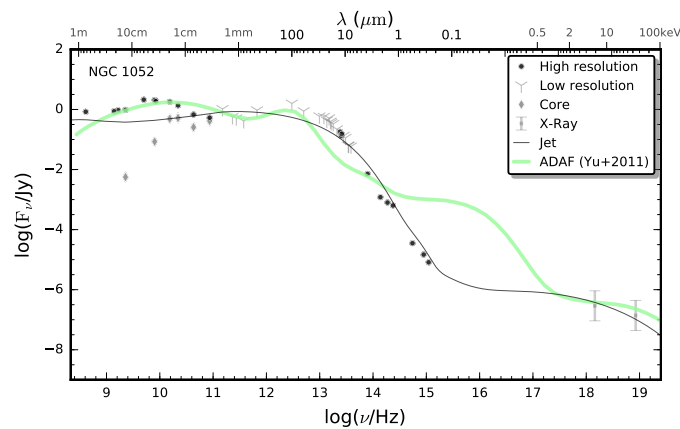


FIGURE 7.2: ADAF and jet model continuum emission for NGC 1052. The black line represents the total jet emission, i.e. the sum of preshock, postshock, and Compton component from the best-fit model. The green line displays the ADAF+jet model emission, intended to model the continuum (adopted from Yu et al. 2011).

without the accretion disc component. For possible explanations of the deviations in the radio frequencies see [subsection 7.3.2](#). The striking advantage of complex jet plus disc models as the one in this work is that it can capture most of the complexity shown by the SEDs of LLAGNs, without the need to incorporate additional components.

Here an important point shall be emphasised. The shown contradictions between the ADAF and the high angular resolution data, and the similar findings in [subsection 7.2.4](#) show, that the high angular resolution continuum shape of LLAGNs is different to the spectral expectations of inefficient accretion flows. This does not rule out the existence of those flows, but shows, that they do not dominate the continuum emission.

## 7.4 Synthesis

### 7.4.1 Comparing to the modelling of other LLAGNs - Breaking Degeneracies

The jet-disc model has also been applied to BHBs (e.g. [Markoff et al. 2005](#); and see others in [van Oers et al. 2017](#)), and to other LLAGNs, such as M87, M81, NGC4051, M94, and Sgr A\* (e.g. [Prieto et al. 2016](#); [Markoff et al. 2008](#); [van Oers et al. 2017](#); [Markoff et al. 2001](#)). The resulting parameters of this work are compared with those previous findings in detail with the compilation in [van Oers et al. \(2017\)](#). A collection of the parameters can be found in [table 7.7](#), focusing on the parameters of this work and previously modelled LLAGNs.

The range of black hole masses and the ranges of values for the energy normalisation are in the same range and fully comparable. NGC 4594 appears at the lower range of normalised accretion  $\sim 10^{-7}$ , while NGC 1052 shows a quite intermediate value, higher than the other LLAGNs but 2 orders below NGC 4051.

TABLE 7.7: Parameter Comparison

LLAGN	NGC 4594	NGC 1097	NGC 1052	Previous*
$m_{\text{bh}} [M_{\odot}]$	$1 \times 10^9$	$1.4 \times 10^8$	$1.54 \times 10^8$	$10^{6.2} - 10^{9.8}$
<b>Jet parameters</b>				
$N_j [L_{\text{edd}}]$	$6.98 \times 10^{-7}$	$2.53 \times 10^{-5}$	$1.87 \times 10^{-4}$	$10^{-6.5} - 10^{-1.7}$
$p$	2.8	2.3	3	2.4 – 3
$z_{\text{sh}} [r_g]$	277	112	5532	5 – 768
$r_0 [r_g]$	1.96	0.80	68.4	1 – 10
$h_{\text{rat}}$	13.2	3.01	0.64	0.7 – 15
$T_e [K]$	$3.57 \times 10^{11}$	$1.70 \times 10^{11}$	$7.62 \times 10^{11}$	$(0.4 - 4.5) \times 10^{11}$
$k$	5.53	53.3	0.9	0.03 – 2
<b>Luminosities</b>				
$l_j [L_{\text{edd}}]$	$1.18 \times 10^{-6}$	$3.92 \times 10^{-5}$	$2.65 \times 10^{-4}$	$2.1 \times 10^{-6} \dagger$
$l_{\text{disc}} [L_{\text{edd}}]$	$1.37 \times 10^{-7}$	$2.83 \times 10^{-6}$	$3.12 \times 10^{-6}$	$4.6 \times 10^{-7} \dagger$

**Notes.** *Upper part:* most important jet parameters: energy normalisation  $N_j$ , electron power law distribution index  $p$ , shock distance  $z_{\text{sh}}$ , nozzle radius  $r_0$ , relative nozzle height  $h_{\text{rat}}$ , electron temperature  $T_e$ , and equipartition  $k$ .

*Lower part:* comparison of model quantities. Model jet luminosity in Eddington fractions,  $l_j = L_j/L_{\text{edd}}$ . Luminosity of the accretion disc in Eddington fractions,  $l_{\text{disc}} = L_{\text{disc}}/L_{\text{edd}}$ . When observationally no thermal peak present, it represents the maximum luminosity in accordance with the data for an inner truncation radius  $r_{\text{in}} = 5r_g$ .

\*Values of LLAGNs from the compilation of [van Oers et al. \(2017\)](#) and references therein.

†Values from M87 ([Prieto et al. 2016](#)).

The power spectral indices are in agreement with the presumably somewhat steeper spectral indices found in LLAGNs,  $p \sim 3$ . Here at this point a basic difference regarding these values is stated: For all objects in this sample X-ray emission is purely SSC dominated. Therefore the spectral indices found can be interpreted as lower limits, especially in the case of NGC 1097 ( $p = 2.3$ ). It was investigated if appropriate fits can be achieved with synchrotron domination for the X-rays: For NGC 4594 (see [section 6.1](#)), the strong preshock seed radiation field directly causes a strong Compton component. The strong preshock component, however, is a result from modelling the well sampled SED in the IR. The same argumentation holds for NGC 1097, where this suppression would further increase the already very high equipartition values. Additionally, the relatively flat slope of the X-ray spectrum would require spectral indices of  $p \sim 2$  and shock distances of  $z_{\text{sh}} \sim 10^4$  to represent it with the postshock component. In the case of NGC 1052, the extremely flat X-ray spectrum together with the strong radio emission and the optical constraints prohibit to fit radio and X-rays simultaneously with the postshock component. Just fitting the X-rays is possible, but would require a very hard power law index below  $\sim 1.5$ , with which the rest of the spectrum could not be modelled at the same time. Regarding the previously modelled objects, e.g. for previously modelled M87, the SED shows a power law behaviour which does not require a strong preshock component. For some other objects the preshock component is only weakly constrained by high angular resolution data, not sufficient to constrain the dominant process (synchrotron or SSC) for the X-ray data (e.g. [van Oers et al. 2017](#)).

Summing that paragraph up: For NGC 1052 and NGC 1097, to represent X-rays with the postshock component the model must be forced to low spectral indices, which are below the previous values between 2.4 – 3. On the other hand, for NGC 4594 and NGC 1097 the Compton component must rather be suppressed (by higher equipartition) due to the strong preshock component necessary to represent the IR-UV data: For NGC 4594, and even more so for NGC 1097, the respective values are above equipartition. For the former the value is at the very high end range of previous values of LLAGNs. For the latter, the value is highly above equipartition. This is, again, mainly caused by the preshock component and in this specific case by the compact nozzle, which results in a high Compton component. In [figure 7.3](#) NGC 1097 is displayed for a configuration which shows appropriate fits for the radio, mm-wavelength, and X-ray region for equipartition  $k = 1.01$ . The IR-UV data are poorly represented by the model. For equipartition it is not possible to fit the IR-UV and X-ray measurements simultaneously with preshock and Compton component, respectively. Weakening SSC in order to allow synchrotron to fit the X-rays, a less compact nozzle would be required, further increasing the discrepancy to the IR-UV data.

For NGC 4594 and NGC 1097 the geometry of the base is small and compact. It has similar dimensions of previously modelled objects: Nozzle radius  $r_0$ , height  $h_{\text{rat}}$  and temperature  $T_e$  agree with previous parameter sets, just the nozzle radius of NGC 1097 is unusually small. The shock distance  $z_{\text{sh}}$  seems to be in tendency somewhat larger. This can be attributed to its freedom in the present iterations. Instead of fixing it it was iteratively determined which presumably, together with the rigid sampling, led to slightly higher values. However, the spectral impact of that parameter is small, making it highly variable in iterative determination. NGC 1052 shows a completely different picture: its nozzle radius is very large - one order of magnitude larger than for previous objects; the electron temperature and shock distance are also larger than all previous values. An extremely flat X-ray spectrum requires a very compact nozzle and/or a high electron temperature. The steep mid-IR to UV data limit the minimum nozzle radius which in turn is compensated with that high electron temperature. A large shock distance, together with a moderate power index, are necessary to avoid contradiction of the data. In total, the parameters of the objects investigated here seem to have a somewhat broader scatter, which is fully attributed

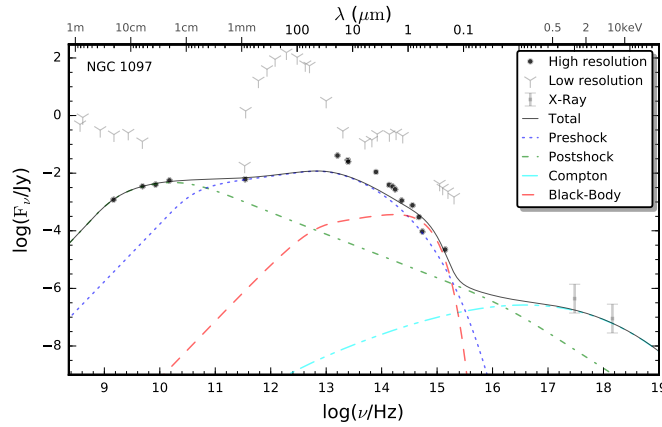


FIGURE 7.3: NGC 1097 for  $k = 1$ . A possible equipartition configuration which represents radio and X-ray data.

to the strong constraints imposed especially by the IR-UV data. Only for NGC 1052 there appear somewhat extreme parameters which previously have not been obtained in that form.

If in the IR-UV no data are accessible, or only upper limits (illustrated in figure 7.3) are accessible, there is a certain freedom of parameter-choice. The model can most probably be tuned to derive a fit in good agreement with the data, resulting in a representation which shows a low  $\chi^2$  value. However, the parameter freedom is likely to weaken the significance of the results. Well sampled SEDs, especially in the IR, are important to determine the shape of the preshock component and in turn impose stronger limits onto the parameters. It is interesting that the "active" requirement of the preshock component seems to break the model degeneracy between synchrotron emission or the SSC mechanism for the origin of the X-ray spectrum. Therefore, this highlights the importance of high angular resolution data across the spectrum. It is indispensable to obtain reliable results.

## 7.4.2 Elusive Accretion Discs - Truncated and Concealed

From high angular resolution observations another strong result can be inferred: UV continuum measurements show, that for the objects investigated here the signature of a standard accretion disc is weak or elusive. The main model component dominating the emission over the entire sampled spectral range is the jet. The missing -or weak in case for NGC 4594- blue bump confirms the general picture of LLAGNs. Any inefficient accretion flow seems to be no dominant component of the continuum emission.

From the observations robust limits for an standard accretion disc can be derived. As already found by Prieto et al. (2016) for M87, a standard<sup>8</sup> disc can just provide enough accretion power to explain the jet rest frame luminosity, but cannot provide enough power to feed the kinetic jet power. While these estimations could be attributed to previous phases of higher activity, things are different in the case of NGC 1052: Inclination and bulk velocities are strictly constrained by kinematic studies (e.g. Baczko et al. 2016; Vermeulen et al. 2003), which allow model independent energetic calculations. The result of these estimations (section 7.3) are, that the estimated minimum rest frame luminosity is less than the maximum typical accretion disc can provide. Even the extraction of rotational energy has a too low efficiency, according to recent magnetohydrodynamical simulations (e.g. Tchekhovskoy et al. 2011).

<sup>8</sup>Standard is used here in the sense, that the disc extends closely inwards to the black hole,  $r_{in} = 5r_g$ . These disc is presumed to have an efficiency of 10 per cent.

Within this work a possible solution for this problem is proposed: From the basic defining equation of the radiative energy release of the Shakura-Sunyaev thin accretion disc, we derive a scaling relation of the mass to light conversion efficiency in dependence of truncation radius (see [section 5.4](#)). A truncated disc of lower efficiency can provide a higher accretion mass-flow. This way, a higher accretion mass-flow can be established without contradicting the observational constraints. The method circumvents the above problem, and additionally allows to roughly estimate minimum truncation radius and maximum radiative efficiency for a disc of given accretion rate.

For the SEDs of LLAGNs which show no thermal signature, this scaling method can be applied and used to estimate minimum truncation radius, maximum temperature and maximum efficiency for the disc. This is done under the assumption, that the truncated disc must provide the mass-flow energy equivalent to account for the rest frame luminosity or the approximate energy requirement at the base of the jet. In the case of NGC 1052, where the largest discrepancy occurs, this method leads to truncation radii, which agree with measurements of [Brenneman et al. \(2009\)](#). For NGC 1097 the discrepancy is too small, but the problem of "missing accretion" can be solved by the application of the same technique. Similarly the missing accretion for M87 could be solved by appropriate rescaling of the disc. This technique is expected to hold only in the low accretion regime, where truncation occurs. In the case of NGC 1052 the most radical scaling provided a mass-flow of  $\dot{M} \sim 6.4 \times 10^{-4} M_{\odot} \text{ yr}^{-1}$  (see [section 7.3](#)). The luminosity equivalent of this mass flow is  $\sim 3.63 \times 10^{43} \text{ erg s}^{-1} \lesssim 2 \times 10^{-3} L_{\text{edd}}$ , and therefore likely in the regime where truncation is expected.



## Chapter 8

# Conclusion

LLAGNs are generally thought not to be just scaled-down versions of luminous AGNs, but stand out with fundamental differences. Observationally, the presence of jets and the spectrally missing "blue bump" of the standard thin accretion disc are tell-tale signs of their unique physics.

This thesis investigates a sample of three LLAGNs whose spectra include highest angular resolution measurements over nearly 10 orders of magnitude in frequency. Especially sub-arcsec resolution observations in the IR from VLT/NACO and from *HST* enable us to complement nuclear flux measurements in radio and the X-rays. The resulting well-sampled SEDs represent the innermost physical region. In this thesis these spectra are fitted with a semi-analytical model, consisting of a compact jet and a truncated accretion disc.

For all sources the continuum emission of a compact jet is the dominant component and gives an excellent representation of the observational SEDs over the entire spectrum. In the case of NGC 1052, the resulting requirements for the geometrical sizes of the base of the jet are in agreement with upper limits of observations. The well sampled SEDs enable us to break the model degeneracy between synchrotron emission and the SSC mechanism for the origin of the X-ray spectrum. This highlights the importance of high angular resolution measurements, especially in the IR. We find that all three sources are SSC dominated.

In NGC 4594's spectrum a thermal feature is modelled by the accretion disc component. For the other two sources no disc component is required to explain the continuum emission, but the measurements allow us to estimate model independent upper limits for the spectral contribution of the standard accretion disc. In the case of NGC 1097 the accretion power budget inferred from this disc component just accounts for the jet power requirement implied by the model within the model uncertainty and for the lower limit of the jet rest frame luminosity. In the case of NGC 1052 the maximum accretion power budgeted inferred from a standard accretion disc is below the jet power requirement within the model uncertainty and below the lower limit of the jet rest frame luminosity.

In the previous work of M87 the discrepancy between the inferred maximum accretion power budget and the much higher jet kinetic power could be explained by earlier periods of higher activity. For NGC 1052 this explanation does not hold: the standard accretion disc cannot provide enough accretion power to account for the jet emission. Alternative mechanisms such as the extraction of rotational energy of the central black hole could lower the discrepancy, but according to current magnetohydrodynamic simulations their predicted maximum efficiency of a few hundred per cent is still insufficient.

Within this work a possible solution for this problem is proposed: From the basic defining equation of the radiative energy release of the Shakura-Sunyaev thin accretion disc a scaling relation is derived, which relates the mass to light conversion efficiency to truncation radius. In detail, the upper limit of the efficiency scales inversely with truncation radius,  $\eta_{\max} \propto r_{\text{in}}^{-1}$ . The method circumvents the above problem, and additionally allows to estimate a minimum truncation radius and the maximum radiative efficiency for a disc

of given accretion rate. In the case of NGC 1052 the application of this method and the thereof estimated minimum truncation radius necessary to account for the jet emission is within the range of measurements of the Fe  $K\alpha$  line.

# Appendix A

## Appendix

### A.1 Eddington Limit

A central mass  $M$  attracts matter by gravity and repels it by radiation pressure at the same time. Under the idealised assumption of isotropy and interaction of light and electrons via the Thomson cross section, and neglecting interaction between light and protons, one can derive a limiting luminosity from the equilibrium of gravitational and radiative forces acting on ionised hydrogen gas (e.g. Rees 1984). An electron is receiving the power  $\sigma_T F$ , since  $F = L/4\pi r^2$  is the energy radiated per area and per time (see subsection 2.1.1), and  $\sigma_T$  is the Thomson cross section (see subsection 2.5.1), i.e. the effective area of the electron receiving radiation. Power divided by  $c$  is the photon momentum per time transferred to the electron,  $\sigma_T L/(4\pi r^2 c)$ . This is the radiation force acting onto an electron. Under the assumption of charge neutrality, i.e. no charge separation, electrons and protons are quasi-bound together. In a steady state the radiation force balances the gravitational force on the proton  $GMm_p/r^2$ , neglecting the much smaller mass of the electron, we obtain the Eddington limit

$$L_{\text{edd}} = \frac{4\pi c m_p G}{\sigma_T} M \quad (\text{A.1.0.1})$$

Under the assumptions from above, the luminosity of a given source is limited by  $L_{\text{edd}}$  since radiation pressure prevents matter from falling further in, intercepting the energy supply. This limit can be exceeded, when isotropy is violated, separation of charge becomes important, the assumption of interaction by the Thomson cross section is not valid, or, finally, no steady state is considered Peterson (1997). With an efficiency prescription of mass to light conversion one can relate mass accretion rate to Eddington luminosity.

### A.2 Special Relativity

#### A.2.1 Lorentz Transformations

Recapturing the angular dependency of emission from equation 2.3.2.3 the emission goes with  $\propto \sin^2 \theta$ . This only holds in the relativistic case for the electron's frame. The cone of emission is narrowed in comparison with the classical case, as relativistic aberration takes place. Therefore the Lorentz equations have to be used to recalculate the emission characteristic in the observer's frame.

Comparing lengths and time intervals in two distinct reference frames which are moving relatively to each other with a constant velocity  $\vec{v}$  is done classically by the Galilei transformations. If additionally requiring the velocity of light  $c$  to be constant and identical in both reference frames one yields the Lorentz transformations.

Without loss of generality  $K$  is the reference frame resting at origin and  $K'$  moving with  $v_x$

into  $x$ -direction. Then the Lorentz transformations are

$$x' = \gamma(x - v_x t) \quad (\text{A.2.1.1})$$

$$t' = \gamma\left(t - \frac{v_x x}{c^2}\right) \quad (\text{A.2.1.2})$$

where  $\gamma = 1/\sqrt{1 - (v_x/c)^2} = 1/\sqrt{1 - \beta^2} \geq 1$ . The coordinates perpendicular to the movement are not affected. A length  $l'$  in frame  $K'$  has a measured length in  $K$  of  $l = l'/\gamma$ . For an observer in  $K$  (at rest) objects are contracted along the axis of their movement relatively to the rest frame. The same holds for the time, a timer in  $K$  (at rest and origin) measures  $\tau = \tau'/\gamma$ , for a time interval  $\tau'$  in  $K'$ , thus a moving clock seems to lag.

The equations above transform in a way, that the observer at rest in  $K$  can measure his unprimed quantities to calculate the primed ones. Thus going from the observer rest frame into the moving particle frame. The inverse transformation take a similar form, just the primes are exchanged and the sign in front of the velocity is inverted. They are used when changing from the particle rest frame back to the observer frame. (REF)

Another important transformation is the change of mass, a result from the relativistic energy-momentum relation,

$$E^2 = (m_0 c^2)^2 + (pc)^2 \quad (\text{A.2.1.3})$$

A moving mass measured in  $K$  has a mass  $m = \gamma m_0$ , where  $m_0$  is the rest mass, i.e. the mass measured in  $K'$ . Quickly moving objects are heavier than their twins at rest. (REF)

## A.2.2 Relativistic Doppler Effect and Apparent Velocity

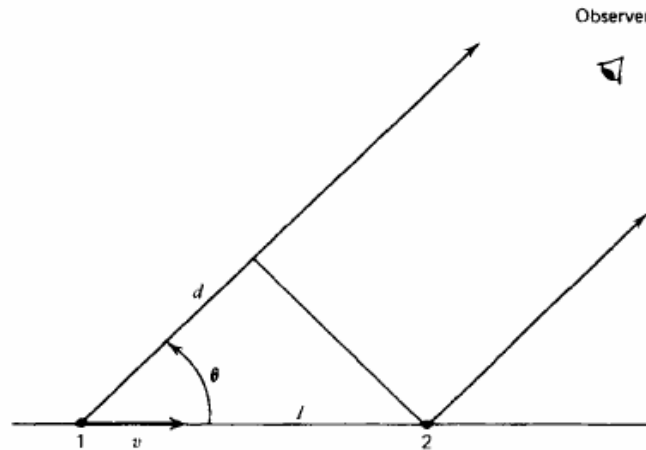


FIGURE A.1: Relativistic Doppler effect. From Rybicki and Lightman (1979).

One direct consequence is the relativistic Doppler effect, a joint effect of time dilation and classical Doppler effect. Consider a particle relativistically moving with velocity  $v$  w. r. t. an observer at rest. It radiates recurrently with time period  $\Delta t' = 1/\nu'$  (in its rest frame). According to time dilation (the lower case, going from particle to observer frame) in the observer frame the period is  $\Delta t = \gamma \Delta t'$ .

Assume the particle moves from 1 to 2 in figure A.1 in the time  $\Delta t$ . This covers the distance  $l = v \Delta t$ , corresponding to a geometrical lead  $d = v \Delta t \cos \theta$  for the radiation originating from point 1. The period the observer measures is  $\Delta t - d/c$ , corresponding to the frequency  $1/(\Delta t - d/c) = 1/[\Delta t(1 - \beta \cos \theta)]$ . Hence the frequency transformation from

observer to moving frame is

$$\nu' = 1/\Delta t' = \gamma/\Delta t = \gamma\nu(1 - \beta \cos \theta) = \frac{\nu}{\delta} \quad (\text{A.2.2.1})$$

where the relativistic Doppler factor is introduced,  $\delta = 1/[\gamma(1 - \beta \cos \theta)]$ . Analogously the inverse relation is  $\nu = \nu'\gamma(1 + \beta \cos \theta')$  (Rybicki and Lightman 1979).

As described above the time is  $\Delta t - d/c$ , which passes between the arrival of an emitted signal of an object from point 1 and point 2. The projection in the plane of the sky for the observer between point 1 and 2 is  $l \sin \theta$ . Hence the apparent velocity - the velocity an observer infers - is

$$\beta_{\text{app}} = \frac{l \sin \theta}{\Delta t - d/c} = \frac{\beta \sin \theta}{1 - \beta \cos \theta} \quad (\text{A.2.2.2})$$

The apparent velocity can exceed the the velocity of light, called superluminal motion. Tracing of bright emission plots of jets over time allows an estimation of the apparent speed.

### A.2.3 Aberration

Another effect of special relativity is the bending of angles when changing between reference systems, called aberration. From the basic transformation rules one can derive transformation of the velocities into arbitrary directions. Setting the velocity to  $c$  one yields the equations representing the aberration of light (Rybicki and Lightman 1979)

$$\cos \theta = \frac{\cos \theta' + \beta}{1 + \beta \cos \theta'} \quad (\text{A.2.3.1})$$

$$\sin \theta = \frac{\sin \theta'}{\gamma(1 + \beta \cos \theta')} \quad (\text{A.2.3.2})$$

$$\tan \theta = \frac{\sin \theta'}{\gamma(\cos \theta' + \beta)} \quad (\text{A.2.3.3})$$

where primed variables belong to  $K'$ . From these relations follows, that the coordinate axis perpendicular to the movement in  $K'$  is tilted into forward direction: for  $\theta' = 90^\circ$  follows  $\sin \theta = 1/\gamma$  and  $\cos \theta = \beta$ .

This has direct consequence for the emission pattern of a particle radiating via the Larmor formula (shown in figure 2.2). The nulls of the emission cones for relativistic movement are somewhat aligned with the direction of movement. For higher Lorentz factors this effect increases and for very high Lorentz factors the forward oriented emission is confined in a cone of total opening angle  $2\theta \approx 2/\gamma$ .

### A.2.4 Beaming

From phase space arguments one can show that the specific intensity transforms in such a way, that  $I_\nu/\nu^3$  is Lorentz invariant, the transformation of the specific intensity is  $I_\nu = \delta^3 I'_{\nu'}$  (e.g. Rybicki and Lightman 1979). In the case of a sphere, emitting isotropically in a power law distribution in the moving frame of the form  $F'_{\nu'} \propto \nu'^{-\alpha}$  it transforms as

$$F_\nu = \delta^{3+\alpha} F'_{\nu'} \quad (\text{A.2.4.1})$$

(e.g. Ghisellini 2013) where the additional factor " $\delta^\alpha$  is just the ratio of the intrinsic power-law fluxes at the observed and emitted frequencies" (Urry and Padovani 1995). The fluxes of a continuous jet transform as  $\delta^{2+\alpha}$  for the transformation of fluxes (e.g. Ghisellini 2013). These effects directly indicate, that for  $\delta > 1$  received emission of matter moving towards

us is boosted, and they must be considered to estimate the emission in the moving rest frame correctly.

Frequently an intrinsically symmetric continuous jet is assumed, then the jet-counterjet (approaching and receding jet) flux ratio can be used to constrain  $\beta \cos \theta$  by

$$\frac{F_{\text{app}}}{F_{\text{rec}}} = \left( \frac{1 + \beta \cos \theta}{1 - \beta \cos \theta} \right)^{2+\alpha} \quad (\text{A.2.4.2})$$

where  $\alpha$  is the measured spectral index (c. f. [Urry and Padovani 1995](#)). This equation, together with [equation A.2.2.2](#) constrain  $\beta$  and  $\theta$  to yield a approximate estimate for the orientation and bulk velocity of the jet.

The approaching jet flux is boosted and the receding jet flux is de-boosted. Smallest effective boosting, i.e. smallest observed fluxes from both, approaching and receding jet, is observed for an edge on geometry - the jets lie in the plane of the sky.

## A.3 Free-Free Emission

### A.3.1 Derivation with the Weak Encounter Concept

Free-free emission, also known as Bremsstrahlung, is radiation emitted by particles which undergo Coulomb interactions. We will follow the non-relativistic and classical (neglecting quantum mechanical effects) approach of [Jackson \(1975\)](#). The approximative results are transferable to those including quantum mechanics, with minor changes.

We consider an ionised hydrogen plasma, consisting out of protons and unbound electrons. Only the interaction between protons and electrons creates radiation, because scattering between particles with identical charge does not create radiation in dipole approximation. Accelerated electrons radiate according to the Larmor formula, [equation 2.3.2.4](#), protons are not considered, due to their smaller acceleration [subsection 2.3.2](#). Further is assumed, that the protons are at rest and regularly distributed within a volume.

The geometry of a single scattering within the weak encounter concept is shown in [figure A.2](#)). The electron passes by with impact parameter  $b$ . We assume first, a straight line for the trajectory of the electron - valid if the acceleration of the electron is small compared to its velocity, and second, that the attraction by the proton via the Lorentz force happens only normal to the direction of the movement. Then the accelerating Lorentz force of the proton  $F = q^2 / (4\pi\epsilon_0 r^2)$  accelerates the electron:

$$ma_{\perp} = \frac{q^2}{4\pi\epsilon_0 r^2} \cos \psi = \frac{q^2}{4\pi\epsilon_0 b^2} \cos^3 \psi \quad (\text{A.3.1.1})$$

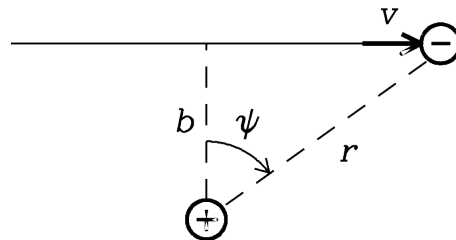


FIGURE A.2: Geometry scheme of the weak encounter principle. From <http://www.cv.nrao.edu/~sransom/web/Ch4.html>, accessed 2017-08-01.

Inserting this expression in the non-relativistic Larmor formula yields

$$P = \frac{q^6}{\underbrace{96\pi^3\epsilon_0^3 m^2 c^3}_{=C}} \frac{\cos^6 \psi}{b^4} \quad (\text{A.3.1.2})$$

for the emitted power in dependence of the electron position. To derive the total emitted energy  $W$ , we must integrate the expression above over time. From the derivative of  $\tan \psi = x/b$  we can express the time integration as  $dt = bd\psi/(v \cos^2 \psi)$ . This is used to carry out the integration:

$$W = \int_{-\infty}^{\infty} P dt = C \int_{-\infty}^{\infty} \frac{\cos^6 \psi}{b^4} dt = \frac{2C}{vb^3} \int_0^{\pi/2} \cos^4 \psi d\psi \quad (\text{A.3.1.3})$$

where the value of the latter integral is  $3\pi/16$ .  $W$  is the total radiated energy in the scattering process and depends only on velocity  $v$  and impact parameter  $b$ . Similar as for synchrotron emission we want to know the emission spectrum of the single scattering event (see section 2.4). To derive this one must Fourier transform the time dependent pulse  $P(t)$ . Similar as for synchrotron emission we can simplify this: In approximation the pulse is emitted in the characteristic collision time  $\tau = b/v$ . The power spectrum is then expected to peak at the frequency  $\nu = 1/(2\pi\tau) = v/(2\pi b)$  (Ghisellini 2013). The spectral power is then approximately

$$W_\nu \approx W/\nu = \frac{3\pi^2 C}{4} \frac{1}{b^2 v^2} \quad (\text{A.3.1.4})$$

Now this expression is used to derive the emissivity of an optically thin medium with equal electron and proton density  $n$ , where the protons are at rest and the electrons have all the same velocity  $v$ . The differential scattering rate, i.e. the number of electrons encountering one proton per unit time is the electron density times the crossed volume per unit time,  $dN/dt = ndV/dt = 2\pi n v b db$ . In the last step a cylindrical differential volume element is considered.

Since the velocity is fixed,  $W_\nu$  depends only on the impact parameter  $b$ . To yield the total emission of electrons scattered at a single proton one must integrate the convolution of differential scattering rate and  $W_\nu$  over  $b$ . Multiplying this result with the proton density and by assuming isotropy we get for the emissivity (equation 2.1.2.1):

$$j_\nu = \frac{1}{4\pi} n \int_{b_{\min}}^{b_{\max}} 2\pi W_\nu n_e v b db = \frac{3\pi^2 n^2 C}{8v} \ln \left( \frac{b_{\max}}{b_{\min}} \right) \quad (\text{A.3.1.5})$$

where the integration limits in the logarithm do not have a strong influence on the exact value. It turns out that quantum mechanical effects only modify the expression by a pre-factor Rybicki and Lightman (1979). These corrections are frequently collected in the so-called Gaunt factor  $g_{ff}$ . Considering a thermal distribution of electrons,

$$f(v) = 4\pi v^2 \left( \frac{m}{2\pi k_B T} \right)^{3/2} e^{-mv^2/2k_B T} \quad (\text{A.3.1.6})$$

we must add the distribution above and in addition integrate over the velocities to yield the full spectrum. The lower integration limit must have a minimum value, because otherwise the photon energy might exceed the particle's kinetic energy,  $1/2mv_{\min}^2 = h\nu$  which would violate the assumption of a free-free scattering process. The integral  $\int_{v_{\min}}^{\infty} dv j_\nu f(v)$

$\propto \int_{v_{min}}^{\infty} dv f(v)/v$  thus gives a non-vanishing contribution  $\sim \exp(-h\nu/k_B T)$  which suppresses the high frequency emission. Just considering the dependencies one gets

$$j_\nu \propto n^2 T^{-\frac{1}{2}} e^{-\frac{h\nu}{k_B T}} \quad (\text{A.3.1.7})$$

The emissivity of a medium with fixed density and a certain temperature has a high frequency cut off, whose onset is roughly at  $h\nu/k_B T \sim 1$ .

### A.3.2 Free-Free Absorption

For an optically thick medium we must consider absorption. In an optically thick medium with a thermal particle distribution we are in LTE and absorption is linked to the emissivity by  $\alpha_\nu = j_\nu/B_\nu$  (equation 2.1.2.3). In the Rayleigh-Jeans limit the absorption coefficient is:

$$\alpha_\nu \propto n^2 T^{-3/2} \nu^{-2} \quad (\text{A.3.2.1})$$

The absorption coefficient is strongly sensitive to the temperature and the frequency.

## A.4 Residual Plots

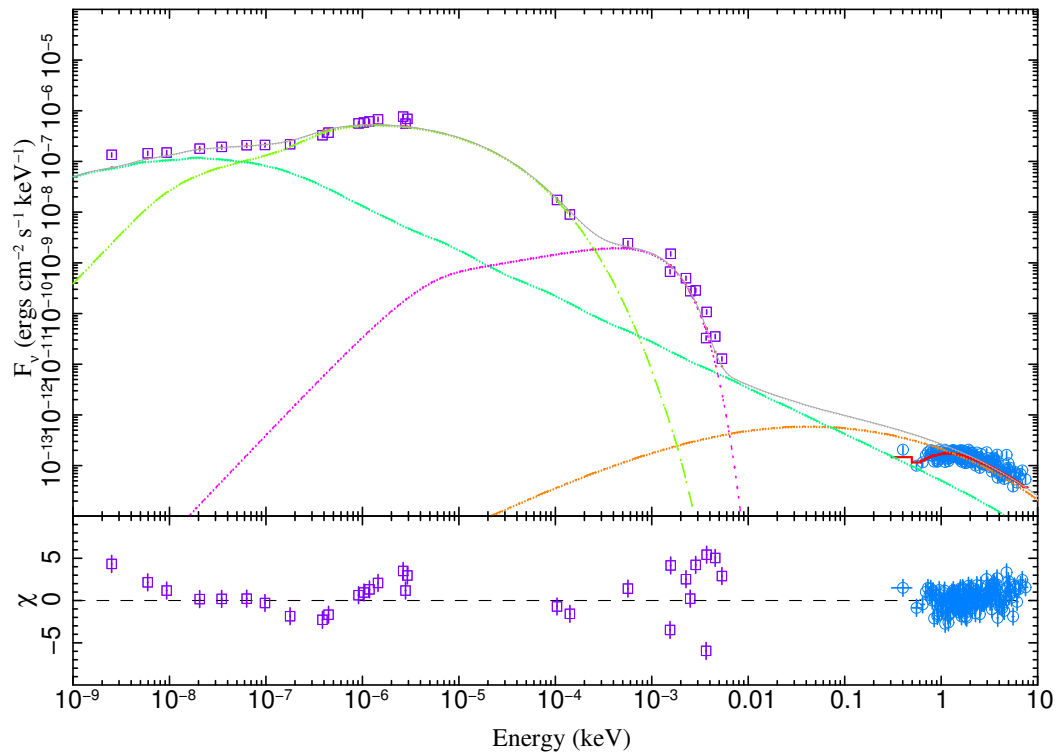


FIGURE A.3: Residual plot NGC 4594.

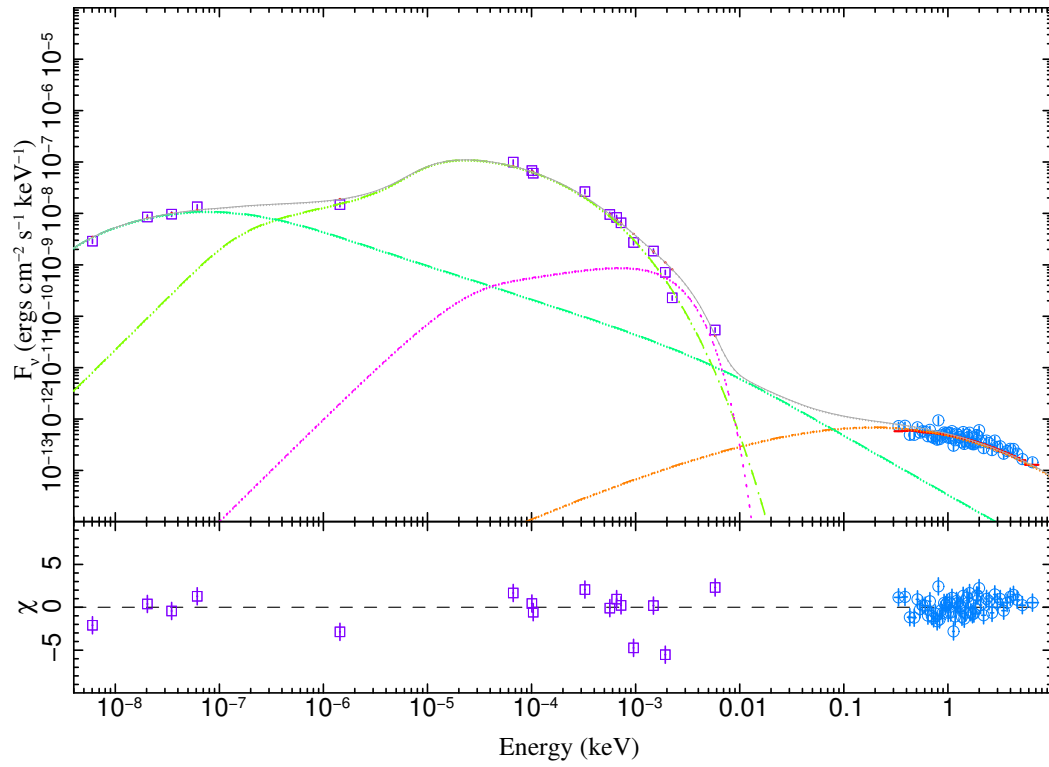


FIGURE A.4: Residual plot NGC 1097.

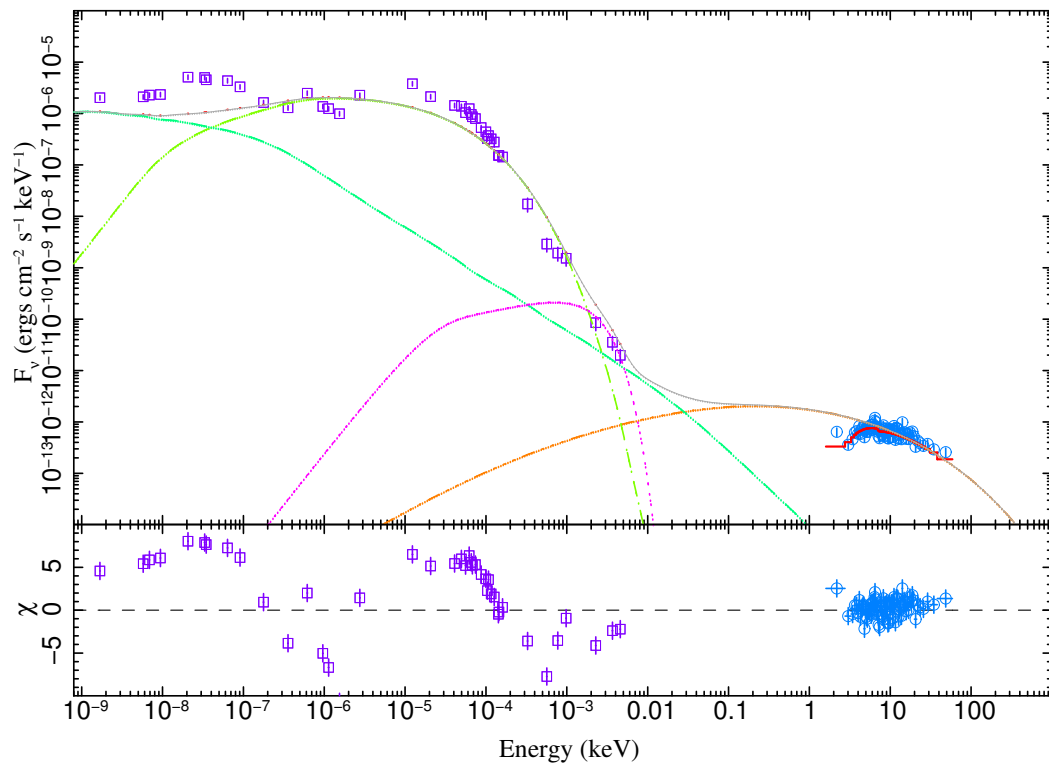


FIGURE A.5: Residual plot NGC 1052.



# Constants and Units

Speed of Light	$c = 2.997\,924\,58 \times 10^8 \text{ m s}^{-1}$
Vacuum Permittivity	$\epsilon_0 = 8.854\,187\,81 \times 10^{-12} \text{ F m}^{-1}$
Vacuum Permeability	$\mu_0 = 1.256\,637\,06 \times 10^{-6} \text{ V s A}^{-1} \text{ m}^{-1}$
Elementary Charge	$e = 1.602\,176\,62 \times 10^{-19} \text{ C}$
Electron Mass	$m_e = 9.109\,383\,56 \times 10^{-31} \text{ kg}$
Proton Mass	$m_p = 1.672\,621\,89 \times 10^{-27} \text{ kg}$
Gravitational Constant	$G = 6.674 \times 10^{-11} \text{ m}^3 \text{ kg}^{-1} \text{ s}^{-2}$
Planck Constant	$h = 6.626\,070\,04 \times 10^{-34} \text{ J s}$
Boltzmann Constant	$k_B = 1.380\,648\,5 \times 10^{-23} \text{ J K}$
Thomson Cross-Section	$\sigma_T = 6.652\,458\,56 \times 10^{-29} \text{ m}^2$
Stefan-Boltzmann Constant	$\sigma_B = 5.670\,37 \times 10^{-8} \text{ W m}^{-3} \text{ K}^{-1}$
Solar Mass	$M_\odot = 1.99 \times 10^{30} \text{ kg}$
Parsec	$1 \text{ pc} = 3.085\,677\,58 \times 10^{16} \text{ m}$
Pi	$\pi = 3.14159265$
Radian	$1 \text{ rad} = 180^\circ \pi^{-1}$
Electron Volt	$1 \text{ eV} = 1.602\,176\,62 \times 10^{-19} \text{ J}$
Erg	$1 \text{ erg} = 1 \times 10^{-7} \text{ J}$
Jansky	$1 \text{ Jy} = 1 \times 10^{-26} \text{ W Hz}^{-1} \text{ m}^{-2}$



# Bibliography

- B. P. Abbott, R. Abbott, T. D. Abbott, M. R. Abernathy, F. Acernese, K. Ackley, C. Adams, T. Adams, P. Addesso, R. X. Adhikari, and et al. Observation of Gravitational Waves from a Binary Black Hole Merger. *Physical Review Letters*, 116(6):061102, February 2016. doi:10.1103/PhysRevLett.116.061102.
- M. Ajello, L. Costamante, R. M. Sambruna, N. Gehrels, J. Chiang, A. Rau, A. Escala, J. Greiner, J. Tueller, J. V. Wall, and R. F. Mushotzky. The Evolution of Swift/BAT Blazars and the Origin of the MeV Background. *ApJ*, 699:603–625, July 2009. doi:10.1088/0004-637X/699/1/603.
- E. A. Ajhar, T. R. Lauer, J. L. Tonry, J. P. Blakeslee, A. Dressler, J. A. Holtzman, and M. Postman. Calibration of the Surface Brightness Fluctuation Method for use with the Hubble Space Telescope. *AJ*, 114:626–634, August 1997. doi:10.1086/118498.
- R. Antonucci. Unified models for active galactic nuclei and quasars. *ARA&A*, 31:473–521, 1993. doi:10.1146/annurev.aa.31.090193.002353.
- A.-K. Baczkó, R. Schulz, M. Kadler, E. Ros, M. Perucho, T. P. Krichbaum, M. Böck, M. Bremer, C. Grossberger, M. Lindqvist, A. P. Lobanov, K. Mannheim, I. Martí-Vidal, C. Müller, J. Wilms, and J. A. Zensus. A highly magnetized twin-jet base pinpoints a supermassive black hole. *A&A*, 593:A47, September 2016. doi:10.1051/0004-6361/201527951.
- E. Bajaja, G. van der Burg, S. M. Faber, J. S. Gallagher, G. R. Knapp, and W. W. Shane. The distribution of neutral hydrogen in the Sombrero galaxy, NGC 4594. *A&A*, 141:309–317, December 1984.
- A. J. Barth, A. V. Filippenko, and E. C. Moran. Polarized Broad H $\alpha$  Emission from the LINER Nucleus of NGC 1052. *ApJ*, 515:L61–L64, April 1999. doi:10.1086/311976.
- V. Beckmann, S. Soldi, C. Ricci, J. Alfonso-Garzón, T. J.-L. Courvoisier, A. Domingo, N. Gehrels, P. Lubiński, J. M. Mas-Hesse, and A. A. Zdziarski. The second INTEGRAL AGN catalogue. *A&A*, 505:417–439, October 2009. doi:10.1051/0004-6361/200912111.
- R. D. Blandford and A. Königl. Relativistic jets as compact radio sources. *ApJ*, 232:34–48, August 1979. doi:10.1086/157262.
- R. D. Blandford and D. G. Payne. Hydromagnetic flows from accretion discs and the production of radio jets. *MNRAS*, 199:883–903, June 1982. doi:10.1093/mnras/199.4.883.
- R. D. Blandford and R. L. Znajek. Electromagnetic extraction of energy from Kerr black holes. *MNRAS*, 179:433–456, May 1977. doi:10.1093/mnras/179.3.433.
- H. Bondi. On spherically symmetrical accretion. *MNRAS*, 112:195, 1952. doi:10.1093/mnras/112.2.195.

- L. W. Brenneman, K. A. Weaver, M. Kadler, J. Tueller, A. Marscher, E. Ros, A. Zensus, Y. Y. Kovalev, M. Aller, H. Aller, J. Irwin, J. Kerp, and S. Kaufmann. Spectral Analysis of the Accretion Flow in NGC 1052 with Suzaku. *ApJ*, 698:528–540, June 2009. doi:10.1088/0004-637X/698/1/528.
- W. Brinkmann, J. Siebert, and T. Boller. The X-ray AGN content of the Molonglo 408 MHz Survey: Bulk properties of previously optically identified sources. *A&A*, 281:355–374, January 1994.
- S. Campitiello, G. Ghisellini, T. Sbarrato, and G. Calderone. Radiatively efficient disks around Kerr black holes. *ArXiv e-prints*, January 2017.
- M. J. Claussen, P. J. Diamond, J. A. Braatz, A. S. Wilson, and C. Henkel. The Water Masers in the Elliptical Galaxy NGC 1052. *ApJ*, 500:L129–L132, June 1998. doi:10.1086/311405.
- S. D. Connolly, I. M. McHardy, C. J. Skipper, and D. Emmanoulopoulos. Long-term X-ray spectral variability in AGN from the Palomar sample observed by Swift. *MNRAS*, 459:3963–3985, July 2016. doi:10.1093/mnras/stw878.
- A. G. de Bruyn. Radio spectra of non-uniform synchrotron sources with internal absorption. *A&A*, 52:439–447, November 1976.
- A. G. de Bruyn, P. C. Crane, R. M. Price, and J. B. Carlson. The radio sources in the nuclei of NGC 3031 and NGC 4594. *A&A*, 46:243–251, January 1976.
- G. de Vaucouleurs, A. de Vaucouleurs, H. G. Corwin, Jr., R. J. Buta, G. Paturel, and P. Fouqué. *Third Reference Catalogue of Bright Galaxies. Volume I: Explanations and references. Volume II: Data for galaxies between 0<sup>h</sup> and 12<sup>h</sup>. Volume III: Data for galaxies between 12<sup>h</sup> and 24<sup>h</sup>*. 1991.
- M. A. Dopita, I.-T. Ho, L. L. Dressel, R. Sutherland, L. Kewley, R. Davies, E. Hampton, P. Shastri, P. Kharb, J. Jose, H. Bhatt, S. Ramya, J. Scharwächter, C. Jin, J. Banfield, I. Zaw, B. James, S. Juneau, and S. Srivastava. Probing the Physics of Narrow-line Regions in Active Galaxies. III. Accretion and Cocoon Shocks in the LINER NGC 1052. *ApJ*, 801:42, March 2015. doi:10.1088/0004-637X/801/1/42.
- A. Einstein. *Ueber einen die Erzeugung und Verwandlung des Lichtes betreffenden heuristischen Gesichtspunkt*. 1905. URL [http://echo.mpiwg-berlin.mpg.de/ECHODOCUVIEW?url=/permanent/einstein\\_exhibition/sources/HUN315QN/index.meta](http://echo.mpiwg-berlin.mpg.de/ECHODOCUVIEW?url=/permanent/einstein_exhibition/sources/HUN315QN/index.meta).
- A. Einstein. Näherungsweise Integration der Feldgleichungen der Gravitation. *Sitzungsberichte der Königlich Preussischen Akademie der Wissenschaften (Berlin)*, Seite 688-696., 1916.
- A. Einstein. Über Gravitationswellen. *Sitzungsberichte der Königlich Preussischen Akademie der Wissenschaften (Berlin)*, Seite 154-167., 1918.
- M. Elvis, B. J. Wilkes, J. C. McDowell, R. F. Green, J. Bechtold, S. P. Willner, M. S. Oey, E. Polowski, and R. Cutri. Atlas of quasar energy distributions. *ApJS*, 95:1–68, November 1994. doi:10.1086/192093.
- G. Fabbiano and J. Z. Juda. ROSAT Observations of the Sombrero Galaxy: Discovery of an X-Ray Active Nucleus. *ApJ*, 476:666–676, February 1997. doi:10.1086/303636.
- S. M. Faber, B. Balick, J. S. Gallagher, and G. R. Knapp. The neutral hydrogen content, stellar rotation curve, and mass-to-light ratio of NGC 4594, the “Sombrero” galaxy. *ApJ*, 214:383–389, June 1977. doi:10.1086/155260.

- H. Falcke. The Nuclear Jet in M81. *ApJ*, 464:L67, June 1996. doi:10.1086/310085.
- H. Falcke, M. A. Malkan, and P. L. Biermann. The jet-disk symbiosis. II. Interpreting the radio/UV correlations in quasars. *A&A*, 298:375, June 1995.
- B. L. Fanaroff and J. M. Riley. The morphology of extragalactic radio sources of high and low luminosity. *MNRAS*, 167:31P–36P, May 1974. doi:10.1093/mnras/167.1.31P.
- J. A. Fernández-Ontiveros, C. López-Sanjuan, M. Montes, M. A. Prieto, and J. A. Acosta-Pulido. The most recent burst of star formation in the massive elliptical galaxy NGC 1052. *MNRAS*, 411:L21–L25, February 2011. doi:10.1111/j.1745-3933.2010.00985.x.
- J. A. Fernández-Ontiveros, M. A. Prieto, J. A. Acosta-Pulido, and M. Montes. The SED of Low-Luminosity AGNs at high-spatial resolution. In *Journal of Physics Conference Series*, volume 372 of *Journal of Physics Conference Series*, page 012006, July 2012. doi:10.1088/1742-6596/372/1/012006.
- J. A. Fernández-Ontiveros, M. Almudena Prieto, J. A. Acosta-Pulido, S. Markoff, and O. González-Martín. The nature of the IR emission in LLAGN at parsec scales. Does the jet dominate at low-luminosities? In *European Physical Journal Web of Conferences*, volume 61 of *European Physical Journal Web of Conferences*, page 04005, December 2013. doi:10.1051/epjconf/20136104005.
- Y. Fukazawa, K. Hiragi, M. Mizuno, S. Nishino, K. Hayashi, T. Yamasaki, H. Shirai, H. Takahashi, and M. Ohno. Fe-K Line Probing of Material Around the Active Galactic Nucleus Central Engine with Suzaku. *ApJ*, 727:19, January 2011. doi:10.1088/0004-637X/727/1/19.
- G. Ghisellini, editor. *Radiative Processes in High Energy Astrophysics*, volume 873 of *Lecture Notes in Physics*, Berlin Springer Verlag, 2013. doi:10.1007/978-3-319-00612-3.
- O. González-Martín, J. Masegosa, I. Márquez, M. A. Guerrero, and D. Dultzin-Hacyan. X-ray nature of the LINER nuclear sources. *A&A*, 460:45–57, December 2006. doi:10.1051/0004-6361:20054756.
- J. E. Greene and L. C. Ho. The Mass Function of Active Black Holes in the Local Universe. *ApJ*, 667:131–148, September 2007. doi:10.1086/520497.
- D.J. Griffiths. *Introduction to Electrodynamics*. Prentice Hall, 1999. ISBN 9780138053260. URL <https://books.google.de/books?id=M8XvAAAAMAAJ>.
- M. Guainazzi and L. A. Antonelli. The flat X-ray spectrum of the LINER NGC 1052. *MNRAS*, 304:L15–L19, March 1999. doi:10.1046/j.1365-8711.1999.02470.x.
- K. Hada, A. Doi, H. Nagai, M. Inoue, M. Honma, M. Giroletti, and G. Giovannini. Evidence for a Nuclear Radio Jet and its Structure down to  $100$  Schwarzschild Radii in the Center of the Sombrero Galaxy (M 104, NGC 4594). *ApJ*, 779:6, December 2013. doi:10.1088/0004-637X/779/1/6.
- N. Häring and H.-W. Rix. On the Black Hole Mass-Bulge Mass Relation. *ApJ*, 604:L89–L92, April 2004. doi:10.1086/383567.
- T. M. Heckman. An optical and radio survey of the nuclei of bright galaxies - Activity in normal galactic nuclei. *A&A*, 87:152–164, July 1980.

- T. M. Heckman and P. N. Best. The Coevolution of Galaxies and Supermassive Black Holes: Insights from Surveys of the Contemporary Universe. *ARA&A*, 52:589–660, August 2014. doi:10.1146/annurev-astro-081913-035722.
- D. S. Heeschen. Optical Polarization in the Nuclei of Galaxies. *ApJ*, 179:L93, January 1973. doi:10.1086/181124.
- D. S. Heeschen and J. J. Puschell. Millimeter-wavelength outbursts in the elliptical galaxy NGC 1052. *ApJ*, 267:L11–L14, April 1983. doi:10.1086/183993.
- W. Heitler. *The Quantum Theory of Radiation*. Dover Books on Physics. Dover Publications, 1954. ISBN 9780486645582. URL <https://books.google.de/books?id=L7w7UpecbKYC>.
- L. Hernández-García, O. González-Martín, J. Masegosa, and I. Márquez. X-ray spectral variability of LINERs selected from the Palomar sample. *A&A*, 569:A26, September 2014. doi:10.1051/0004-6361/201424140.
- L. C. Ho. The Spectral Energy Distributions of Low-Luminosity Active Galactic Nuclei. *ApJ*, 516:672–682, May 1999. doi:10.1086/307137.
- L. C. Ho. Nuclear Activity in Nearby Galaxies. *ARA&A*, 46:475–539, September 2008. doi:10.1146/annurev.astro.45.051806.110546.
- L. C. Ho, A. V. Filippenko, and W. L. W. Sargent. A Search for “Dwarf” Seyfert Nuclei. III. Spectroscopic Parameters and Properties of the Host Galaxies. *ApJS*, 112:315–390, October 1997. doi:10.1086/313041.
- J. C. Houck and L. A. Denicola. ISIS: An Interactive Spectral Interpretation System for High Resolution X-Ray Spectroscopy. In N. Manset, C. Veillet, and D. Crabtree, editors, *Astronomical Data Analysis Software and Systems IX*, volume 216 of *Astronomical Society of the Pacific Conference Series*, page 591, 2000.
- E. Hummel, J. M. van der Hulst, and J. M. Dickey. Central radio sources in spiral galaxies: Starburst or accretion. *A&A*, 134:207–221, May 1984.
- V. Impellizzeri, A. L. Roy, and C. Henkel. The molecular torus in NGC 1052. In *The role of VLBI in the Golden Age for Radio Astronomy*, page 33, 2008.
- T. Izumi, K. Kohno, S. Martín, D. Espada, N. Harada, S. Matsushita, P.-Y. Hsieh, J. L. Turner, D. S. Meier, E. Schinnerer, M. Imanishi, Y. Tamura, M. T. Curran, A. Doi, K. Fathi, M. Krips, A. A. Lundgren, N. Nakai, T. Nakajima, M. W. Regan, K. Sheth, S. Takano, A. Taniguchi, Y. Terashima, T. Tosaki, and T. Wiklind. Submillimeter ALMA Observations of the Dense Gas in the Low-Luminosity Type-1 Active Nucleus of NGC 1097. *PASJ*, 65:100, October 2013. doi:10.1093/pasj/65.5.100.
- T. Izumi, K. Kohno, K. Fathi, E. Hatziminaoglou, R. I. Davies, S. Martín, S. Matsushita, E. Schinnerer, D. Espada, S. Aalto, K. Onishi, J. L. Turner, M. Imanishi, K. Nakanishi, D. S. Meier, K. Wada, N. Kawakatu, and T. Nakajima. On the disappearance of a cold molecular torus around the low-luminosity active galactic nucleus of NGC 1097. *ArXiv e-prints*, July 2017.
- J.D. Jackson. *Classical electrodynamics*. Wiley, 1975. ISBN 9780471431329. URL [https://books.google.de/books?id=\\_7rvAAAAMAAJ](https://books.google.de/books?id=_7rvAAAAMAAJ).

- J. B. Jensen, J. L. Tonry, B. J. Barris, R. I. Thompson, M. C. Liu, M. J. Rieke, E. A. Ajhar, and J. P. Blakeslee. Measuring Distances and Probing the Unresolved Stellar Populations of Galaxies Using Infrared Surface Brightness Fluctuations. *ApJ*, 583:712–726, February 2003. doi:10.1086/345430.
- S. Jester, H.-J. Röser, K. Meisenheimer, R. Perley, and R. Conway. HST optical spectral index map of the jet of 3C 273. *A&A*, 373:447–458, July 2001. doi:10.1051/0004-6361:20010593.
- J. R. Jokipii. Rate of energy gain and maximum energy in diffusive shock acceleration. *ApJ*, 313:842–846, February 1987. doi:10.1086/165022.
- F. C. Jones. Calculated Spectrum of Inverse-Compton-Scattered Photons. *Physical Review*, 167:1159–1169, March 1968. doi:10.1103/PhysRev.167.1159.
- M. Kadler, E. Ros, J. Kerp, H. Falcke, J. A. Zensus, R. W. Pogge, and G. V. Bicknell. The twin-jet of NGC 1052 at radio, optical, and X-ray frequencies. *New A Rev.*, 47:569–572, October 2003. doi:10.1016/S1387-6473(03)00095-2.
- M. Kadler, J. Kerp, E. Ros, H. Falcke, R. W. Pogge, and J. A. Zensus. Jet emission in <ASTROBJ>NGC 1052</ASTROBJ> at radio, optical, and X-ray frequencies. *A&A*, 420:467–474, June 2004a. doi:10.1051/0004-6361:20034126.
- M. Kadler, E. Ros, A. P. Lobanov, H. Falcke, and J. A. Zensus. The twin-jet system in NGC 1052: VLBI-scrutiny of the obscuring torus. *A&A*, 426:481–493, November 2004b. doi:10.1051/0004-6361:20041051.
- S. Kameno, S. Sawada-Satoh, M. Inoue, Z.-Q. Shen, and K. Wajima. The Dense Plasma Torus around the Nucleus of an Active Galaxy NGC1052. *PASJ*, 53:169–178, April 2001. doi:10.1093/pasj/53.2.169.
- K. I. Kellermann and I. I. K. Pauliny-Toth. The Spectra of Opaque Radio Sources. *ApJ*, 155:L71, February 1969. doi:10.1086/180305.
- K. I. Kellermann, R. Sramek, M. Schmidt, D. B. Shaffer, and R. Green. VLA observations of objects in the Palomar Bright Quasar Survey. *AJ*, 98:1195–1207, October 1989. doi:10.1086/115207.
- K. I. Kellermann, M. L. Lister, D. C. Homan, R. C. Vermeulen, M. H. Cohen, E. Ros, M. Kadler, J. A. Zensus, and Y. Y. Kovalev. Sub-Milliarcsecond Imaging of Quasars and Active Galactic Nuclei. III. Kinematics of Parsec-scale Radio Jets. *ApJ*, 609:539–563, July 2004. doi:10.1086/421289.
- J. Kormendy. The Stellar-Dynamical Search for Supermassive Black Holes in Galactic Nuclei. *Coevolution of Black Holes and Galaxies*, page 1, 2004.
- J. Kormendy, R. Bender, E. A. Ajhar, A. Dressler, S. M. Faber, K. Gebhardt, C. Grillmair, T. R. Lauer, D. Richstone, and S. Tremaine. Hubble Space Telescope Spectroscopic Evidence for a  $1 \times 10^9 M_{\text{sun}}$  Black Hole in NGC 4594. *ApJ*, 473:L91, December 1996. doi:10.1086/310399.
- D. Maitra, S. Markoff, C. Brocksopp, M. Noble, M. Nowak, and J. Wilms. Constraining jet/disc geometry and radiative processes in stellar black holes XTE J1118+480 and GX 339-4. *MNRAS*, 398:1638–1650, October 2009. doi:10.1111/j.1365-2966.2009.14896.x.
- K. Makishima, Y. Maejima, K. Mitsuda, H. V. Bradt, R. A. Remillard, I. R. Tuohy, R. Hoshi, and M. Nakagawa. Simultaneous X-ray and optical observations of GX 339-4 in an X-ray high state. *ApJ*, 308:635–643, September 1986. doi:10.1086/164534.

- S. Markoff. From Multiwavelength to Mass Scaling: Accretion and Ejection in Microquasars and AGN. In T. Belloni, editor, *Lecture Notes in Physics, Berlin Springer Verlag*, volume 794 of *Lecture Notes in Physics, Berlin Springer Verlag*, page 143, March 2010. doi:10.1007/978-3-540-76937-8\_6.
- S. Markoff, H. Falcke, F. Yuan, and P. L. Biermann. The Nature of the 10 kilosecond X-ray flare in Sgr A\*. *A&A*, 379:L13–L16, November 2001. doi:10.1051/0004-6361:20011346.
- S. Markoff, M. A. Nowak, and J. Wilms. Going with the Flow: Can the Base of Jets Subsume the Role of Compact Accretion Disk Coronae? *ApJ*, 635:1203–1216, December 2005. doi:10.1086/497628.
- S. Markoff, M. Nowak, A. Young, H. L. Marshall, C. R. Canizares, A. Peck, M. Krips, G. Petitpas, R. Schödel, G. C. Bower, P. Chandra, A. Ray, M. Munro, S. Gallagher, S. Hornstein, and C. C. Cheung. Results from an Extensive Simultaneous Broadband Campaign on the Underluminous Active Nucleus M81\*: Further Evidence for Mass-scaling Accretion in Black Holes. *ApJ*, 681:905–924, July 2008. doi:10.1086/588718.
- A. Merloni, S. Heinz, and T. di Matteo. A Fundamental Plane of black hole activity. *MNRAS*, 345:1057–1076, November 2003. doi:10.1046/j.1365-2966.2003.07017.x.
- M. Mezcuca and M. A. Prieto. Evidence of Parsec-scale Jets in Low-luminosity Active Galactic Nuclei. *ApJ*, 787:62, May 2014. doi:10.1088/0004-637X/787/1/62.
- D. Mihalas. *Stellar Atmospheres*. Astronomy and Astrophysics Series. W. H. Freeman, 1978. ISBN 9780716703594. URL <https://books.google.de/books?id=P197QgAACAAJ>.
- J. A. Miller and R. Ramaty. Ion and relativistic electron acceleration by Alfvén and whistler turbulence in solar flares. *Sol. Phys.*, 113:195–200, 1987. doi:10.1007/BF00147698.
- K. Mitsuda, H. Inoue, K. Koyama, K. Makishima, M. Matsuoka, Y. Ogawara, K. Suzuki, Y. Tanaka, N. Shibasaki, and T. Hirano. Energy spectra of low-mass binary X-ray sources observed from TENMA. *PASJ*, 36:741–759, 1984.
- I. N. Bronstein and K. A. Semendjajew. *Taschenbuch der Mathematik*. BSB B. G. Teubner Verlagsgesellschaft, Nauka-Verlag, Leipzig, Moskau, 19 edition, 1979. ISBN 3871444928.
- N. M. Nagar, H. Falcke, and A. S. Wilson. Radio sources in low-luminosity active galactic nuclei. IV. Radio luminosity function, importance of jet power, and radio properties of the complete Palomar sample. *A&A*, 435:521–543, May 2005. doi:10.1051/0004-6361:20042277.
- R. Narayan and I. Yi. Advection-dominated Accretion: Underfed Black Holes and Neutron Stars. *ApJ*, 452:710, October 1995. doi:10.1086/176343.
- R. S. Nemmen, T. Storchi-Bergmann, F. Yuan, M. Eracleous, Y. Terashima, and A. S. Wilson. Radiatively Inefficient Accretion Flow in the Nucleus of NGC 1097. *ApJ*, 643:652–659, June 2006. doi:10.1086/500571.
- K. L. Nicholson, G. A. Reichert, K. O. Mason, E. M. Puchnarewicz, L. C. Ho, J. C. Shields, and A. V. Filippenko. Evidence for low-level AGN activity in the nucleus of the LINER galaxy NGC4594. *MNRAS*, 300:893–906, November 1998. doi:10.1046/j.1365-8711.1998.01944.x.

- J. B. Oke. Absolute Energy Distribution in the Optical Spectrum of 3C 273. *Nature*, 197: 1040–1041, March 1963. doi:10.1038/1971040b0.
- K. Onishi, S. Iguchi, K. Sheth, and K. Kohno. A Measurement of the Black Hole Mass in NGC 1097 Using ALMA. *ApJ*, 806:39, June 2015. doi:10.1088/0004-637X/806/1/39.
- A. G. Pacholczyk. *Radio astrophysics. Nonthermal processes in galactic and extragalactic sources*. 1970.
- B. Paczyński and P. J. Wiita. Thick accretion disks and supercritical luminosities. *A&A*, 88: 23–31, August 1980.
- S. Pellegrini, A. Baldi, G. Fabbiano, and D.-W. Kim. An XMM-Newton and Chandra Investigation of the Nuclear Accretion in the Sombrero Galaxy (NGC 4594). *ApJ*, 597:175–185, November 2003. doi:10.1086/378235.
- D. E. Perez-Olea and L. Colina. X-Ray Emission of Active Galactic Nuclei with Circumnuclear Star-forming Rings: NGC 1097 and NGC 7469. *ApJ*, 468:191, September 1996. doi:10.1086/177681.
- B.M. Peterson. *An Introduction to Active Galactic Nuclei*. Cambridge University Press, 1997. ISBN 9780521479110. URL <https://books.google.de/books?id=ok4EF1PMStwC>.
- M. A. Prieto, J. Reunanen, K. R. W. Tristram, N. Neumayer, J. A. Fernandez-Ontiveros, M. Orienti, and K. Meisenheimer. The spectral energy distribution of the central parsecs of the nearest AGN. *MNRAS*, 402:724–744, February 2010. doi:10.1111/j.1365-2966.2009.15897.x.
- M. A. Prieto, J. A. Fernández-Ontiveros, S. Markoff, D. Espada, and O. González-Martín. The central parsecs of M87: jet emission and an elusive accretion disc. *MNRAS*, 457: 3801–3816, April 2016. doi:10.1093/mnras/stw166.
- M. J. Rees. Black Hole Models for Active Galactic Nuclei. *ARA&A*, 22:471–506, 1984. doi:10.1146/annurev.aa.22.090184.002351.
- M. J. Rees, M. C. Begelman, R. D. Blandford, and E. S. Phinney. Ion-supported tori and the origin of radio jets. *Nature*, 295:17–21, January 1982. doi:10.1038/295017a0.
- J. Reunanen, M. A. Prieto, and R. Siebenmorgen. VLT diffraction-limited imaging at 11 and 18  $\mu\text{m}$  of the nearest active galactic nuclei. *MNRAS*, 402:879–894, February 2010. doi:10.1111/j.1365-2966.2009.15997.x.
- G. H. Rieke, M. J. Lebofsky, and J. C. Kemp. Nonthermal optical-infrared emission from NGC 1052. *ApJ*, 252:L53–L56, January 1982. doi:10.1086/183718.
- F. Rohrlich. *Classical Charged Particles*. World Scientific, 1964. ISBN 9789812700049. URL <https://books.google.de/books?id=lJrPrP6L6tQC>.
- G.B. Rybicki and A.P. Lightman. *Radiative Processes in Astrophysics*. A Wiley-Interscience publication. Wiley, 1979. ISBN 9780471827597. URL <https://books.google.de/books?id=LtdEjNABM1sC>.
- S. Sawada-Satoh, S. Kameno, K. Nakamura, D. Namikawa, K. M. Shibata, and M. Inoue. Positional Coincidence of H<sub>2</sub>O Maser and a Plasma-Obscuring Torus in Radio Galaxy NGC 1052. *ApJ*, 680:191–199, June 2008. doi:10.1086/587886.

- M. Schmidt. 3C 273 : A Star-Like Object with Large Red-Shift. *Nature*, 197:1040, March 1963. doi:10.1038/1971040a0.
- C. K. Seyfert. No. 671. Nuclear emission in spiral nebulae. *Contributions from the Mount Wilson Observatory / Carnegie Institution of Washington*, 671:1–13, 1943.
- N. I. Shakura and R. A. Sunyaev. Black holes in binary systems. Observational appearance. *A&A*, 24:337–355, 1973.
- F. Shankar, P. Salucci, G. L. Granato, G. De Zotti, and L. Danese. Supermassive black hole demography: the match between the local and accreted mass functions. *MNRAS*, 354: 1020–1030, November 2004. doi:10.1111/j.1365-2966.2004.08261.x.
- M. Sikora, Ł. Stawarz, and J.-P. Lasota. Radio Loudness of Active Galactic Nuclei: Observational Facts and Theoretical Implications. *ApJ*, 658:815–828, April 2007. doi:10.1086/511972.
- A. K. Singal. Radiation reaction and pitch-angle changes for a charge undergoing synchrotron losses. *MNRAS*, 458:2303–2306, May 2016. doi:10.1093/mnras/stw349.
- L. K. Steinborn, K. Dolag, M. Hirschmann, M. A. Prieto, and R.-S. Remus. A refined sub-grid model for black hole accretion and AGN feedback in large cosmological simulations. *MNRAS*, 448:1504–1525, April 2015. doi:10.1093/mnras/stv072.
- T. Storchi-Bergmann, J. A. Baldwin, and A. S. Wilson. Double-peaked broad line emission from the LINER nucleus of NGC 1097. *ApJ*, 410:L11–L14, June 1993. doi:10.1086/186867.
- T. Storchi-Bergmann, R. Nemmen da Silva, M. Eracleous, J. P. Halpern, A. S. Wilson, A. V. Filippenko, M. T. Ruiz, R. C. Smith, and N. M. Nagar. Evolution of the Nuclear Accretion Disk Emission in NGC 1097: Getting Closer to the Black Hole. *ApJ*, 598:956–968, December 2003. doi:10.1086/378938.
- A. Tchekhovskoy, R. Narayan, and J. C. McKinney. Efficient generation of jets from magnetically arrested accretion on a rapidly spinning black hole. *MNRAS*, 418:L79–L83, November 2011. doi:10.1111/j.1745-3933.2011.01147.x.
- R. B. Tully. *Nearby galaxies catalog*. 1988.
- Y. Ueda, Y. Ishisaki, T. Takahashi, K. Makishima, and T. Ohashi. The ASCA Medium Sensitivity Survey (the GIS Catalog Project): Source Catalog. *ApJS*, 133:1–52, March 2001. doi:10.1086/319189.
- C. M. Urry and P. Padovani. Unified Schemes for Radio-Loud Active Galactic Nuclei. *PASP*, 107:803, September 1995. doi:10.1086/133630.
- C. J. van Houten. Surface photometry of extragalactic nebulae (Errata: 17 310). *Bull. Astron. Inst. Netherlands*, 16:1, November 1961.
- P. van Oers, S. Markoff, P. Uttley, I. McHardy, T. van der Laan, J. Donovan Meyer, and R. Connors. A jet-dominated model for a broad-band spectral energy distribution of the nearby low-luminosity active galactic nucleus in M94. *MNRAS*, 468:435–450, June 2017. doi:10.1093/mnras/stx514.
- S. Veilleux and D. E. Osterbrock. Spectral classification of emission-line galaxies. *ApJS*, 63: 295–310, February 1987. doi:10.1086/191166.

- R. C. Vermeulen, E. Ros, K. I. Kellermann, M. H. Cohen, J. A. Zensus, and H. J. van Langevelde. The shroud around the twin radio jets in NGC 1052. *A&A*, 401:113–127, April 2003. doi:10.1051/0004-6361:20021752.
- J.-H. Woo and C. M. Urry. The Independence of Active Galactic Nucleus Black Hole Mass and Radio Loudness. *ApJ*, 581:L5–L7, December 2002. doi:10.1086/345944.
- Z. Yu, F. Yuan, and L. C. Ho. On the Origin of Ultraviolet Emission and the Accretion Model of Low-luminosity Active Galactic Nuclei. *ApJ*, 726:87, January 2011. doi:10.1088/0004-637X/726/2/87.
- F. Yuan and R. Narayan. Hot Accretion Flows Around Black Holes. *ARA&A*, 52:529–588, August 2014. doi:10.1146/annurev-astro-082812-141003.



# Erklärung

Hiermit erkläre ich, Lennart REB, die vorliegende Arbeit, "*Modelling the Spectral Energy Distribution of Low Luminosity Active Galactic Nuclei*", selbständig verfasst zu haben und keine anderen als die in der Arbeit angegebenen Quellen und Hilfsmittel benutzt zu haben.

München, den 1. August 2017

Unterschrift:

---